VERTICALLY ORDERED NANOSTRUCTURES FOR ENERGY HARVESTING AND STORAGE

by

Umang Vijay Desai

B.S. in Chemical Engineering

Institute of Chemical Technology (formerly UDCT), 2008

Submitted to the Graduate Faculty of

Swanson School of Engineering in partial fulfillment

of the requirements for the degree of

Doctor of Philosophy

University of Pittsburgh

2013

UNIVERSITY OF PITTSBURGH

SWANSON SCHOOL OF ENGINEERING

This dissertation was presented

by

Umang Vijay Desai

It was defended on

July 11, 2013

and approved by

Prashant Kumta, PhD, Professor, Department of Chemical and Petroleum Engineering

Götz Veser, PhD, Professor, Department of Chemical and Petroleum Engineering

Jung-Kun Lee, PhD, Associate Professor, Department of Mechanical Engineering and Materials Science

Dissertation Director: Di Gao, PhD, Associate Professor, Department of Chemical and Petroleum Engineering

VERTICALLY ORDERED NANOSTRUCTURES FOR ENERGY HARVESTING AND STORAGE

Umang Vijay Desai, PhD

University of Pittsburgh, 2013

Vertically ordered (1-D) nanostructures provide a promising alternative to conventional nanoparticle films used as electrode materials for energy conversion and storage devices. These 1-D nanostructures, in forms of nanowires or nanotubes, promote mass transfer and accessibility of the electrodes while providing a direct conduction path for electrons. Our work has been focused on synthesis and application of novel 1-D nanostructures for dye-sensitized solar cells (DSCs) and lithium-ion batteries (LIBs).

The vertically aligned 1-D nanostructures are employed in DSCs to overcome the limitation of nanoparticle-based DSCs. Much longer electron life time has been observed in DSCs based on 1-D nanostructures compared to the nanoparticle-based ones, which allows us to use thicker sensitized film to improve the efficiency. We have developed a facile low-temperature hydrothermal method to synthesize vertically aligned ZnO nanowire arrays directly on transparent conductive oxide, and to use the ZnO nanowire arrays as a template to synthesize SnO_2 nanotube arrays. In addition, we have developed a convenient approach that involves alternate cycles of nanowire growth and self-assembled monolayer coating processes for synthesizing multilayer assemblies of 1-D nanostructures with ultrahigh internal surface areas.

The vertically aligned nanostructure also enables us to fabricate high-efficiency solid-state DSCs by replacing the liquid electrolyte with a solid hole transporting material. The vertically aligned nanostructures provide straight channels for filling the solid electrolyte,

enabling the use of thicker photoanodes for solid-state DSCs. Significantly, by using vertically aligned multilayer arrays of TiO_2-coated ZnO nanowires, liquid-electrolyte DSCs with power conversion efficiency up to 7.0% and solid-state DSCs with efficiency up to 5.65% have been obtained.

Vertically ordered 1-D nanostructures also offer remarkable advantages for rechargeable LIBs including fast electron transport/collection and ion diffusion, enhanced electrode-electrolyte contact area, and facile accommodation of strains caused during the charge and discharge cycles. We have developed a method to fabricate SnO_2 nanotube arrays and hybrid Sn-based nanotube arrays directly on current collecting substrate (Ti) and have evaluated their performance as anodes in rechargeable LIBs. The hybrid Sn-based nanotube arrays synthesized by us delivered a capacity of 710 mAh/g after 80 cycles with a low capacity fade.

TABLE OF CONTENTS

LIST OF TABLES

LIST OF FIGURES

ACKNOWLEDGEMENTS

First and foremost, I would like to thank my research advisor, Dr. Di Gao, for his invaluable support and guidance during my five years in his research group. His spirited thinking and ability to come up with new ideas have always impressed me and I will treasure the experience of working with him. I would like to thank my lab mates Jiamin Wu and Liang-Liang Cao for helping me during my PhD, especially during the first few years in the lab. I am particularly grateful to Dr. Chengkun Xu for his tremendous help and support with my work on dye-sensitized solar cells.

I would like to especially thank all my family and friends with whom I have spent all the wonderful moments with during the five years of my PhD. Spending time with them has made my journey through graduate school a memorable and an enjoyable one. Finally, I would like to thank my parents for their unconditional love and support. I am glad I was able to repay their patience and sacrifice by successfully completing my PhD.

1.0 INTRODUCTION

The tremendous challenges that face us to meet our future energy needs are now widely recognized. The annual world energy consumption is currently estimated to be 4.1×10^{13} joules, or 13 trillion watts.[1, 2] A major portion of these energy needs are currently met from fossil fuels. Between 2004 and 2030 the annual global consumption of energy is estimated to further rise by more than 50%.[3] As per the current policies, most of this increase in energy is expected to come from fossil fuels, resulting in almost a commensurate increase in CO_2 emissions. A major portion of the energy currently produced in the US is from coal which is a major contributor to the CO_2 emissions. The impact of these CO_2 emissions is a matter of great concern. In the last 200 years, CO_2 level in the atmosphere has increased from 280 ppm to 380 ppm. Industrial activities, mainly power generation from coal, have also increased the total mercury flux from 1600 tons/year in the pre-industrial era to 5000 tons/year, of which 3000 tons is deposited on land and 2000 tons is deposited in the marine.[4] Despite these grave consequences, and the projected increase in gas and oil prices, less than 10% of the global energy production in 2030 is expected to come from renewable energy sources. There is no single solution to the challenges we face concerning meeting our energy needs without causing further environmental harm. The best approach would be to utilize various alternative technologies in tandem to reduce the overall dependence on fossil fuels.

Almost all alternative energy technologies, be it for conversion or storage, are limited by either the availability or the properties of current material. Photovoltaic devices are limited by the poor charge-carrier mobilities and narrow absorption spectra in current materials limiting the light harvesting and energy conversion efficiencies. Storage devices such as lithium-ion batteries and supercapacitors are limited by insufficient energy or power densities and efficiencies owing largely to the poor charge and mass transport properties. The high manufacturing costs and poor availability of the best performing materials have further limited the widespread use of these devices. Fundamental advances in synthesis, processing and control of material structure and properties could lead to significantly more efficient energy conversion and storage technologies. Of great interests are nanotechnology and nanostructure materials, which are expected to have a great impact on the potential widespread use of these technologies. Recently, ordered nanomaterials and device designs based on these nanomaterials have demonstrated very promising results for energy conversion and storage.[1, 5, 6] Though the unique advantages of these ordered nanostructures vary from device to device, the fundamental advantage of fast electron and charge transport is the chief driving force for keen interest in these materials.

Our work has focused on synthesizing vertically ordered, 1-D nanostructures and examining their performance for energy generation and storage devices. More specifically, we have synthesized and evaluated the performance of these ordered nanostructures for dye-sensitized solar cells (DSCs), a promising low-cost, third generation photovoltaic, and lithium-ion batteries. To start of, we have spoken briefly about the potential of the photovoltaic market and the role DSCs could play in the future.

Background on Photovoltaic Market

Now, more than ever before, energy is what makes our world continuously work. World energy consumption is *ca.*4.7 x 10^{20} J (450 quadrillion BTU) and is expected to grow about 2% every year for next 25 years.[7] The current earth's resources upon which the energy needs are dependent are finite and there is a pressing need of making a suitable transition to renewable fuels. Among all the renewable energy technologies, photovoltaic technology utilizing solar energy is the most promising one. The supply of energy from the sun to the earth is gigantic, i.e., 3 x 10^{24} J/year or about 10^4 times what mankind consumes currently. In other words, covering only 0.1% of the earth's surface with solar cells with an efficiency of 10% would suffice to satisfy our current needs.[8]

The photovoltaic market has had outstanding yearly growth, 33% growth per year since 1997, and it is expected to grow by 25 to 30% per year in the next decades. While traditional energy sources become more expensive, PV will be much more competitive due to technology improvements and economies of scale.[9] Currently, mono and polycrystalline silicon have dominated the photovoltaic market. Even though silicon is far from and ideal material for photovoltaic conversion, the major reason for crystalline silicon market dominance is that manufacturers have been supplied with rejected materials from the semi-conductor industry. There have been various materials and technologies which have been studied to replace silicon solar cells with the aim of reducing the costs and improving the devices efficiencies. **Table 1** shows the record efficiencies for the various types of photovoltaic cells as reported in the literature.[10] Amongst these various types of photovoltaic cells listed, dye sensitized solar cells and organic solar cells can be classified as the third generation of photovoltaics. By this

classification we imply that they are currently in the research stage. Even at this early stage in their development cycle, DSCs have already attracted considerable interest for use as building integrated photovoltaics (BIPV) for supplementary electricity generation. In the next section, we have given a brief explanation of the working principles and the unique advantages of DSCs and our motivation to work in this field.

Table 1. Confirmed terrestrial cell and submodule efficiencies measured under the global AM 1.5 spectrum (1000 W/m^2) at 25°C

Classification	Efficiency (%)	Description
Silicon		
• Si (crystalline)	25.0 ± 0.5	UNSW PERL
• Si (multicrystalline)	20.4 ± 0.5	FhG-ISE
• Si (amorphous)	10.1 ± 0.3	Oerlikon Solar Lab, Neuchatel
• Si (nanocrystalline)	10.1 ± 0.2	Kaneka
III-V Cells		
• GaAs (thin film)	28.8 ± 0.9	Alta Devices
• GaAs (multicrystalline)	18.4 ± 0.5	RTI, Ge substrate
• InP (crystalline)	22.1 ± 0.7	Spire, epitaxial
Thin Film Chalcogenide		
• CIGS (cell)	19.6 ± 0.6	NREL, on glass
• CIGS (submodule)	17.4 ± 0.5	Solibro, 4 serial cells
• CdTe (cell)	18.3 ± 0.5	GE Global Research
Photochemical		
• Dye-sensitized (cell)	11.9 ± 0.4	Sharp
• Dye-sensitized (module)	9.9 ± 0.4	Sony, 8 parallel cells
Organic		
• Organic thin film (cell)	10.7 ± 0.3	Mitsubishi Chemicals
• Organic (submodule)	6.8 ± 0.2	Toshiba (15 series cells)

1.1 DYE-SENSITIZED SOLAR CELLS

Dye-sensitized solar cells (DSCs) are a very promising alternative to traditional photovoltaics for low cost energy production. The main difference between DSCs and conventional solar cells is that in DSCs the functional element, which is responsible for absorption of light (dye), is separated from the charge carrier transport media. This is contrary to conventional solar cells where a semiconductor assumes both functions. This separation of functions leads to lower purity demands on the raw materials side and makes it possible for DSCs to use low- to medium-purity materials which can be synthesized through low-cost processes. In essence, DSC can be looked as an analogous concept to photosynthesis where a dye is used to absorb the light from the sun.

DSCs main advantages can be summarized as follows[7]:

- Good performance under standard reporting conditions;
- Stable performance at nonstandard conditions of temperature, irradiation and solar incidence angle;
- Low cost
- Available environmental-friendly raw materials
- Semi-transparency and multi-color range possibilities

1.1.1 Working Principle of Dye-Sensitized Solar cells (DSCs)

A schematic representation of the operating principles of a conventional DSC is given by **Figure 1**. At the heart of the system is a nanoparticle semiconductor oxide film. The material of choice has been TiO_2 although other wide band-gap semiconductor materials have also been

studied. Attached to the nanoparticle film is a monolayer of the charge transfer dye. This dye is responsible for the absorption of photons from the incoming light. The nanoparticle film, with a dye attached to it, is placed in contact with a redox electrolyte or an organic hole conductor. The electrolyte of choice till date has been a redox system containing and iodide/triodide couple in an organic solvent. Photoexcitation of the dye results in the injection of an electron into the conduction band of the semiconductor oxide. The original state of the dye is subsequently restored by electron donation from the electrolyte. The regeneration of the dye by the electrolyte intercepts the recapture of the conduction band electron by the oxidized dye. The redox couple is regenerated, in turn, by the reduction of triiodide at the counter electrode, with the circuit being completed via electron migration through the external load. Overall, the device generates electric power from light without any permanent chemical transformation. The voltage generated under illumination corresponds to the difference between the Fermi level of the electron in the semiconductor oxide and the redox potential of the electrolyte.

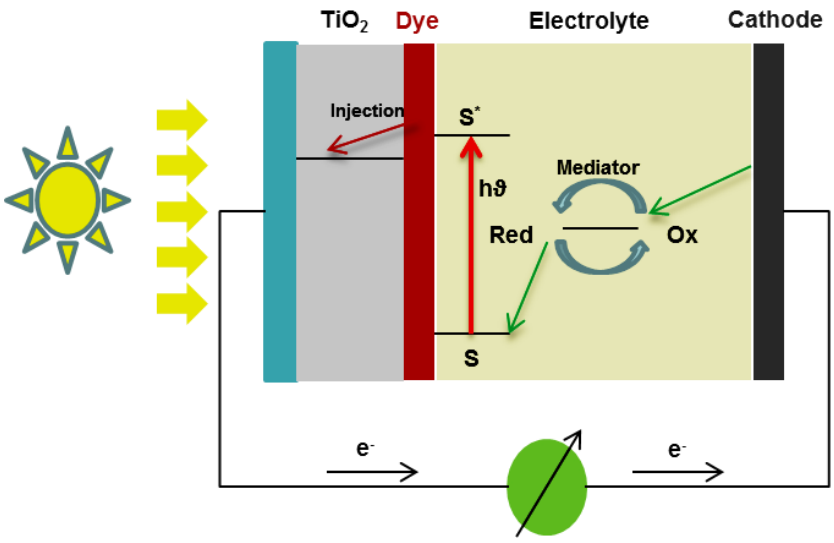

Figure 1. Principle of operation of a traditional dye-sensitized solar cell

The article published in 1991 by Gratzel and co-workers[11] originated the interest in DSCs that still seems to be increasing each year. A conversion efficiency of 7.1% was reported at that time and evolution has continued progressively since then, with efficiency of 12.3% reported recently.[12] Much of the research has been centered on[13]:

(a) improving the spectral absorbance of the dye,

(b) improving the electron transport in the cell by using a wide band-gap semiconductor of suitable morphology,

(c) improving the stability of the cell by replacing the liquid electrolyte with solid hole-transport materials (HTMs).

The best photovoltaic performance both in terms of conversion yield and long-term stability has so far been achieved using dyes with polypyridyl complexes of ruthenium. The ruthenium complex $(Bu_4N)_2[Ru(4,4'\text{-}(COOH)\text{-}2,2,\text{-}bipyridene)_2(NCS)_2]$, known as N719 dye has become the paradigm of sensitizer for DSCs. N719 is the most commonly reported dye in published literature and hence, to evaluate our DSCs, we have used N719 dye for most of our work presented in this report. We have focused our work on improving the electron transport in DSC by replacing the nanoparticle film with vertically ordered nanostructures of metal oxides. We will discuss the advantages of vertically ordered structures over nanoparticle films for DSCs in the next section.

1.1.2 Vertically Ordered Nanostructures for DSCs

DSC anodes are typically constructed of nanoparticle films several micrometers thick. These films are typically composed of TiO_2 nanoparticles to achieve high surface area supports

for the dye monolayer. The films must be thick to maximize the path length of incident light and hence the absorption by the dye. However, inefficient electron transport in the nanoparticle film results in low electron diffusion constants and recombination losses, preventing the usage of thicker photoanodes.

Remarkably, the charge collection efficiency of these nanoparticle films is high due to the slow kinetics of the back reaction of injected electrons with the electrolyte. The electron diffusion lengths in these devices are accordingly long, up to several tens of micrometers. However, current research efforts on DSC improvements focus on the development of new dyes and electrolytes, thus changing the kinetics of the forward and reverse redox reactions. In these and other cases where surface recombination becomes significant, the low electron diffusion coefficients become significantly more detrimental to device performance. The slow percolation of electrons through a random polycrystalline nanoparticle network is the major factor limiting further improvement in the photocurrent efficiencies achievable using nanocrystalline DSCs. **Table 2** lists the various efforts made in improving DSCs and how the use of nanoparticle film has proved to be a limitation in these efforts.

Table 2. Limitations of nanoparticle based DSCs

Approach for Improving DSCs	**Main Purpose**	**Limitation of the NP-based anodes**
Use solid electrolyte / ionic liquid	Overcome packaging problems	Ineffective filtration & short electron diffusion length
Increase thickness of sensitized film	Improve light harvesting efficiency (LHE) in the red and near-infrared region	Short electron diffusion length
Sensitizing with quantum dots	Improve light harvesting efficiency (LHE) in the red and near-infrared region	Ineffective filtration
Use alternative redox couple	Remove Pt, increase Voc and therefore overall efficiency	Short electron lifetime

Vertically ordered nanostructures, in the form of nanowires, nanotubes or nanorods, are a very promising solution to overcome these limitations. **Figure 2** shows a schematic of the DSC architecture with vertically ordered structures. These vertically aligned nanostructures behave like nanoparticles assembled into columns resulting in significantly fewer grain boundaries. The vertically ordered structures thus provide straight conduction channels, a form of highway for the electrons. As a result, the electron mobility in these vertically aligned structures is larger than that in the nanoparticle films due to their directional and uninterrupted conduction channel, as opposed to the tortuous percolation network and grain boundaries of the nanoparticle films. This directed transport is expected to increase the electron diffusion constant, thus improving the efficiency of charge collection and enabling the production of optically thick cells which absorb

more incident light. Inorganic vertically ordered structures of wide-band gap semiconductors thus represent an ideal charge transport medium for nanostructured DSCs and represent a promising alternative to nanoparticle films.

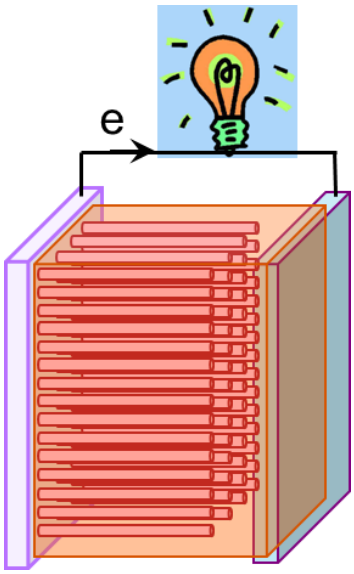

Figure 2. Ideal DSC architecture with vertically ordered nanostructure

We have investigated the performance of various such vertically oriented nanostructures which have been discussed in some detail in this report. In Chapter **3.0** we discuss the synthesis and performance of ordered SnO_2 nanotube arrays in DSCs. In Chapter **4.0** we have demonstrated synthesis of high surface area multilayer ZnO nanowire arrays and showed their remarkable performance in DSCs.

1.1.3 Vertically Ordered Nanostructures for Solid-State DSCs

Another area of research that has attracted considerable interest is the replacement of the volatile liquid electrolyte in DSCs. Although reported DSCs that yield the highest efficiencies are based on liquid electrolytes,[13-15] the main problem is that the use of liquid electrolyte

limits device stability. Improper sealing of the cell can lead to evaporative loss of the electrolyte and permeation of water and oxygen molecules which may react with the liquid electrolyte. This leads to deterioration of device performance. Manufacturing of multi-cell modules using liquid electrolytes is also difficult as the cells have to be connected electrically yet separated chemically. Many attempts have been made to overcome these limitations by replacing the liquid electrolyte with a solid or a quasi-solid hole-transport material (HTM).[13]

To date, the power conversion efficiency of most solid-state DSCs has been far below the efficiency of their counterparts based on liquid electrolytes.[13, 15] This is likely because of two factors that have been identified by researchers. First, the anode of most current DSCs uses a porous film of sintered nanoparticles, and effective filling of HTM into this porous film has been challenging, putting a limitation on the thickness of the nanoparticle film that could be used for a solid-state DSC. Secondly, the electron–hole recombination rate in a solid-state DSC has been observed to be much faster than in the corresponding liquid electrolyte DSC[16]; this also puts a limit on the thickness of the nanoparticle films, whose charge extraction relies on trap-limited diffusion for electron transport. As a result of these two factors, the optimum thickness of the sensitized film for solid-state DSCs has been found to be around 2 μm,[17-20] which is significantly thinner than the film thickness typically used for liquid electrolyte DSCs. The limitation on the thickness of the sensitized film leads to insufficient dye loading and thus low light harvesting efficiency. Anodes based on vertically ordered nanostructures could help overcome these limitations for solid-state DSCs. The vertically ordered nanostructures greatly facilitate filling of the sensitized films with solid-state HTM. They also provide a direct conduction path for electrons to travel between the dyes and the conducting substrate and thus significantly improve the electron-transport properties of the anodes. Therefore, compared to

those based on sintered nanoparticles, much thicker anodes based on vertically aligned nanostructures may be used in solid-state DSCs, and higher efficiencies may be obtained. We have evaluated the performance of vertically oriented nanostructures, in the form of aligned ZnO nanowires in Chapter **5.0** of this report. The promising results observed using these nanowire arrays encouraged us to explore the use of our multilayer assembly of nanowires for solid-state DSCs and we have discussed the results we obtained in Chapter **6.0** of this report.

1.2 LITHIUM-ION BATTERIES

Lithium-ion batteries (LIBs) have been widely recognized as an important energy storage device for portable electronics as well as electric vehicles.[21, 22] The main motivation behind using batteries based on Li metal ion is the fact that Li is the most electropositive as well as the lightest metal, thus facilitating the design of systems with high energy densities. In the subsequent sections, we briefly discuss the working of LIBs and possible advantages which vertically ordered nanostructures may have for application in LIBs.

1.2.1 Working Principle of Lithium-Ion Batteries

The three main components of a lithium-ion battery are the anode, cathode and a separator between them to prevent short-circuit. The cell is filled with an electrolyte to facilitate easy transfer of Li ions between the electrodes. **Figure 3** shows the schematic representation of a typical Li-ion cell. During charge, Li is removed from the cathode, transferred through the separator and inserted into the anode. The reverse movement of ions occurs during discharge i.e.

Li is extracted from the anode and collected at the cathode. The cell voltage is defined by the difference in the voltage of the cathode and the anode. The amount of Li that is stored in each of these electrode materials determines the capacity of the cell. The amount of electrical energy delivered by the battery per mass or volume depends on both the cells voltage and the capacity, which are dependent on those three functional components. The three main means to increase the energy deliverable by the battery are:

- Increase the voltage of the cathode
- Decrease the voltage of the anode
- Increase the capacity of the materials used as electrodes

In our work, we have synthesized of hybrid Sn-based nanotube arrays as a possible high capacity anode material for LIBs. The potential advantages of such vertically ordered nanostructures for LIBs are explained in the next section.

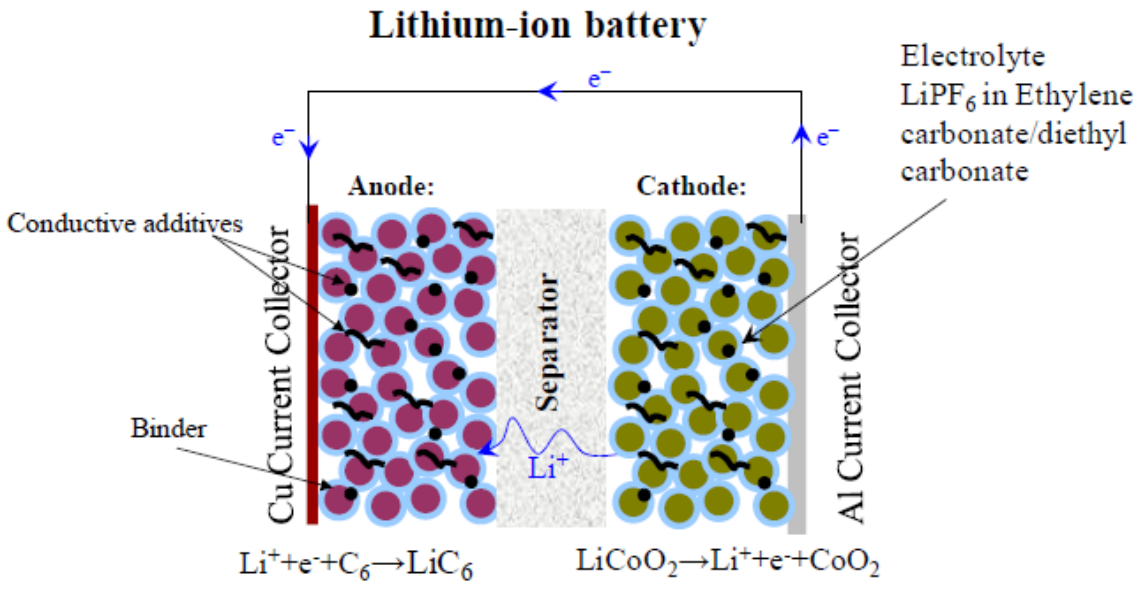

Figure 3. Schematic of a typical Li-ion cell

1.2.2 Vertically Ordered Nanostructures for Lithium-Ion Batteries

So far, much effort has been devoted to replacing the commercially available graphite anode materials in LIBs with alternate materials which offer higher lithium storage capacity.[5, 23-28] In recent years, various metals and metal oxides have been investigated as potential anode materials in lithium-ion batteries. Among the various such materials systems, both tin (Sn)[29-32] and tin oxide (SnO_2)[33-35] have received considerable research interest because of their high theoretical capacities (993 mAh/g and 782 mAh/g, respectively, based on the stoichiometry of 4.4 Li ions intercalating with each Sn atom) and low discharge potentials.[36]

A critical issue which has hampered the commercial use of these Sn-based anodes is the severe capacity fading observed during the intercalation and de-intercalation of Li ions. The main reason for this is the large volume change (>250%) brought about by the lithium insertion/ extraction process.[37, 38] These large volume changes lead to pulverization of the active materials and disconnection of the electrical contact with the current collector, which ultimately causes irreversible capacity fade.

One promising way to overcome the capacity loss due to pulverization is to use nanostructured electrode materials which can better withstand the strains produced by the large volume changes. 1-D nanostructures in the form of nanowires or nanotubes offer a promising alternative to overcome this problem. Recently, ordered nanostructures grown directly on conducting substrates have been reported to give significantly improved performance.[34, 39-41] The main advantage of growing the nanostructures directly on the current collector is improved electrical contact. They also offer efficient pathway for electron transport, facilitate strain relaxation as well as offer improved electrolyte contact. Another major advantage is the ability to use the active material directly as the anode material without the addition of binders or other

conducting additives. The ability to use the active material without any additives should enable increased material loading resulting in higher capacity LIBs.[42-44] In the light of all these potential advantages, we have tested our SnO_2 nanotube arrays directly on Ti substrate and evaluated their performance as anode material for LIBs. The details of this part of our work are discussed later in Chapter **7.0** In the next chapter, we have described the method used by us to grow ZnO nanowire arrays, which forms the backbone of all the materials synthesized by us and described in the subsequent chapters.

2.0 SYNTHESIS OF ZINC OXIDE NANOWIRE ARRAYS

Before we get started with the main body of our work, I would like to briefly go over the method we used for synthesizing ZnO nanowires. Growing ZnO nanowires is a preliminary step and an integral part of all the work carried out and documented by us in this report. In order to avoid repetition, we thought it would be best to discuss this at the beginning.

We have used a liquid-phase chemical process for growing arrays of ultralong ZnO nanowire arrays on seeded substrates. The substrate used for DSCs is a conducting glass substrate, Indium-doped Tin Oxide (ITO). The substrate used for work on LIBs is titanium foil. In the liquid-phase deposition (LPD) process, used by us to grow ZnO nanowires, the synthesis can be described by the following reaction:

$$Zn^{2+} + 2OH^{-} \rightarrow Zn(OH)_2 \rightarrow ZnO + H_2O$$

where hexamethylenetetramine (HMTA), NaOH, or NH_4OH may be used as the hydroxide source. LPD approaches have the advantages of low growth temperature, low cost and ease in scale-up. A major drawback of the liquid phase approaches, however, is that ZnO forms both on the seeded substrates and in the bulk solution simultaneously. In the reaction mixture, there is a high degree of supersaturation with respect to ZnO or $Zn(OH)_2$, which consequently induces the formation of ZnO solid in the bulk solution through homogeneous nucleation as well as on the surface of the pre-existing nuclei.

A method was developed in our lab for growing long ZnO nanowires solely on seeded substrates based on suppressing the homogeneous nucleation while maintaining the growth of pre-existing nuclei.[45] As a result, long, aligned ZnO nanowires could be obtained at a very fast rate without any contamination brought about due to growth of nanowires in the bulk solution. To suppress the homogeneous nucleation, the degree of supersaturation in the reaction system needs to be decreased. This was achieved by introducing ammonium hydroxide to the growth solution. Ammonium hydroxide forms complexes with the Zn ions,

$$Zn^{2+} + nNH_3 \leftrightarrow Zn(NH_3)_n^{2+}$$

where n = 1,2,3, or 4. The complexes also serve as a buffer for Zn^{2+}; it continuously supplies Zn^{2+} while lowering the degree of supersaturation of the reaction system. The use of ammonium hydroxide substantially suppresses ZnO homogeneous nucleation. However, by using ammonium hydroxide alone to effectively prevent formation of ZnO in the liquid phase, a high concentration of ammonium hydroxide is required, which also results in very slow growth of the wires on the seeded substrate due to excessively low degree of supersaturation.

To avoid this, polyethyleneimine (PEI) was added to further suppress the homogeneous nucleation process. It was found that in the presence of both PEI and ammonium hydroxide, formation of ZnO in the bulk solution can be effectively prevented while ZnO nanowires could still grow at a reasonably high growth rate. This is because PEI preferentially adsorbs to certain crystal faces of ZnO clusters and inhibits further crystal growth along these faces.[46] In the homogeneous nucleation case, the ZnO clusters initially formed due to thermal fluctuation is so small that the polymer chain of PEI adsorbed to certain crystal faces is long enough to cover other faces and, as a result, the steric hindrance of the PEI chain inhibits the crystal growth along all faces. Consequently, the clusters have a very small chance to grow to the critical size that

thermodynamically favors the growth of crystals. On the seeded substrates, however, the pre-existing seeds are large enough (5-20 nm) that despite PEI adsorption to certain crystal faces, the growing faces remain exposed to the reactants. Therefore, growth of ZnO nanowires can normally occur on the seeded substrates. The significance of this discovery was that ZnO nanowires now may grow on seeded substrates without precipitation in the bulk solution at a reasonable degree of supersaturation through coupled use of ammonium hydroxide and PEI.

2.1 EXPERIMENTAL METHOD

ZnO nanowire arrays were grown directly on indium doped tin oxide (ITO) glass substrates. The conducting glass substrates were first cleaned by acetone/ethanol sonication and rinsed thoroughly with DI water. The substrates were then subjected to ultra-violet ozone to remove any residual organics. The clean substrates were then seeded by spin coating with 5 mM zinc acetate solution in ethanol followed by thermal decomposition at 300ºC. The seeded substrates are placed in an aqueous growth solution containing 0.025 M zinc nitrate, 0.0125 M hexamethylenetetraamine, 0.005 polyethylenimine and 0.35 M ammonium hydroxide at 90ºC for 6 hours. The synthesized ZnO nanowire arrays were then rinsed with DI water and calcinated in air at 450ºC for 1 hour. **Figure 4** shows a representative cross-section scanning electron microscope image of ZnO nanowires grown on an ITO substrate. The length of the nanowires was approximately 10 µm and the diameter was 150-200 nm. **Figure 5** shows the X-Ray diffraction (XRD) pattern the ZnO nanowires. A very strong peak was observed corresponding to the (002) plane of ZnO. The peak corresponding to this plane was significantly stronger than the

(101), (102) and (103) peaks, indicating a strong texture effect in accordance with *c*-axis elongated nanowires oriented normal to the substrate.

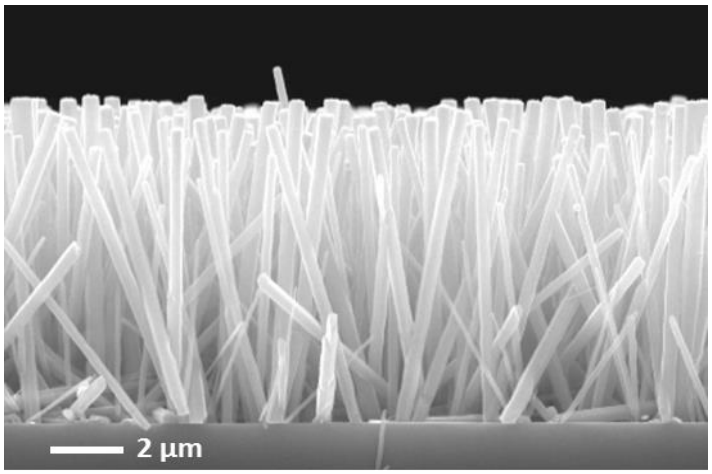

Figure 4. Scanning electron microscope (SEM) image of ZnO nanowire arrays

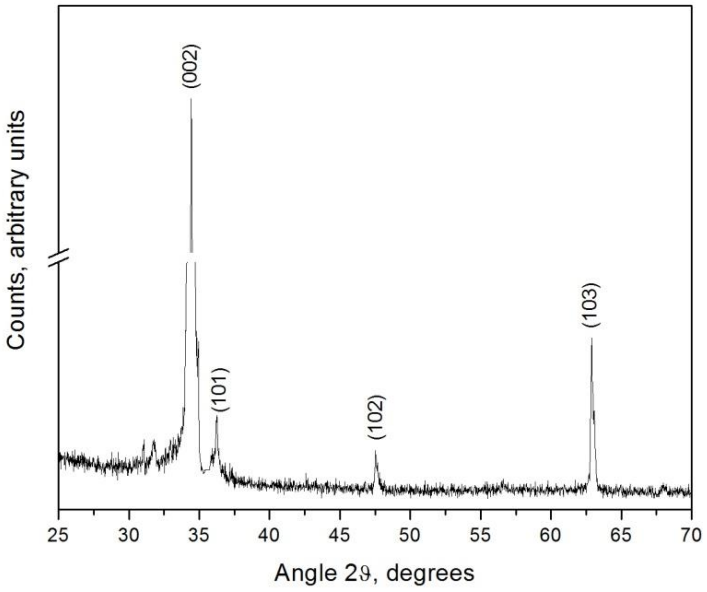

Figure 5. X-Ray Diffraction Spectra of ZnO nanowire arrays

3.0 ORDERED TIN OXIDE NANOTUBE ARRAYS FOR DYE-SENSITIZED SOLAR CELLS

3.1 INTRODUCTION

As discussed earlier, highest efficiencies for DSCs have been reported using a nanoparticle TiO_2 network.[12] The main advantage of using such a random nanoparticle network is the high surface area available for dye adsorption leading to improved light harvesting. However, further improvements in device performance have been limited mainly due to the poor electron transport characteristics of TiO_2 and the inherent problem of electron recombination in nanoparticle films. In addition to TiO_2, various wide band-gap metal oxide semiconductors, including ZnO,[46] SnO_2 [47] and Nb_2O_5 [48] have been studied for their potential use as photoanodes in DSCs. Among these, SnO_2 is one of the most promising wide band-gap semiconductor materials for DSCs. Bulk electron mobility in SnO_2 (μ_e=100-200 $cm^2V^{-1}s^{-1}$)[49] is orders of magnitude higher than TiO_2 (μ_e< 1 $cm^2V^{-1}s^{-1}$)[50] and comparable to ZnO nanowires (μ_e= 200 $cm^2V^{-1}s^{-1}$).[51] The high electron mobility may open up possibilities to further improve DSCs, for example, by using redox mediators with faster kinetics than currently used ones.[52, 53] Very fast electron injection into SnO_2 from the excited dye molecules has also been reported (≈ 150 ps) which is comparable to TiO_2.[54] Furthermore, use of SnO_2 as a

photoanode may make the DSC less susceptible to UV degradation, due to the large band gap of SnO_2, leading to better long-term stability than DSCs employing ZnO or TiO_2 electrodes.[55, 56]

Mesoporous films of SnO_2 nanoparticles have been used as photoanodes in DSCs.[48, 57] The efficiencies of these DSCs, however, have been less than those using TiO_2 nanoparticles. The open-circuit voltage (V_{OC}) of SnO_2 nanoparticle-based DSCs has been limited to less than 0.4 V.[47, 48, 57, 58] Such a small V_{OC} prohibits further exploration of using mesoporous films of SnO_2 nanoparticles as photoanodes for DSCs. As a promising alternative to sintered nanoparticles, 1-D nanostructures facilitate electron transport by providing a direct conduction pathway for the electrons. Gubbala *et al* has used SnO_2 nanowires as photoanodes in DSCs, and a V_{OC} of 0.56 V is obtained, a 0.2 V increase compared to DSCs that use sintered SnO_2 nanoparticles.[58] Although a V_{OC} of 0.56 V is still too low to be considered for DSC applications, this result indicates that 1-D nanostructures may overcome some of the limitations of sintered nanoparticles. The SnO_2 nanowires in their DSCs, however, are randomly placed on the substrate, and therefore the advantages of 1-D nanostructures may not be fully taken. In DSCs, photogenerated electrons need to travel through the sensitized film to be collected before they recombine. Apparently, aligning the 1-D nanostructures vertically across the thickness of the sensitized film, compared to random placement, provides a significantly more efficient path for electron transport and thus can reduce the recombination probability of photogenerated electrons. In addition, vertically aligned 1-D nanostructures also provide straight channels for filling the sensitized film with solid-state electrolytes, which is a promising approach to solve the packaging challenge and improve the long-term stability of DSCs. Therefore, vertically aligned 1-D nanostructures have recently attracted considerable interest for their potential use as photoanodes in DSCs. Both vertically aligned ZnO nanowires[45, 46] and TiO_2 nanotubes[59]

have been used to fabricate DSCs and, indeed, faster electron transport and improved electron collection efficiency, compared to photoanodes based on sintered nanoparticles, has been reported. DSCs fabricated by using vertically aligned SnO_2 1-D nanostructures, however, have not been reported, primarily due to the difficulty in synthesis of such nanostructures.

Here, we report a method for synthesizing vertically aligned SnO_2 nanotube arrays by using ZnO nanowire arrays as a sacrificial template. The sacrificial ZnO nanowires are converted to SnO_2 nanotubes via liquid-phase SnO_2 deposition and simultaneous ZnO dissolution. The resulting SnO_2 nanotube arrays are used to fabricate DSCs, showing improved photovoltaic performance compared to SnO_2 nanoparticle-based devices. In addition, it is found that coating the SnO_2 nanotubes with a conformal thin layer of TiO_2 leads to significant increase in open circuit voltage (V_{OC}) and fill factors (*ff*) for the DSCs, resulting in much higher efficiencies. Transient photovoltage measurements indicate that the photogenerated electron lifetime in the hybrid TiO_2-SnO_2 nanotubes is substantially longer than in TiO_2 nanoparticles, TiO_2 nanotubes, and ZnO nanowires, suggesting promises of the TiO_2-coated SnO_2 nanotubes for further improvement of DSCs.

3.2 EXPERIMENTAL METHODS

3.2.1 Growth of ZnO Nanowire Arrays

ZnO nanowire arrays were grown directly on indium doped tin oxide (ITO) glass substrates by method described in Section **2.1**.

3.2.2 Conversion to SnO_2 Nanotube Arrays

The synthesized ZnO nanowire arrays were rinsed with DI water and calcined in air at 450°C for 1 hr. The nanowire array was then placed in an aqueous solution of 0.09 M ammonium hexafluorostannate ($(NH_4)_2SnF_6$) and 0.1 M H_3BO_3 at room temperature for 30 min, which resulted in the formation of vertical SnO_2 nanotube array. For preparing the aqueous solution, 0.15 M bulk solution of ammonium hexafluorostannate (AHFS) ($(NH_4)_2SnF_6$) (Aldrich) was prepared by dissolving 4 g AHFS in 100 ml water. The aqueous solution for conversion was prepared by mixing 3 ml of 0.15 M AHFS, 1 ml of 0.5 M H_3BO_3 and 1 ml water. The synthesized SnO_2 nanotube array was then calcined in air at 450°C for 1 hr.

3.2.3 Synthesis of Hybrid TiO_2-SnO_2 Nanotube Arrays

For synthesizing hybrid TiO_2-SnO_2 nanotube arrays, a thin layer of TiO_2 was deposited on the surface of SnO_2 nanotubes by immersing the SnO_2 nanotube array in a solution of 0.1 M $(NH_4)_2TiF_6$ and 0.2 M H_3BO_3 for 20 min. This solution was prepared by mixing 3 ml of 0.1667 M bulk solution of ammonium hexaflurotitanate (AHFT) ($(NH_4)_2TiF_6$, Aldrich), prepared by dissolving 3.3 g AHFT in 100 ml water, and 2 ml of 0.5 M H_3BO_3.

3.2.4 Synthesis of TiO_2 Nanoparticles

TiO_2 nanoparticle-based electrode was prepared by applying a paste of TiO_2 nanoparticle onto the conducting substrate (ITO) by doctor blading. The paste used consisted of commercially procured TiO_2 nanoparticles (15 nm) dissolved in 10 ml ethanol and 0.2 ml isopropoxide. The

TiO_2 nanoparticle film obtained by this method was 10-11 µm thick. The method used for synthesizing TiO_2 nanotubes has been published by our group before.[59]

3.2.5 Fabrication and Characterization of DSCs

The area of the photoanodes was limited to about 0.5 cm^2. The excess tubes was removed from the substrate with a blade. The films were immersed in 0.5 mM (Bu4N)2[Ru(4,4'-(COOH)-2,2-bipyridene)2(NCS)2] (N719 dye) solution in ethanol overnight. A 60 µm thick hot melt sealing foil (SX1162-60, Solaronix) frame was sandwiched between the sensitized photoanode and the counter-electrode with one side left open. The counter-electrode used was platinized ITO electrode and was prepared by decomposing a Pt salt (H_2PtCl_6) at a temperature of 400°C. A solution consisting of 0.1 M LiI, 0.1 M I_2, 0.5 M tert-butyl pyridine, and 0.6 M tetrabutylammonium iodide in acetonitrile was introduced from the open end of the sealing frame. The open end was then immediately sealed with silicone adhesive. The cells were then immediately tested under 100 mW/cm^2 AM 1.5G simulated sunlight (Model 67005, Oriel) and the *J-V* curve was recorded using Reference 600 potentiostat (Gamry Instruments). Photovoltage decay measurements were performed using the same light source and Reference 600 potentiostat. Electrochemical Impedance Spectroscopy (EIS) studies were performed under both 100 mW/cm^2 AM 1.5G simulated sunlight and dark conditions. The impedance spectra were obtained over a frequency range of 0.01-100 kHz. The magnitude of the alternative signal was 20 mV.

3.3 RESULTS AND DISCUSSIONS

Figure 6 schematically shows the process for synthesizing vertically aligned SnO_2 nanotube arrays by using ZnO nanowires as a sacrificial template. The process starts with growing vertically aligned ZnO nanowires on ITO-coated glass substrate by a hydrothermal method. This is followed by conversion of ZnO nanowire arrays to SnO_2 nanotubes via SnO_2 deposition and simultaneous ZnO dissolution by placing the ZnO nanowire array in an aqueous solution of $(NH_4)_2SnF_6$ and H_3BO_3. The conversion process can be described by the following chemical reactions:[59-61]

$$SnF_6^{2-} + 2H_2O \rightarrow SnO_2 + 6F^- + 4H^+ \quad (3.1)$$

$$H_3BO_3 + 4HF \rightarrow HBF_4 + 3H_2O \quad (3.2)$$

$$ZnO + 2H^+ \rightarrow Zn^{2+} + H_2O \quad (3.3)$$

During the conversion process, $(NH_4)_2SnF_6$ hydrolyses on the surface of the nanowires resulting in the deposition of SnO_2 on the surface of ZnO nanowires. $(NH_4)_2SnF_6$ hydrolysis also results in formation of acids which aid in the dissolution of ZnO. It should be noted that a small amount of HF may be present in the solution post the conversion process and necessary precautions were taken.

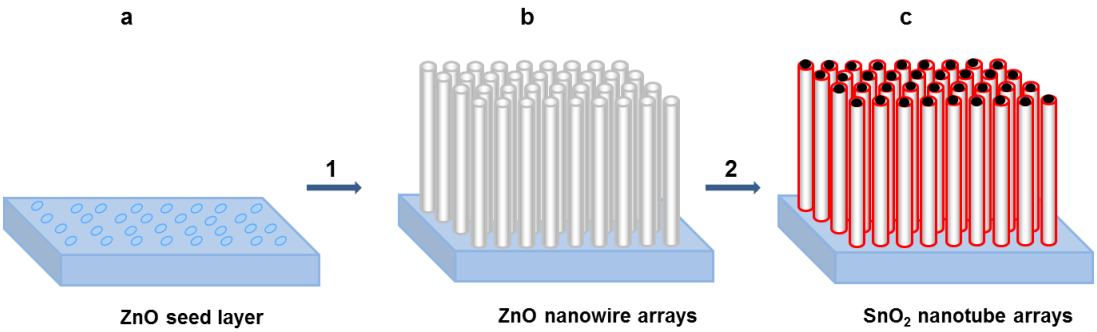

Figure 6. Schematic illustration of the process for synthesizing vertically aligned SnO_2 nanotube arrays.

3.3.1 Morphological Characterization

Figure 7a shows a representative cross-section SEM image of a ZnO nanowire array synthesized by the hydrothermal method previously developed by our group and discussed in Section **2.1**.[45] The wires are 10 µm in length and 150-200 nm in diameter. **Figure 7b** and **Figure 7c** show representative cross-section and top-view SEM images of a SnO_2 nanotube array. It is observed that the SnO_2 nanotubes retain the length of ZnO wires, most of them are open at the top end, and the hollow cores have approximately the same width as the original ZnO wires. **Figure 7d** shows energy dispersive X-ray (EDX) spectra recorded before (curve a) and after (curve b) the conversion process. In comparison to curve a, curve b shows strong peaks for Sn and O and no detectable peak for Zn, indicating that all the ZnO nanowires have been converted to SnO_2 nanotubes.

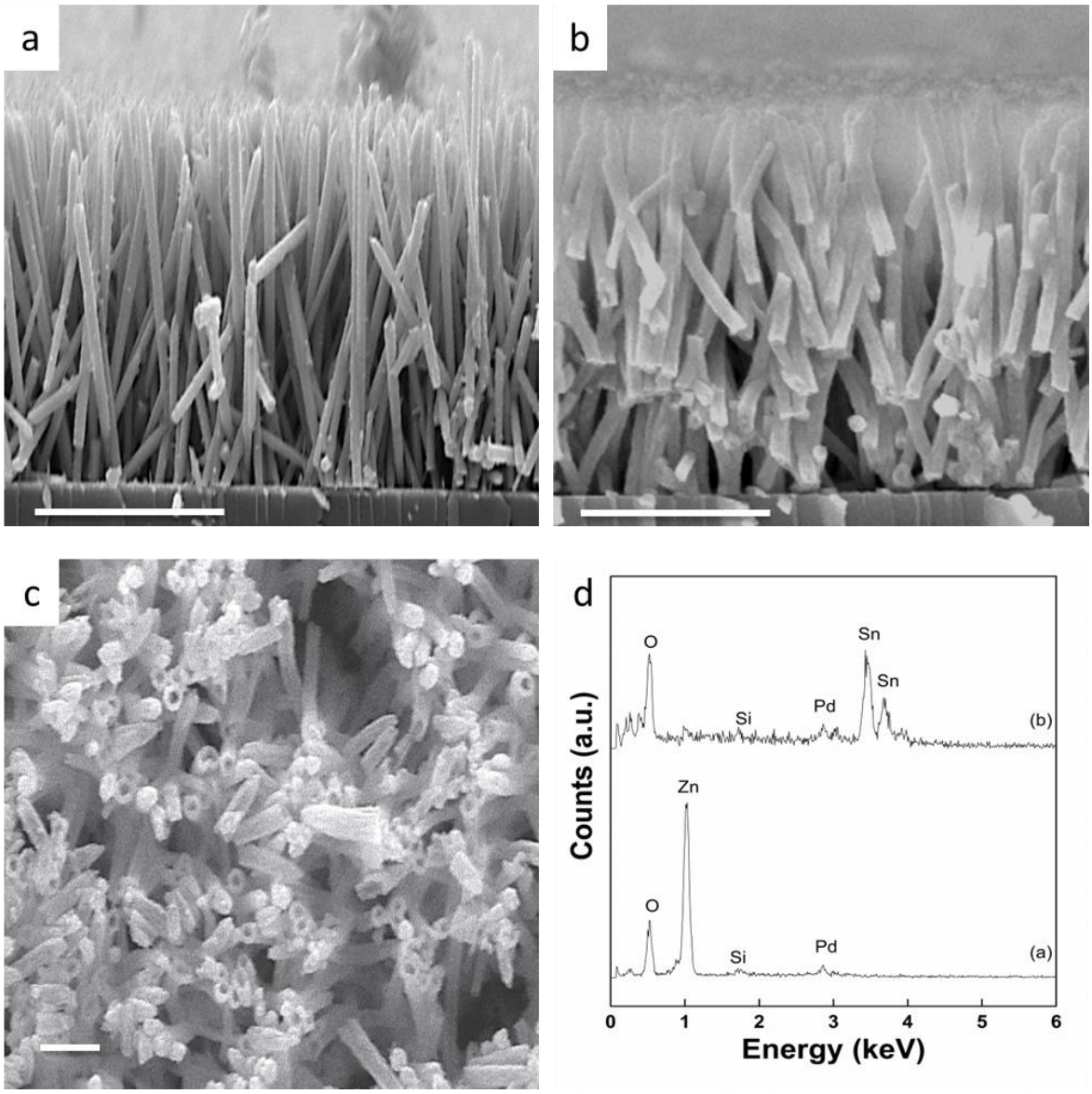

Figure 7. ZnO nanowires and converted SnO_2 nanotube arrays. (a) SEM image of ZnO nanowire array on ITO. Scale bar, 5 μm. (b) SEM image of converted SnO_2 nanotube array. Scale bar, 5 μm. (c) Top-view SEM image of SnO2 nanotube array. Scale bar, 2 μm. (d) EDX spectra for ZnO nanowire array, curve a, and SnO_2 nanotube array after conversion, curve b.

3.3.2 Determination of Crystal Structure

Figure 8a shows the X-Ray diffraction (XRD) pattern for the SnO_2 nanotubes. The XRD pattern can be indexed to tetragonal rutile structured SnO_2 (JCPDS card no. : 41-1445). No peaks corresponding to crystalline ZnO were detected, confirming the conversion of ZnO nanowires to SnO_2 nanotubes. The as-synthesized SnO_2 nanotubes are polycrystalline. The size of individual SnO_2 crystals in the polycrystalline nanotubes was estimated by using the Scherrer equation, $D = 0.89\lambda / \beta(\cos\theta)$, where λ is the wavelength of the X-ray (1.54056 Å), β is the peak width at half-maximum in radians, and θ is the Bragg's angle.[62, 63] Using this equation, the mean particle size was estimated to be 3.3 nm on the basis of the (110) peak. **Figure 8b** shows a transmission electron microscopy (TEM) image of an individual SnO_2 nanotube, where the hollow core and a wall of 15-20 nm thick can be clearly seen. **Figure 8c** shows a high-resolution TEM (HRTEM) image of the wall of an individual SnO_2 nanotube. The lattice spacing of 0.34 nm shown in **Figure 8c** corresponds to the (110) plane of SnO_2.

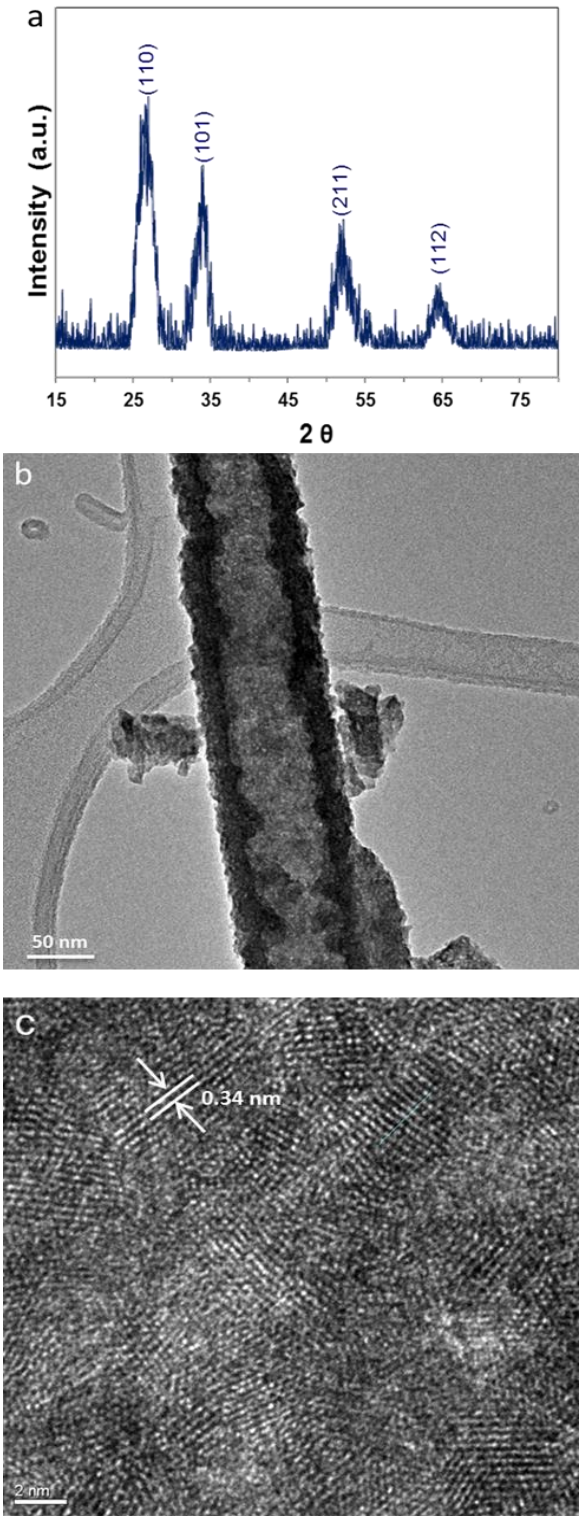

Figure 8. (a) X-ray diffraction pattern for SnO_2 nanotube array. (b) TEM image for a single SnO_2 nanotube. (c) HRTEM image, showing lattice spacing corresponding to (110) plane for SnO_2.

3.3.3 J-V Characterization

The synthesized SnO_2 nanotubes were then used to fabricate DSCs. **Figure 9** shows the photovoltaic performance of a representative DSC based on SnO_2 nanotube arrays. The DSC yielded an efficiency of 1.13% with a short-circuit current (J_{SC}) of 8.05 mA/cm^2 and a V_{OC} of 0.50 V. The V_{OC} obtained is almost 0.20 V higher than those reported for SnO_2 nanoparticle based DSCs.[47, 58] This increase in V_{OC} could be attributed mainly to the faster electron transport and lower recombination rates for the nanotube based DSC. These factors were verified by studying the recombination kinetics discussed later. The measured J_{SC} was significantly higher than the previously reported J_{SC} for similar DSCs based on SnO_2 1-D nanostructures.[64] This could be mainly attributed to the higher roughness factor, resulting from longer nanotubes of our arrays, compared to previously reported SnO_2 1-D nanostructures. Increase in roughness factor would imply higher dye loading and consequently higher light harvesting efficiency and higher current densities.

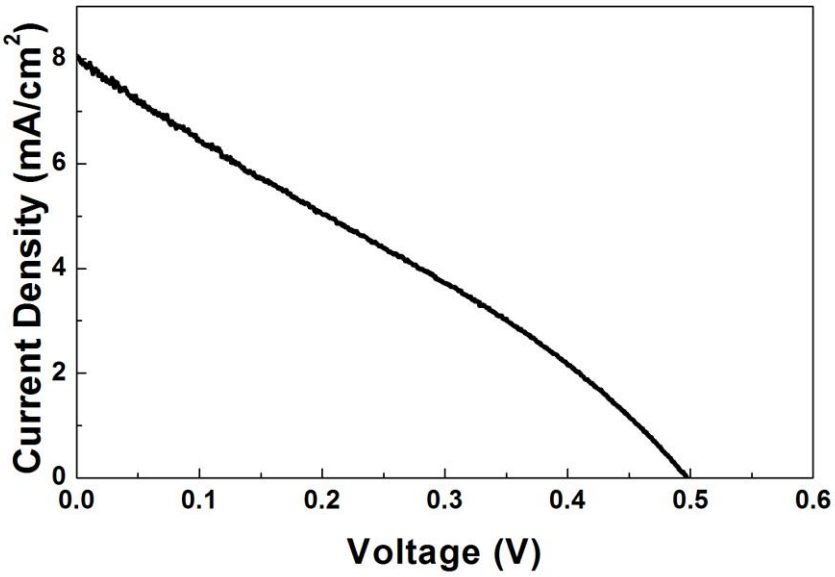

Figure 9. J-V characteristics of DSCs based on SnO_2 nanotube arrays as photoanode.

However, V_{OC} and fill factors (*ff*) for these devices are still low when compared to typical TiO_2-based devices, which is characteristic of SnO_2 as a photoanode.[58, 64, 65] Efficiency of DSCs based on photoanodes of SnO_2 has been shown to improve by coating the surface of SnO_2 with a conformal barrier layer such as TiO_2 or Al_2O_3.[47, 55, 65] As can be seen from the band-edge diagram in **Figure 10**, the conduction band of TiO_2 lies between that of the N719 dye and SnO_2. Hence, the electrons injected into TiO_2 from the dye would be readily injected into the SnO_2 nanotube array. This should result in better electron transfer from the dye to the current collecting surface. The TiO_2 layer would also act as a barrier layer, thereby preventing back transfer of electrons which have been injected in the photoanode. This should result in significant reduction of recombination losses and hence improve device performance.

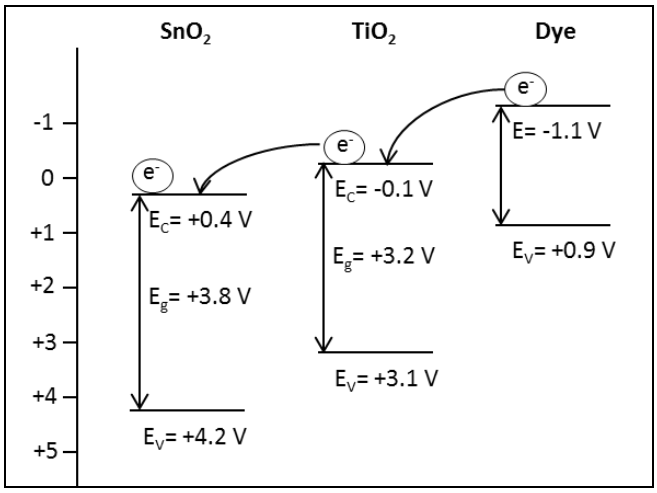

Figure 10. Energy band diagram of SnO_2, TiO_2 and N 719 dye with respect to the electrochemical scale at pH=1

3.3.4 Characterization and Performance of Hybrid Nanotubes

We here use a liquid-phase deposition method to coat the walls of SnO_2 nanotubes with a thin layer of TiO_2. The method involved immersing SnO_2 nanotube array in a solution of $(NH_4)_2TiF_6$ and H_3BO_3 for up to 30 min, and the deposition of TiO_2 can be described by the following chemical reactions:[66]

$$TiF_6^{2-} + 2H_2O \rightarrow TiO_2 + 6F^- + 4H^+ \quad (3.4)$$

$$H_3BO_3 + 4HF \rightarrow HBF_4 + 3H_2O \quad (3.5)$$

Figure 11a and **Figure 11b** show an SEM image and an EDX spectrum, respectively, of the SnO_2 nanotube array coated with TiO_2, indicating fairly uniform deposition of TiO_2 while retaining the morphology of the original SnO_2 nanotube array. **Figure 11c** and **Figure 11d** show a TEM image and a line-scan EDX profile, respectively, of a single TiO_2-coated SnO_2 nanotube, confirming uniform deposition of a 20-25 nm thick TiO_2 layer on the SnO_2 nanotube.

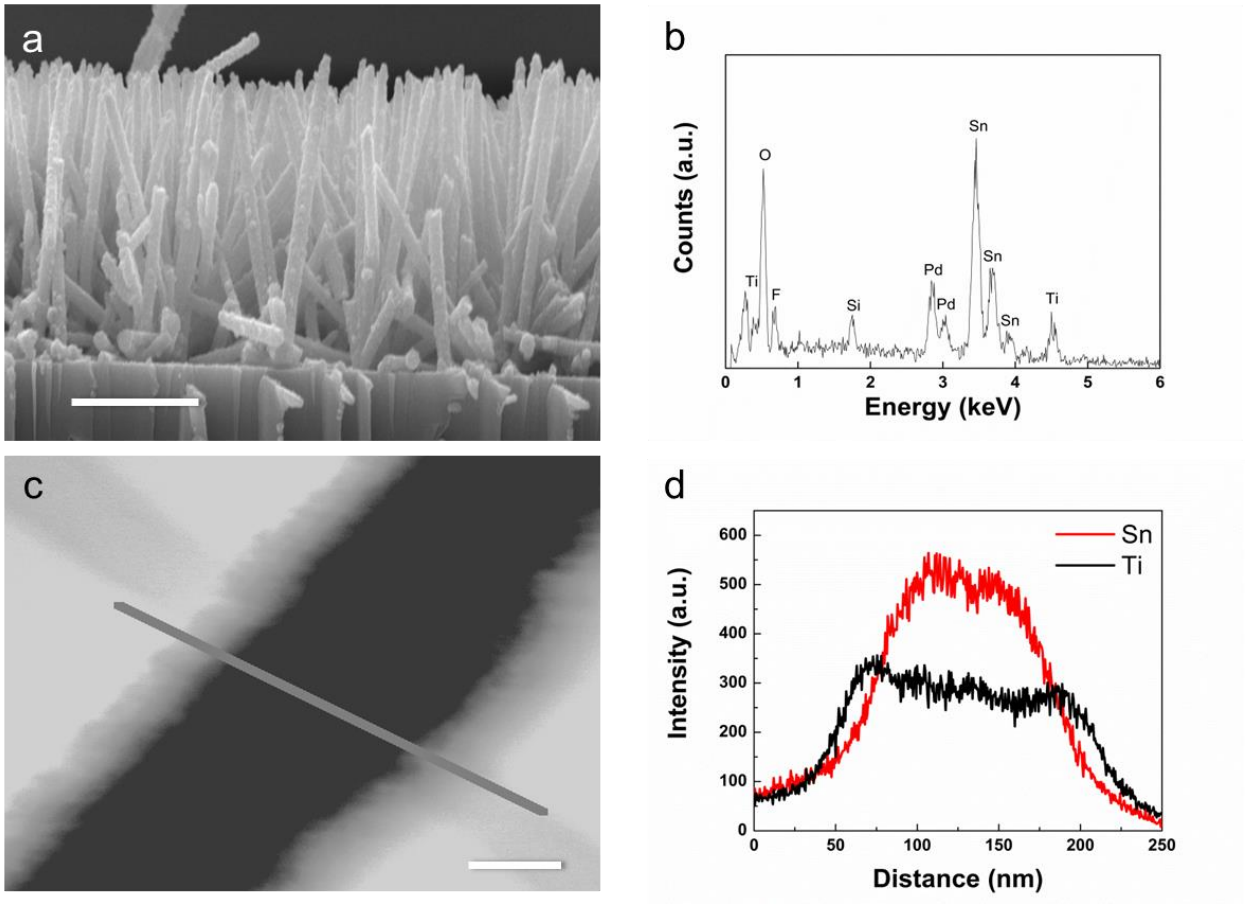

Figure 11. SnO_2 nanotubes coated with TiO_2. (a) SEM image. Scale bar, 5μm. (b) EDX spectra. (c) TEM image of a TiO_2-coated SnO_2 nanotube. Scale bar, 50nm. (d) Line-scan EDX profile obtained along the line shown in (c).

We then fabricated DSCs using these hybrid TiO_2-SnO_2 nanotubes. A representative J-V characteristic of these DSCs is shown in **Figure 12**. The photovoltaic performances of DSCs based on (i) SnO_2 nanotubes and (ii) hybrid TiO_2-SnO_2 nanotubes are summarized and compared in **Table 3**. In comparison, coating the SnO_2 nanotubes with a thin layer of TiO_2 led to a significant improvement in V_{OC} and *ff* —V_{OC} increased from 0.50 to 0.70 V, and *ff* from 0.28 to 0.50. The much improved photovoltaic performance could be mainly attributed to slower recombination rates due to surface passivation of sub-band-edge surface states.[49] Also, the conduction band-edge of SnO_2 is 0.4 V more positive than TiO_2.[58] Thus the electrons injected into TiO_2 from the dye would be readily injected into the SnO_2 nanotubes, allowing fast electron transport to the current-collecting surface. TiO_2 forms an energy barrier forcing electrons to travel towards the current-collecting surface.[55, 58] These factors result in considerable reduction in recombination rate leading to improved V_{OC}. The increase in J_{SC} could be attributed to better dye uptake by the hybrid TiO_2-SnO_2 nanotubes. The increase in J_{SC}, V_{OC} and *ff* lead to significant increase in the efficiency of DSC.

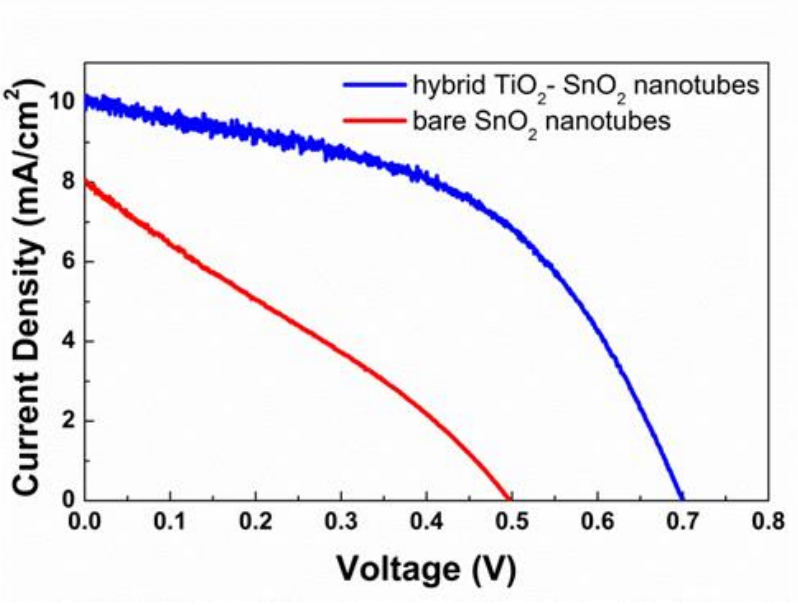

Figure 12. J-V characteristics of DSCs using SnO_2 nanotube arrays with (blue curve) and without (red curve) TiO_2 coating.

Table 3. Photovoltaic performance of DSCs based on (i) bare SnO_2 nanotubes and (ii) TiO_2-coated SnO_2 nanotubes

	Bare SnO_2 nanotubes	**TiO_2-coated SnO_2 nanotubes**
J_{SC} (mA/cm^2)	7.99 ± 0.06	9.91 ± 0.17
V_{OC} (V)	0.49 ± 0.01	0.68 ± 0.02
ff	0.27 ± 0.01	0.49 ± 0.01
η (%)	1.06 ± 0.07	3.47 ± 0.06

Our best performing cell delivered an efficiency of 3.53%, with J_{SC} of 10.08 mA/cm^2, V_{OC} of 0.70 V, and *ff* of 0.50. This efficiency is still low when compared to typical TiO_2 nanoparticle-based DSCs. This is mainly due to the low internal surface area of our nanotube arrays when compared to a nanoparticle film. This results in lower dye adsorption and hence lower light absorption. This constraint may be overcome by synthesizing longer nanotubes. In the next chapter we have reported a method for synthesizing multilayer ZnO nanowire arrays with lengths of up to 40 μm.[66] Work is currently underway to convert these multilayer assemblies into SnO_2 nanotubes.

3.3.5 Photovoltage Decay Measurements

To further understand the performance of DSCs based on SnO_2 nanotubes and hybrid TiO_2-SnO_2 nanotubes, transient photovoltage measurements were conducted, by monitoring the V_{OC} as a function of time upon turning off the illumination. The idea behind performing these experiments was to study the electron recombination kinetics. The experiments were repeated with DSCs based on TiO_2 nanoparticles, TiO_2 nanotubes, and ZnO nanowires of same thickness and the results were compared. **Figure 13a** shows V_{OC} decay as a function of time for five different anodes: (i) TiO_2-coated SnO_2 nanotubes, (ii) SnO_2 nanotubes, (iii) TiO_2 nanotubes, (iv) ZnO nanowires, and (v) TiO_2 nanoparticles. It was observed that DSCs based on TiO_2-coated SnO_2 nanotubes and SnO_2 nanotubes showed much slower V_{OC} decay rate than DSCs based on the other three electrodes, indicating much slower recombination rates. From the V_{OC} decay rate, the photoelectron recombination lifetime (τ_r) may be determined by the following equation:[67, 68]

$$\tau_r = -\left(\frac{k_B T}{e}\right) \times \left(\frac{dV_{OC}}{dt}\right)^{-1}, \tag{3.6}$$

where k_B is the Boltzmann constant and T is temperature. The calculated τ_r is plotted in **Figure 13b** for five different electrodes. It is observed that τ_r for TiO_2-SnO_2 nanotubes, SnO_2 nanotubes, and TiO_2 nanotubes are almost two orders of magnitude higher than TiO_2 nanoparticles. They are also much higher than the literature reported τ_r for SnO_2 nanoparticles.[58]

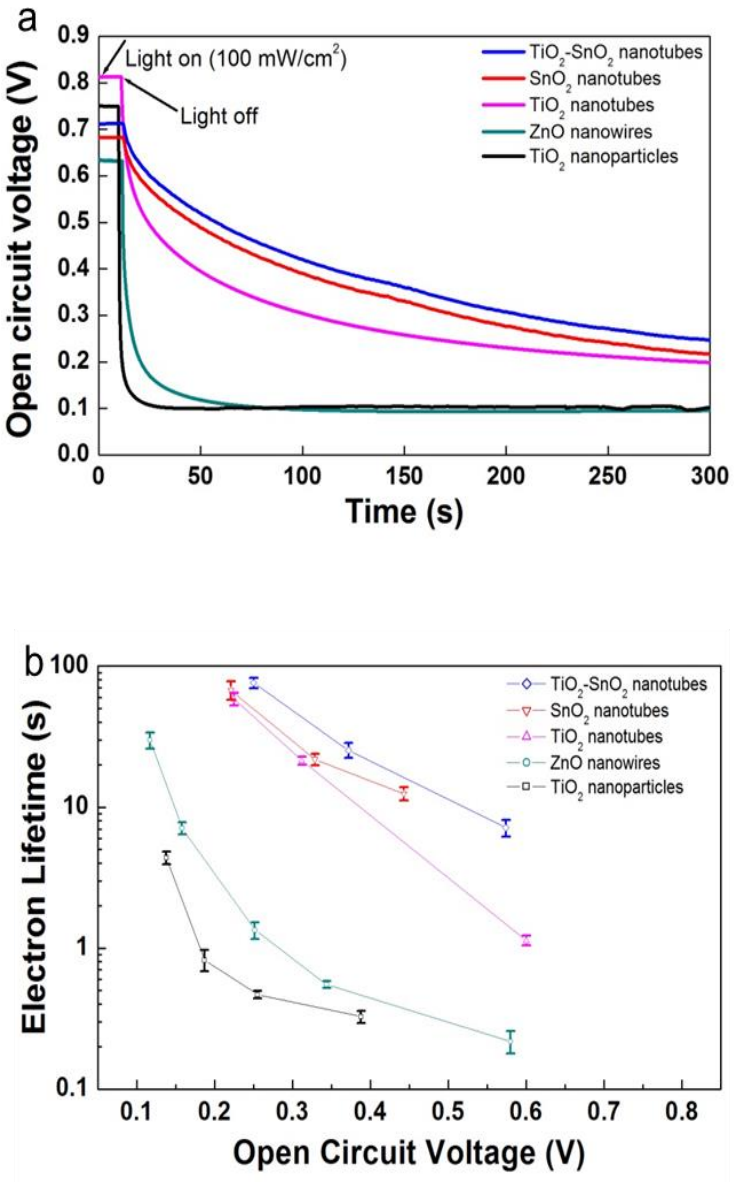

Figure 13. Open-circuit voltage decay curve and calculated electron recombination lifetime for five different anodes: (i) TiO_2-coated SnO_2 nanotubes, (ii) SnO_2 nanotubes, (iii) TiO_2 nanotubes, (iv) ZnO nanowires, and (v) TiO_2 nanoparticles. (a) Voltage-decay curve. (b) Electron lifetime determined from open-circuit voltage decay measurement.

The much larger τ_r in the nanotubes compared to nanoparticle films may be explained by an internal radial electric field that is developed within the walls of the nanotubes. The wall of the tubes is thick enough to develop a potential difference. This potential difference drives the electrons inwards, away from the interface, thereby preventing the recombination reaction.[59] The primary reason for longer lifetimes in TiO_2 based nanotubes as compared to ZnO nanowires is due to the intrinsic material properties. It has been reported that the conduction band of TiO_2 is composed of d-orbital electrons that are less susceptible to recombination than the electrons in ZnO.[69] Among the five different electrodes, the hybrid TiO_2-SnO_2 electrode exhibits slowest recombination rates, slightly slower than the bare SnO_2 nanotube arrays. This could be due to the energy barrier formed by the TiO_2 coating, forcing the electrons to flow towards the current collecting surface and preventing the electrons from flowing in the opposite direction. Introduction of TiO_2 may have also passivated the reactive low-energy SnO_2 surface states.[49] These factors lead to further lowering the recombination rates, resulting in enhanced V_{OC} and *ff* for DSCs based on the hybrid TiO_2-SnO_2 electrodes. To ensure a fair comparison for the various photoanodes tested for open-circuit voltage decay, we tried to ensure a uniform film thickness of approximately 10 μm for all devices. The photovoltaic performance of DSCs fabricated using the different photoanodes used for comparison in these studies is tabulated in **Table 4**.

Table 4. Photovoltaic performance data of DSCs based on different electrodes used for open-circuit voltage decay study experiments.(i) TiO_2 nanoparticles, (ii) ZnO nanowires, (iii) TiO_2 nanotubes, (iv) Bare SnO_2 nanotubes, (v) TiO_2-coated SnO_2 nanotubes

	TiO_2 Nanoparticles	**ZnO Nanowires**	**TiO_2 Nanotubes**	**Bare SnO_2 Nanotubes**	**TiO_2-coated SnO_2 nanotubes**
J_{SC} (mA/cm^2)	12.8	5.20	6.50	8.05	10.08
V_{OC} (V)	0.82	0.56	0.76	0.50	0.70
ff	0.66	0.36	0.60	0.28	0.50
η (%)	6.93	1.05	2.96	1.13	3.53

3.3.6 Electrochemical Impedance Spectroscopy Studies

We also performed electrochemical impedance spectroscopy (EIS) to further understand the improved performance of the hybrid electrodes. **Figure 14a** shows the Nyquist plots for DSCs based on hybrid TiO_2-SnO_2 and bare SnO_2 nanotubes obtained by EIS carried out under illumination of AM 1.5G simulated sunlight at an applied bias of V_{OC}. The impedance components of the interfaces in the DSCs are observed in three different frequency regimes. The arcs observed in the EIS spectra may be assigned to the impedances due to conducting layer/semiconductor interface, Pt/electrolyte interface, and photoanode/dye/electrolyte interface.[70, 71] In the middle frequency range of 0.1 – 10^4 Hz, the semicircle on the Nyquist plot is associated with the charge transfer across the photoanode/dye/electrolyte interface and the size of the semicircle represents the resistance to recombination.

As can be seen from the Nyquist plots in **Figure 14a**, the semicircle observed in the middle frequency range is larger in the case of hybrid TiO_2-SnO_2 nanotube photoanode than that for bare SnO_2 nanotube photoanode. This indicates increased recombination resistance which results in lower recombination rates at the photoanode/dye/electrolyte interface for DSCs using the hybrid TiO_2-SnO_2 photoanodes. The electron lifetime, τ_r, can be estimated from the maximum angular frequency of the impedance semicircle arc at middle frequencies, according to the relation:

$$\tau_r = \frac{1}{2\pi f_{\max}} \tag{3.7}$$

where f_{max} is the maximum frequency of the mid-frequency peak.[65] Thus, a peak shift to a lower frequency represents longer electron recombination lifetime. For DSCs with hybrid TiO_2-SnO_2 photoanode, a longer electron lifetime of 18.9 ms is obtained compared to 12.8 ms for DSCs based on bare SnO_2 photoanode. The longer electron recombination lifetime of hybrid TiO_2-SnO_2 photoanode compared to bare SnO_2 photoanode is in agreement with the trend observed in the transient photovoltage measurement. It needs to be noted that the absolute values for recombination lifetimes obtained by EIS differ from those reported by photovoltage decay measurements. The primary reason for this could be that, in photovoltage decay measurements, the cell was allowed to decay through low carrier density states resulting in longer electron lifetimes. On the other hand, EIS measurements were performed at open-circuit voltage, when electron density is the highest.

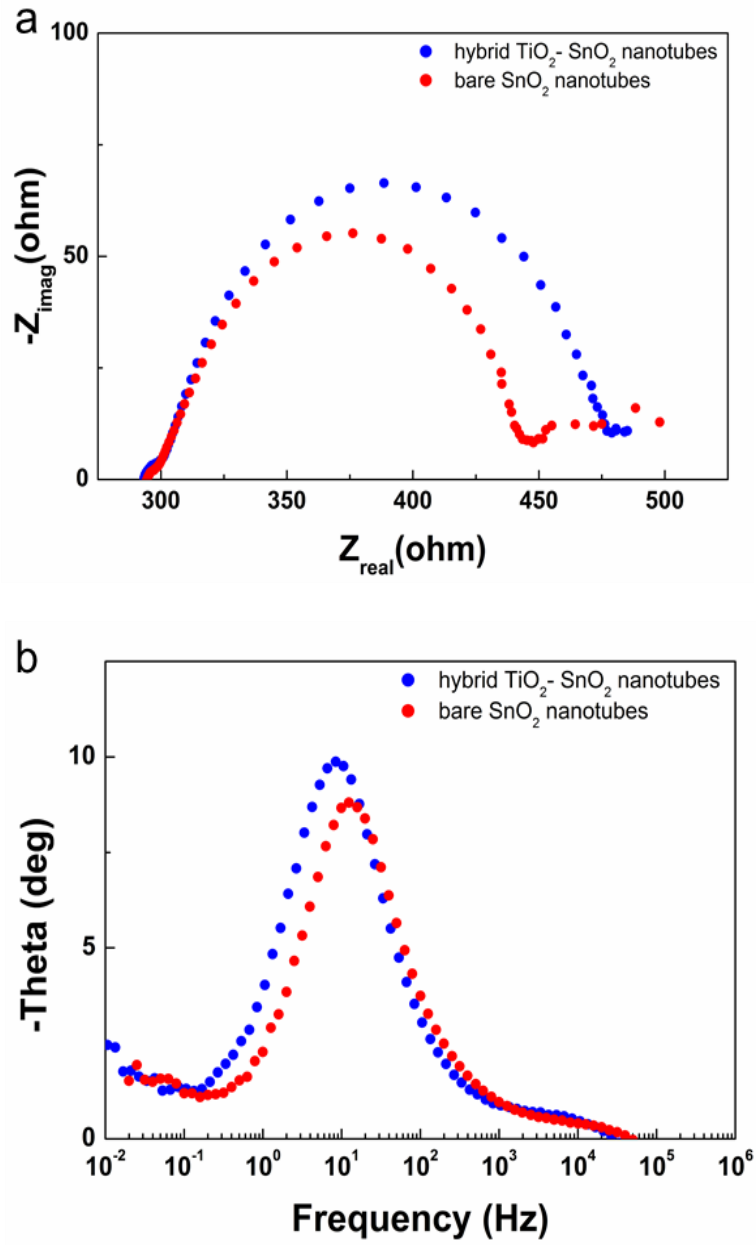

Figure 14. Electrochemical impedance spectroscopy (EIS) for DSCs based on (i) hybrid TiO_2-SnO_2 nanotubes and (ii) bare SnO_2 nanotube arrays under illumination of AM 1.5G simulated sunlight at an applied bias of V_{OC}. (a) Nyquist plots. (b) Bode phase angle versus frequency plots

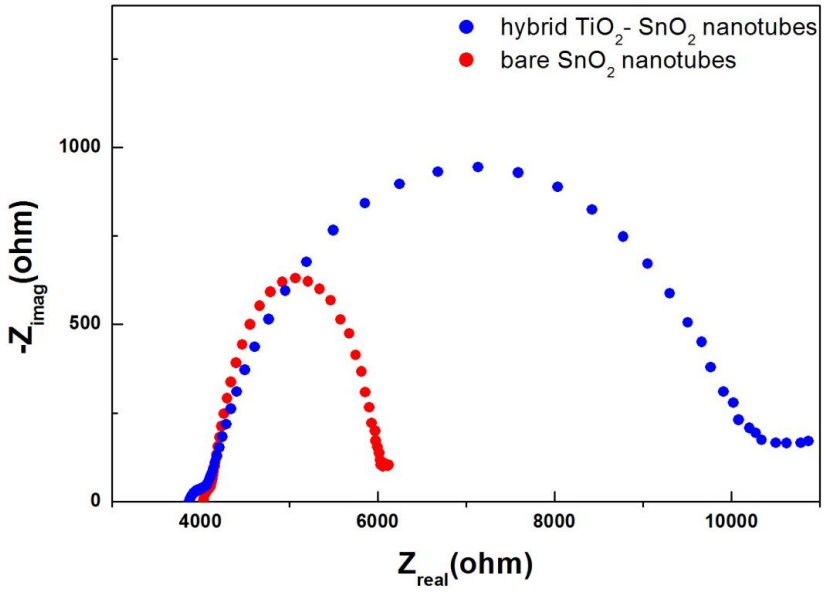

Figure 15. Electrochemical impedance spectroscopy (EIS) for DSCs based on (i) hybrid TiO_2 –SnO_2 nanotubes and (ii) bare SnO_2 nanotube arrays under dark conditions.

Electrons with longer τ_r lead to longer diffusion length (L_n) and can more easily escape the electron recombination. L_n can be derived using the following equations:[72-74]

$$L_n^2 = D_{eff} \times \tau_r \tag{3.8}$$

$$D_{eff} = (R_k/R_w)L^2 k_{eff} \tag{3.9}$$

where R_w, R_k, L, D_{eff}, *and* k_{eff} represent the resistance of electron transport in photoanode, resistance of charge transfer related to recombination, thickness of the photoanode, effective electron diffusion coefficient, and constant of effective rate for recombination, respectively. The values of these parameters were estimated from the central arc of Nyquist and Bode phase plots as described by J.L. Song.[74] R_w is determined from the diameter of the middle semicircle in Nyquist plot shown in **Figure 14a** and R_k is determined from the diameter of the middle

semicircle in Nyquist plot obtained under dark conditions shown in **Figure 15**. k_{eff} is estimated from the maximum peak frequency obtained from the Bode phase plot in **Figure 14b**. The calculated values are tabulated in **Table 5**. These results indicate that the hybrid photoanode is superior to bare SnO_2 nanotube photoanode with significantly larger L_n, D_{eff}, and τ_r but smaller k_{eff}. Besides the expected increase in electron lifetime, a larger effective diffusion coefficient was also observed in case of the hybrid photoanode. The reason for large D_{eff} could be due to the passivation of the low energy SnO_2 surface trap states. These results explain the improved photovoltaic performance of hybrid TiO_2-SnO_2 photoanode as compared to the bare SnO_2 photoanode.

Table 5. Parameters determined by EIS for photoanodes based on (i) bare SnO_2 nanotubes and (ii) TiO_2 -coated SnO_2 nanotubes.

	R_w (Ω)	R_k/R_w	k_{eff} (s^{-1})	τ_r (ms)	D_{eff} (x 10^4 cm^2/s)	L_n (μm)
Bare SnO_2 nanotubes	145 ± 15	12.75 ± 1.45	11.9 ± 1.08	12.89 ± 1.17	1.71 ± 0.33	14.72 ± 0.79
TiO_2-coated SnO_2 nanotubes	165 ± 20	33.45 ± 2.35	8.39 ± 0.06	18.91 ± 0.14	2.89 ± 0.11	23.31 ± 0.12

3.4 CONCLUSIONS

We have developed feasible processes to synthesize long, vertically ordered SnO_2 and hybrid TiO_2-SnO_2 nanotube arrays. All the processes involved in the synthesis are carried out in aqueous solution at low temperatures. We have fabricated DSCs by using the vertically ordered nanotube arrays of both SnO_2 and hybrid TiO_2-SnO_2, and found that coating the SnO_2 nanotubes with a thin layer of TiO_2 significantly improves the DSC performance. The best performing cell is fabricated by using the hybrid TiO_2-SnO_2 anodes, which yields an efficiency of 3.53%. In addition, we have studied the photogenerated electron recombination kinetics of different photoanode materials and observed that the electron recombination lifetime in the anodes of SnO_2 and hybrid TiO_2-SnO_2 nanotubes are significantly higher than in nanoparticle-based anodes and also significantly higher than 1-D nanostructures of ZnO and TiO_2. These results open up the possibility of further improvement of DSCs by using redox mediators with faster kinetics, which would otherwise be hampered by fast recombination of electrons. The use of vertically ordered 1-D nanostructures as anodes in DSCs may also facilitate filling of the pores with solid hole transporting materials, making them promising candidate anodes for solid-state DSCs.[52, 53] We have discussed some aspects of the advantage of vertically ordered nanostructures for solid-state DSCs in more detail in Chapter **5.0** and Chapter **6.0** Furthermore, the vertically ordered SnO_2 nanostructures also have unique advantages for applications in gas sensors[75] and lithium-ion batteries.[76, 77] The application of these SnO_2 nanotubes for LIBs has been explored by us and discussed in Chapter **7.0**

4.0 MULTILAYER ASSEMBLY OF NANOWIRE ARRAYS FOR DYE-SENSITIZED SOLAR CELLS

4.1 INTRODUCTION

As discussed in the last chapter, a key challenge of using vertically aligned 1-D nanostructures in DSCs, compared to mesoporous films, is that they typically have a low internal surface area. This results in insufficient dye adsorption and therefore low light harvesting efficiency.[59, 78-80] As a result, the efficiency of the DSCs based on vertically aligned 1-D nanostructures is significantly lower than that of nanoparticle-based ones. In a recent report,[81] an efficiency of 6.9%, currently the highest one in the literature for DSCs based on 1-D nanostructures, has been achieved using TiO_2 nanotube arrays fabricated on conducting glass substrate (ITO). However, the fabrication process involves complex sputtering and anodization of thick Ti films, which are difficult to scale up both technically and economically. Therefore, to fabricate arrays of long and vertically aligned 1-D nanostructures by an economically viable method remains challenging.

In our previous work, described in Section **2.1**,[45] we have developed a wet chemical process for rapid growth of ZnO nanowire arrays. By using this process, ZnO nanowires of more than 40 μm long may be readily obtained. However, such long wires are typically fused at their root and, as a result, a significant percentage of the surface area gained by increasing the wire

length is lost. Fusion of the wires is largely due to the widening of the wires as they grow long, which occurs in almost all published methods for growing ZnO nanowires in chemical baths. Therefore, to avoid wire fusion, we need to develop a method to grow wires only at the top surface while protecting the lower section of the wires. Here we present an innovative solution to this challenge by synthesizing multilayer assemblies of ZnO nanowire arrays, which possess an internal surface area that is more than five times larger than that of single-layer ZnO nanowire arrays.

A key strategy for preventing the fusion of wires at their root in our process is to grow the wires in multiple stages — wires only grow for about 10 μm in each stage and a self-assembled monolayer (SAM) coating is used to protect the wires grown in previous stages from widening and fusing in the next growth stage. This process is schematically shown in **Figure 16** and is described in the next section.

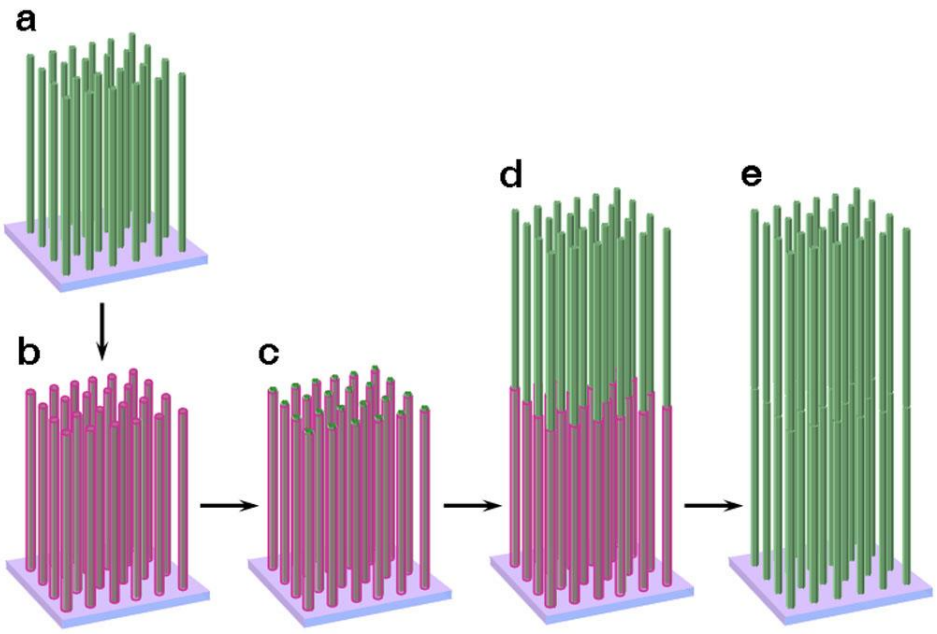

Figure 16. Schematic illustration for growing two-layer assembly of ZnO nanowires

4.2 EXPERIMENTAL METHODS

4.2.1 First Layer Growth and Hydrophobic Coating

The first step was to grow the first layer of wires on ITO by the method described in Section **2.1**. The length of the wires grown in this first stage is around 10 μm. The next step was to coat the nanowire array with a self-assembled monolayer (SAM) coating. This was achieved by dipping the substrate in 0.2 wt% octadecyltrichlorosilane ($CH_3(CH_2)_{17}SiCl_3$, OTS) in hexane for 2 h. The SAM coating rendered the top surface of the nanowires superhydrophobic which was confirmed by water contact angle measurements.

4.2.2 Growth of Multilayer Nanowire Arrays

The substrate was then treated by ultraviolet ozone (UVO) for 3 minutes. After the UVO treatment the substrate was placed into a fresh growth solution resulting in the growth of a second layer of ZnO nanowires. This process of SAM coating and UVO treatment was repeated several times to obtain a four layer nanowire assembly.

4.2.3 DSC Fabrication

After synthesizing the multilayer assembly of nanowire arrays, we fabricated DSCs using them as the photoanode. DSCs were fabricated in a similar way as described in Section **3.2.5**. The fabricated DSCs were then immediately tested using the procedure described earlier. Incident photon-to-current efficiencies (IPCE) were measured with the same potentiostat.

Monochromatic illumination was achieved through M 77250 monochromator (Oriel). Roughness factor (RF) was determined by measuring the adsorbed dye amount. Dye molecules were stripped from the surface the nanowires using 0.01 M NaOH. The amount of dye desorbed was quantified on a USB2000 Spectrometer (Ocean Optics) by measuring the absorbance of the dye, N719. A value of 1.6 nm^2/dye molecule was used to estimate the roughness factor.

4.3 RESULTS AND DISCUSSIONS

4.3.1 Morphological Characterization

Figure 17a shows an SEM image of the first-layer ZnO nanowire array directly grown on ITO. The ZnO nanowires are about 10 μm long and 200 nm wide. It should be noted that in order to reduce the possibility for wires to fuse at their root, the concentration of the precursor $Zn(NO_3)_2$ used in this process was 0.01 M, which was much lower than the typical concentration of 0.025 M reported in the literature and used by us previously.[45, 46] This layer of nanowires was then coated with a SAM of OTS, which rendered the top surface of the nanowire arrays superhydrophobic with a water contact angle of about 165°, as shown in the inset of **Figure 17a**. Prior to the growth of the second-layer wires, the substrate was treated by UVO. By controlling the UVO treatment time, only the SAM coating at the top end of the wires was removed while most of the coating on the sidewall of the wires was left. After this treatment, the water contact angle of the ZnO nanowire arrays was reduced to about 70°. The substrate was then placed into a chemical bath to grow the second-layer ZnO nanowires. **Figure 17b** shows an SEM image of a two-layer assembly of ZnO nanowire arrays, where a boundary between the two layers of wires

was clearly observed. A closer examination of the boundary, seen in **Figure 17b,** indicated that the second-layer wires started their growth from the top end of the first-layer wires and grew along the same orientation as the first-layer wires. The area density of the second-layer wires was slightly smaller than that of the first-layer. This is because some first-layer wires were not long enough to reach the top surface of the array and, thus, the aqueous solution during the second stage of growth. Therefore, they failed to serve as the seed for the growth of the second-layer wires. The second-layer wires were slightly wider than the first-layer wires, because as the wires grew vertically they also grew laterally, although at a much slower rate. The differences in width and density between the wires in different layers led to the visible boundary between the adjacent layers under SEM. Such differences also suggested that the growth of the new-layer wires did not significantly change the morphology of the previous-layer wires and, therefore, widening and fusion of the previous-layer wires at their root was effectively avoided during the growth of the new-layer wires.

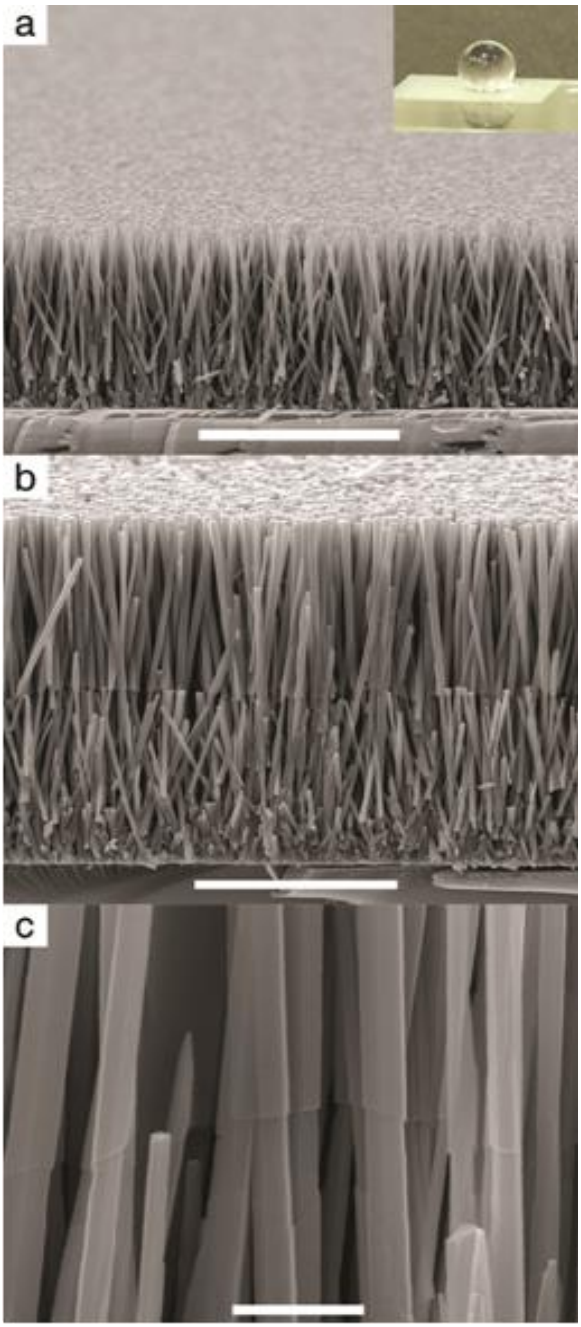

Figure 17. SEM images of one and two layers of ZnO nanowire arrays. a, the first-layer ZnO nanowire array (inset, optical image of a water droplet on the array after it is coated with a SAM coating). Scale bar, 10 μm. b, a two-layer assembly of ZnO nanowire array

The internal surface area of the multilayer assembly of nanowire arrays should keep increasing as more layers are added to the assembly by repeating this process. As a proof of concept, we have made a four-layer assembly using this approach. **Figure 18** shows an SEM image of a four-layer assembly of ZnO nanowire arrays, with each layer of about 10 μm thick.

Figure 18. SEM image of a four-layer assembly of ZnO nanowire arrays. The thickness of each layer is about 10 μm. Scale bar, 10 μm.

4.3.2 Roughness Factor Calculations

In order to quantify the increase in surface area achieved by growing the multi layer assembly, we have performed roughness factor (RF) calculations. RF is defined as the ratio of the actual surface area of the nanowires to the projection area of the substrate. The RF of the four-layer assembly presented in **Figure 18** is plotted as a function of the number of layers by **curve 1** in **Figure 19**. It can be seen that the total RF of the four-layer array assembly is about 510, which is more than five times larger than what one can possibly obtain with a single-layer array. On the basis of **curve 1**, the RFs of the individual layers in the assembly (estimated as the increase in RF resulting from the addition of new layer to the assembly) are plotted as **curve 2** in **Figure 19**.

Curve 2 indicates that RF of each layer varies although the thickness of all layers is the same. When the thickness is fixed, RF of each layer is proportional to the product of the wire diameter and the wire density. For the same reason that the second-layer wires are wider and less dense than the first-layer wires, the width of the wires in each new layer is consistently larger than that of the previous layers, while concurrently the area density becomes smaller. Therefore, the RF for each layer depends on the relative weighing of the two factors: the diameter and the area density of the wires. **Curve 2** indicates that under our experimental conditions, the RF of the third layer was the largest, followed by the second and the first layers, and the RF of the fourth layer was the smallest.

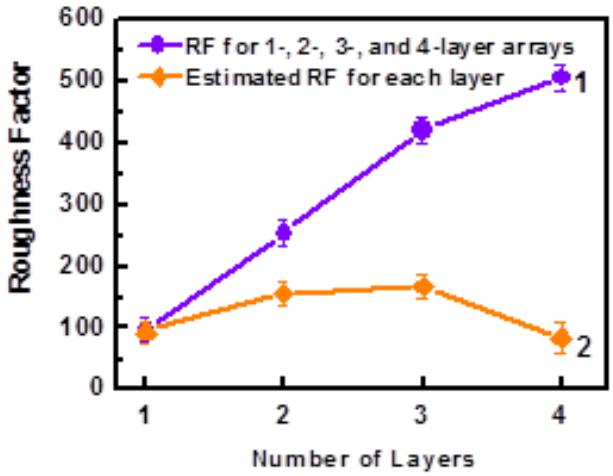

Figure 19. Roughness factor (RF) versus the number of layers for multiple assemblies of ZnO nanowire arrays. Curve 1 is the total RF versus the number of layers in the assembly; curve 2 is the RF for each individual layer

4.3.3 Limitations of Multilayer Growth

An intriguing question is whether there is a limit on the number of layers that one may be able to assemble through this approach. Through experiments, we have found that this assembly approach fails when the distance between the SAM-coated wires is too large to prevent aqueous solution from infiltrating into the underneath wire arrays. Top-view SEM images of the wires in different layers show that as the number of layers increases, the area density of wires decreases and the gap between adjacent wires becomes larger, as seen in **Figure 20**. The aqueous solution will enter the space between the wires if this gap becomes so large that the capillary force generated between the hydrophobic sidewalls of the wires fail to overcome the hydrostatic pressure. Experimentally, we have found that this happens when we try to assemble more than 4-5 layers of wires through this approach. When the aqueous solution is able to infiltrate into the

previously synthesized wire arrays, wires underneath the new layer will be widened and even fused during the growth of the wires of the new layer.

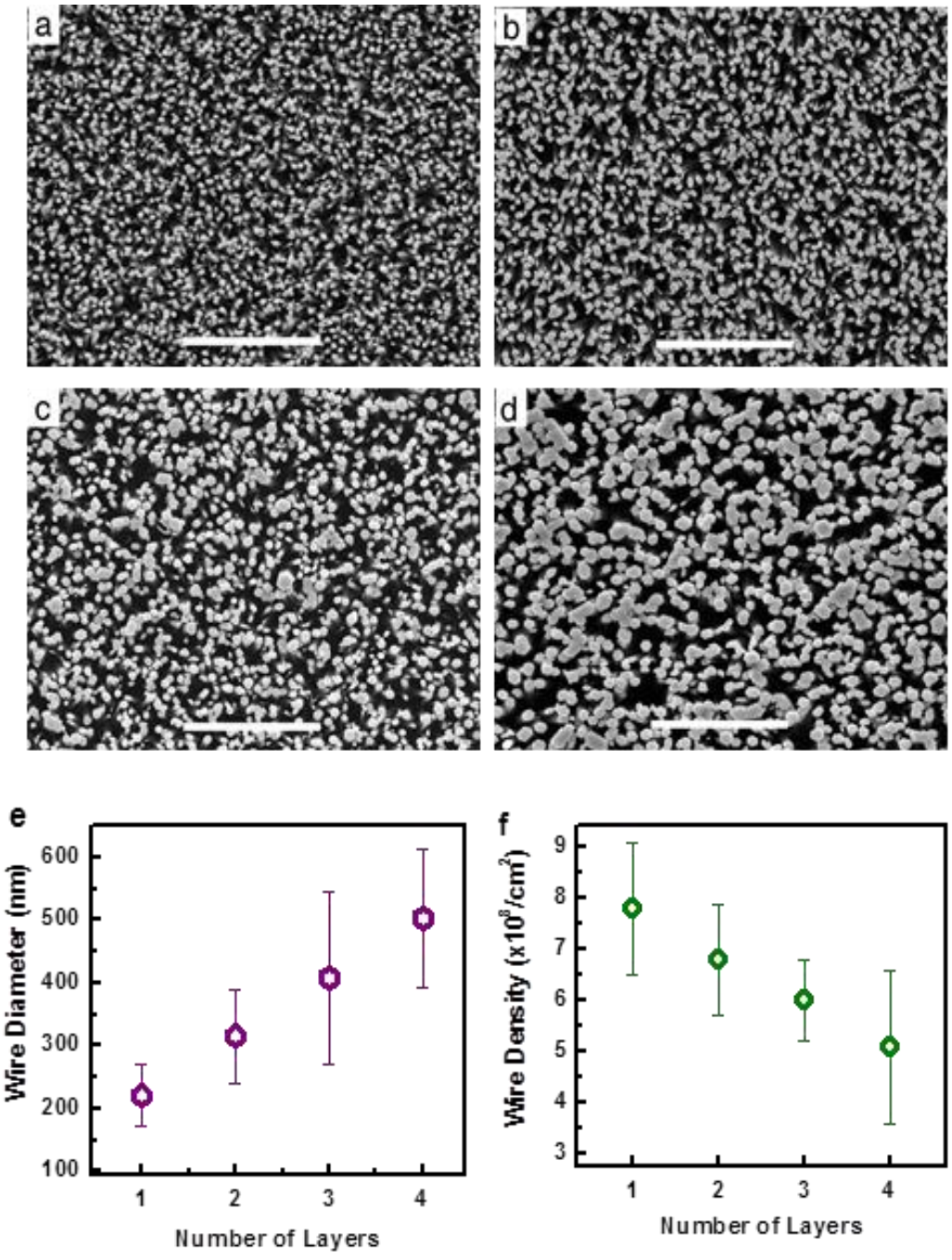

Figure 20. Diameter and density of the wires grown in different layers of the assembly. a), b), c) and d) top-view SEM images of wires grown in the first, second, third, and fourth layers, respectively. Scale bar, 10 μm. e) plot of wire diameter versus the layer. f) plot of wire density versus the layer number.

The multilayer assembly of ZnO nanowire arrays provides an ideal electrode structure for DSCs. However, compared to TiO_2, ZnO has significant disadvantageous material properties when used as an anode material for DSCs, which may result in low open circuit voltage and small fill factor, leading to a low energy conversion efficiency.[59] Therefore, for better characterization of DSCs based on such anode structures and to compare them with DSCs based on TiO_2 nanoparticles, we coated the ZnO nanowires with a layer of about 20-30 nm thick TiO_2 by a solution deposition method[59] before we sensitized the nanowire arrays and made final DSCs. Using this approach, we fabricated a series of DSCs, using assemblies of one, two, three, and four layers of ZnO nanowire arrays, respectively. The thickness of each layer was kept at 10 μm, and the morphology of each layer may be represented by **Figure 18**.

4.3.4 J-V Characterization

The *J-V* characteristics of these DSCs are presented in **Figure 21a**. As expected, the short circuit currents (J_{SC}), largely dependent upon the surface area of the arrays, increase almost linearly with RF as the total thickness of the assembly increases. The energy conversion efficiencies are 2.1, 4.6, 6.2, and 7.0% for the DSCs made using a one-, two-, three-, and four-layer assembly of nanowire arrays, respectively. To our knowledge, the 7.0% efficiency obtained from the four-layer, 40 μm thick assembly is already the highest efficiency reported in the literature for DSCs based on 1-D nanostructures. This efficiency is still lower than what has been reported for DSCs based on sintered nanoparticles, partly because the RF of the current four-layer assembly, which is about 510, is still smaller than the RF of ~780 reported for sintered nanoparticle films.[11]

However, it is believed that the RF of the multilayer assembly can be further increased by increasing the thickness of the array in each layer and, therefore, DSCs based on such multilayer assemblies may outperform the nanoparticle-based DSCs. **Figure 21a** also shows a slight decrease in the V_{OC} and *ff* as the thickness of the multilayer arrays increased, possibly due to the increase in the series resistance of the DSCs. **Figure 21b** shows the incident-photon-to-current conversion efficiency (IPCE) versus wavelength for the DSCs fabricated using different numbers of array layers. As can be seen, increasing the total thickness of the multilayer assembly improves IPCE at all wavelengths varying from 350 to 800 nm. An important feature observed in these IPCE curves is a significant red-shift of the peak IPCE with increasing assembly thickness, indicating that the red-light absorption may be effectively improved by thickening the sensitized film with a vertically ordered structure. The consistently increasing IPCE, with a nearly 80% IPCE for the 40 μm thick assembly, also indicates that the electron collection by the multilayer arrays up to 40 μm thick is reasonably efficient. Relative to the increases in J_{SC} and IPCE upon addition of the second and the third layer wires, growing the fourth layer wires brought a less significant increase in these parameters because the increase in RF (~70) as a result of adding the fourth layer wires was smaller than those (~150) brought by the second and the third layers.

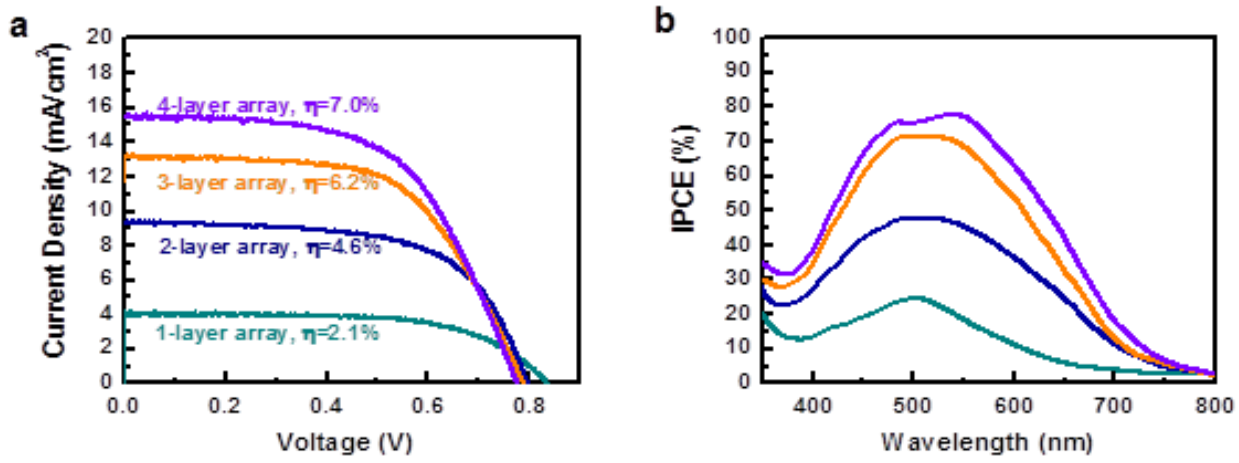

Figure 21. Photovoltaic performance of DSCs fabricated using TiO2-coated multilayer assembly of ZnO nanowire arrays. (a) J-V characteristics; (b) IPCE versus wavelength.

In addition to their application as an anode material for DSCs, ZnO nanowire arrays have been used in ultrasensitive chemical and biological sensors, organic solar cells, light emitting diodes, nanogenerators, and nano-piezotronic devices.[82] It is hoped that the multilayer assemblies of ZnO nanowire arrays and the approach to synthesizing such assemblies may find use in the development of these devices. Furthermore, ZnO nanowire arrays have been used as templates for fabricating TiO_2, Fe_2O_3, SnO_2 and CdSe nanotube arrays.[59, 83, 84] There is no apparent technical barrier to the use of these processes in fabricating multilayer TiO_2, Fe_2O_3, and CdSe nanotube arrays by employing the multilayer ZnO nanowire arrays as template. Such vertically aligned structural materials with a high internal surface area may find applications for catalysis and as electrodes in batteries and fuel cells.[85, 86]

4.4 CONCLUSIONS

In summary, we have developed a convenient approach to synthesizing multilayer assemblies of high surface-area nanowire arrays. The approach involves alternate cycles of nanowire growth and self-assembled monolayer coating processes. As a demonstration, assemblies of one to four layers of ZnO nanowire arrays with a total thickness of up to 40 μm have been synthesized. The internal surface area of the 4-layer assembly is more than five times larger than what one can possibly obtain with a single layer array. Such multilayer assemblies have been used to fabricate DSCs which yield power conversion efficiencies of up to 7%.[66] The potential of such an approach to synthesizing multilayers of vertically aligned nanowire arrays has not been fully explored, and it is believed that by optimizing process parameters and by increasing the thickness of each layer, the internal surface area of such assemblies can be further increased and, therefore, DSCs with better performances may be fabricated.

5.0 SOLID-STATE DYE-SENSITIZED SOLAR CELLS BASED ON ZINC OXIDE NANOWIRE ARRAYS

As discussed earlier in Section **1.1.3**, the use of liquid electrolyte limits device stability and, hence, many attempts have been made to overcome these limitations by replacing the liquid electrolyte with a solid or a quasi-solid hole- transport material HTM.[13] We also discussed, that, compared to anodes based on sintered nanoparticles, much thicker anodes based on aligned 1-D nanostructures may be used in solid-state DSCs, and higher efficiencies may be obtained. In the next section we report the work done by us on solid-state DSC using ordered ZnO nanowire array as the photoanode. **Figure 22** shows a schematic illustration of ZnO nanowire-based solid-state DSC.

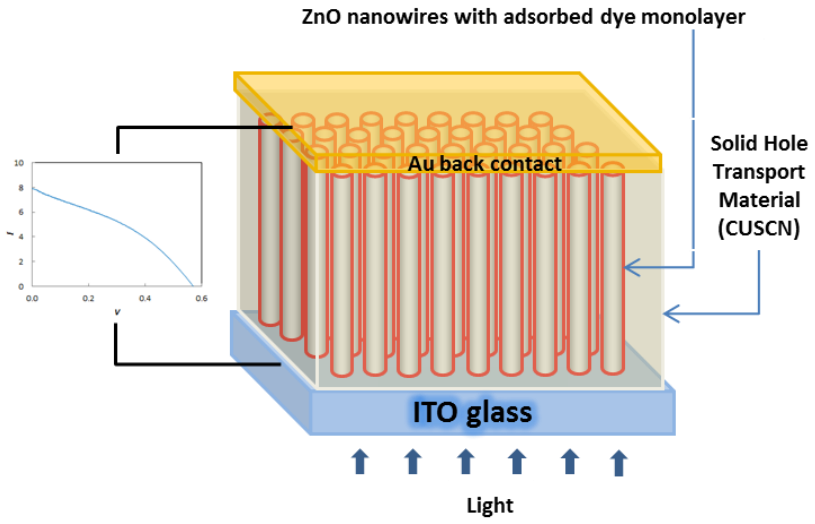

Figure 22. Schematic illustration of ZnO nanowire based solid-state DSC

5.1 INTRODUCTION

The role of an electrolyte in a DSC is to transfer the electrons to the photo-oxidized dye molecules and then to transport the positive charge to the counter electrode. Inorganic p-type semiconductors can be effectively used as solid hole-transport materials as a substitute for the liquid electrolyte for DSCs. Copper-based materials, CuI and CuSCN, have been extensively investigated.[87, 88] They exhibit high conductivity, exceeding 10^{-2} S/cm.[89] Although cells with CuI have been reported to show better performance, they are not very stable due to the stoichiometric excess of iodine molecules adsorbed at the CuI interface.[90] DSCs incorporating CuSCN as the HTM show improved stability.[13] CuSCN has a hexagonal lattice in which (001) planes of Cu^{I} atoms are separated by layers of SCN^{-} ions aligned parallel to the *c*-axis**.**[91] The stabilization of the oxidized state leads to easy donation of the electrons to the Ru^{II} of the photo-oxidized dye N719.

Among the 1-D nanostructures, vertically aligned ZnO nanowires have attracted considerable interest because of their unique material properties as well as the convenience and robustness of the synthesis processes for growing ZnO nanowires on a variety of substrates. Numerous novel applications in optics, optoelectronics, energy conversion, and photovoltaics have been demonstrated by using the aligned ZnO nanowire arrays.[92, 93] In particular, single crystalline ZnO nanowires enable fast electron transport and have been used for nanowire-based DSCs.[46] ZnO nanowires have also been used for fabrication of solid-state DSCs, but the nanowires used were very short (actually in the form of nanorods) and hence the reported efficiency of the solid-state DSCs was very low (≈0.1%).[94] This could be mainly due to the insufficient area for the dye adsorption offered by the short ZnO nanorods. Potentially, the performance of solid-state DSCs could be significantly improved by using long ZnO nanowires,

but such effort has not been reported, primarily due to the difficulty in the synthesis of long vertically aligned ZnO nanowires and integration of such nanowires into solid-state DSCs.

In the present work, solid-state DSCs are fabricated with 11-12 μm long, vertically aligned ZnO nanowires as the photoelectrode, CuSCN as the solid HTM, and N719 as the light absorbing dye. **Figure 23** shows the energy-band diagram of the synthesized DSC.[95, 96] The conduction band of ZnO and valence band of CuSCN are such that they enable electron flow across the ZnO/N719 dye/CuSCN interface as indicated by the arrows. Efficient filling of the nanowire arrays with CuSCN is demonstrated. The resulting solid-state DSC, based on ZnO nanowires completely embedded in CuSCN, yields a remarkably higher photocurrent density (J_{SC}= 8 mA/cm^2) compared to previously reported data for similar solid-state DSCs based on either 1-D nanostructures (J_{SC}= 0.34 mA/cm^2)[94] or nanoporous nanocrystalline ZnO (J_{SC}= 4.5 mA/cm^2).[96] A power conversion efficiency of 1.7% under an irradiation of AM 1.5G simulated sunlight is obtained, which is significantly higher than the previously reported efficiency (about 0.1%) [94] of solid-state DSCs based on ZnO nanorods. Furthermore, the efficiency obtained for our DSCs was comparable to the TiO_2 nanoparticle-based solid-state DSCs. The efficiencies reported for solid-state DSCs using TiO_2 nanoparticles as the photoanode and CuSCN as the HTM are in the order of 1.5-2%. [16, 17]

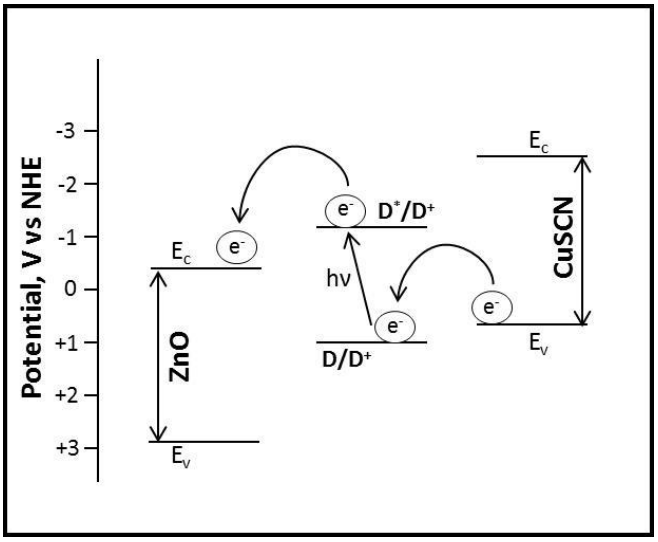

Figure 23. Energy-band diagram of the ZnO/N719 dye/ CuSCN interface

5.2 EXPERIMENTAL METHODS

5.2.1 Growth of ZnO nanowire arrays

Ordered ZnO nanowires were grown on indium-doped tin oxide (ITO)-coated glass substrates by method described in Section **2.1.**

5.2.2 CuSCN deposition

To prepare the solution for HTM deposition, 0.1 g CuSCN was dissolved in 5 ml propylsulphide and the solution was stirred overnight and then allowed to settle for 6 hr. The supernatant was separated from the undissolved CuSCN and aliquots of 2 ml were removed from this supernatant. These aliquots were further diluted with 250 µL of propylsulphide before use.

The ITO glass substrate, with dye-coated ZnO nanowires, was then placed on a hot plate at 75°C. Small droplets, each drop size being 2 µL, were then dropped on the substrate. After each drop, the solution was spread evenly on the surface using air flow and the solvent was allowed to evaporate completely. This procedure was repeated 25-30 times resulting in ZnO nanowires embedded with CuSCN and a thin film of CuSCN on the top of the nanowires.

5.2.3 Fabrication and Characterization of DSCs

A major advantage of using solid HTMs is that it does not necessitate the use of Pt counter-electrode for catalyzing the electrolytic reaction. Thus, instead of using a Pt counter-electrode one can use simply to metallic conducting electrode. In our work, we have deposited a 100 nm thick layer of gold by e-beam evaporation after CuSCN deposition. This gold layer acts a back contact. 2 cm long Cu strips were attached to both the front and back contacts to enable electrical connections for cell characterizations. *J-V* curves were obtained by method described in Section **3.2.5**. Incident photon-to-current efficiencies (IPCE) were measured with the same potentiostat. Monochromatic illumination was achieved through M 77250 monochromator (Oriel). Light harvesting efficiency was quantified by measuring the absorbance of the dye using USB2000 Spectrometer (Ocean Optics).

5.3 RESULTS AND DISCUSSIONS

5.3.1 Morphological Characterization

Ordered ZnO nanowires were grown on indium-doped tin oxide (ITO)-coated glass substrates by a liquid-phase deposition (LPD) process previously developed by our group.[45] With coupled use of ammonium hydroxide and polyethyleneimine, formation of ZnO in the bulk solution and hence depletion of reactants was successfully prevented, and wires of up to 12 μm in length were grown without replenishing the growth solution. **Figure 24** shows representative cross-section and top-view SEM images of a ZnO nanowire array. The wires are 12 μm long, and 150-200 nm in diameter. It is worth noting that the surface of the nanowire array is clean and free of particles and the root of the wires remains separated from each other—both are important factors that affect the performance of the DSCs fabricated based on such arrays.

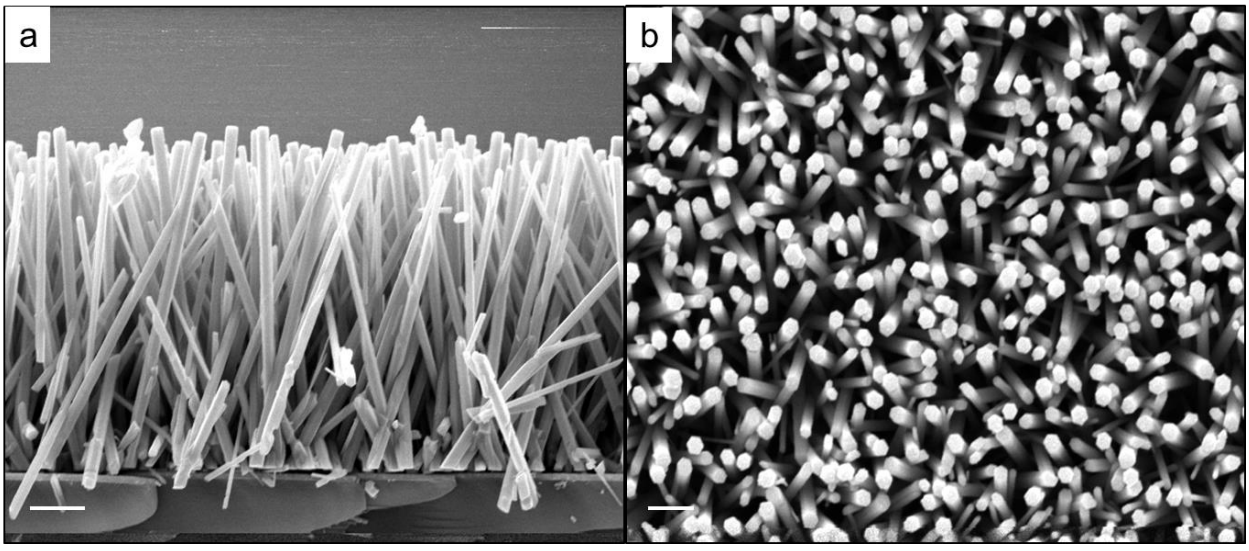

Figure 24. SEM images of an ZnO nanowire array. The wires are 11-12 μm long, and 150-300 nm in diameter. (a) Cross-section image. Scale bar, 2 μm. (b) Top-view image. Scale bar, 1 μm.

After coating the ZnO nanowires with the dye, the array was filled with a solid-state electrolyte, CuSCN, by a solvent based technique. Various methods have been reported for deposition of CuSCN. Electrochemical deposition[95] and solvent-based techniques have been the most commonly used.[88] In our work, CuSCN was deposited from a solution of n-propylsulphide. During the CuSCN deposition stage, it was important to avoid formation of voids which might behave as 'dead-zones' and lead to loss in efficiency. **Figure 25** shows cross-section and top-view SEM images of ZnO nanowires completely embedded in CuSCN with an about 1 µm thick CuSCN layer on top. This layer of solid electrolyte is essential to avoid short-circuiting of the cell. However, too thick a layer of CuSCN on top would lead to increase in series resistance of the cell, because of the relatively low electrical conductivity of CuSCN, leading to poor device performance. Hence, it was critical to ensure that the CuSCN layer formed at the top was uniform, yet thin for optimum device performance.

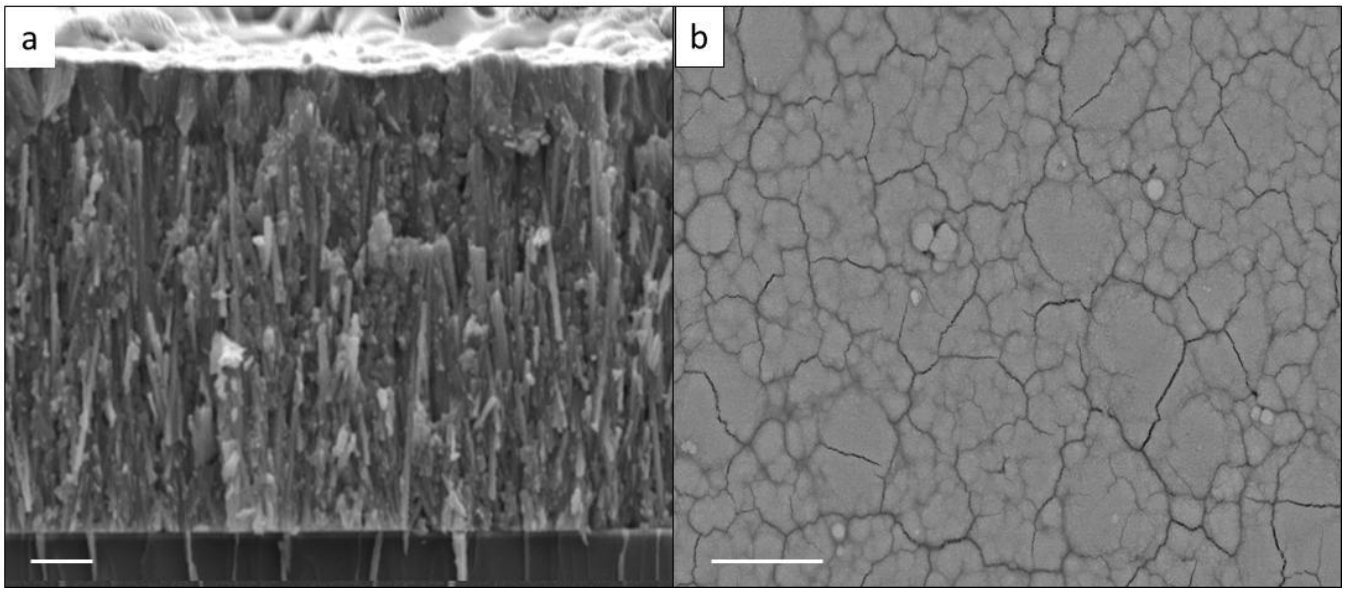

Figure 25. SEM images of ZnO nanowire array after CuSCN deposition. (a) Cross-section image. Scale bar, 2 µm. (b) Top-view image. Scale bar, 10 µm.

Figure 26a and **Figure 26b** represent the energy-dispersive X-ray (EDX) spectra taken at the top surface and the base of the nanowire array, respectively, after deposition of CuSCN. As a comparison, **Figure 26c** shows the EDX spectrum taken before the deposition of CuSCN. **Figure 26a** shows strong peaks corresponding to Cu, S, and C on the top surface of the nanowire array without detectable peaks for Zn and O, which indicates that the surface is completely covered by CuSCN. **Figure 26b** shows peaks from both CuSCN and ZnO at the very bottom of the array, which confirms the thorough filling of the nanowire array with the solid electrolyte.

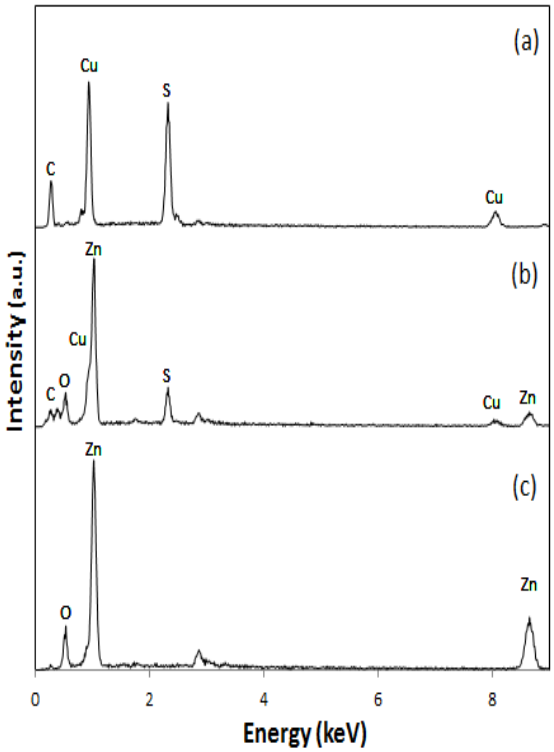

Figure 26. EDX analysis of the ZnO nanowire array before and after CuSCN deposition. (a) The top surface after CuSCN deposition. (b) Cross-section at the base of the array after CuSCN deposition. (c) Cross-section at the base of the array before CuSCN deposition.

5.3.2 J-V and Quantum Efficiency Measurements

After evaporating a gold thin film on the top of the CuSCN layer as a back contact, the cells were tested under AM 1.5G simulated sunlight. A typical *J-V* curve for the fabricated solid-state DSC is shown in **Figure 27**. The cell delivered a short-circuit current density (J_{SC}) of 8 mA/cm^2 and an open-circuit voltage (V_{OC}) of 0.57 V. Peak efficiency of 1.7% was obtained and the corresponding fill factor was 0.37.

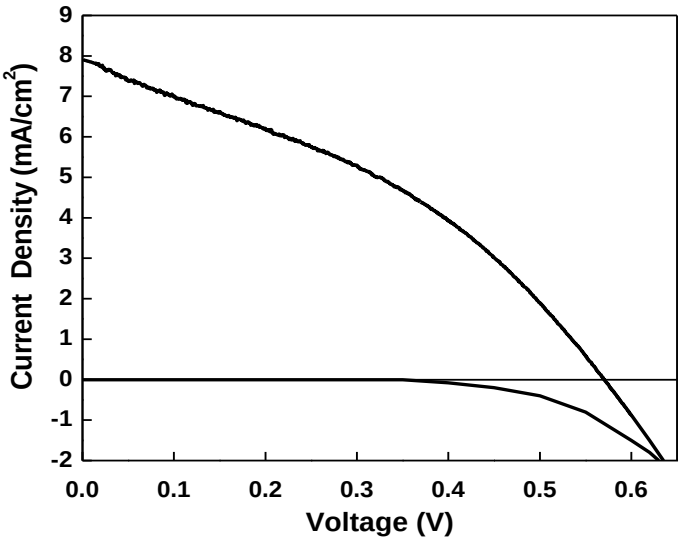

Figure 27. J-V characteristic of the solid-state DSC under AM 1.5G simulated sunlight (upper line) and under dark conditions (lower line).

The obtained J_{SC} of 8 mA/cm^2 is significantly higher than J_{SC} (0.34 mA/cm^2)[94] of previously reported nanowire-based solid-state DSCs. The improvement in photocurrent could be attributed mainly to the increased light absorption due to the increased dye loading enabled by using a nanowire array with a higher roughness factor. The vertical channels formed by the

ordered nanowire array significantly facilitated filling of the cell with the solid HTM and thus a much thicker sensitized film could be used in the cell, which allowed much higher loading of the dye.

The significantly improved J_{SC} leads to a much higher power conversion efficiency of 1.7%. This efficiency is comparable to the best reported TiO_2 nanoparticle-based solid-state DSCs using CuSCN as the HTM (1.5-2%).[16, 17] Although our cell yields significantly higher J_{SC}, the open-circuit voltage (V_{OC}) and the fill factor are lower than TiO_2 nanoparticle-based solid-state DSCs. This is mainly due to the inherent material characteristics of ZnO, which is known to yield lower fill factors and V_{OC} compared to TiO_2 when used as the photoanode in conventional liquid electrolyte DSCs.[45, 46]

The photo spectral response of the ZnO nanowire-based solid-state DSC was also studied to determine the charge collection efficiency of the anode. **Figure 28** shows the incident-photon-to-current conversion efficiency (IPCE) and the light harvesting efficiency (LHE) curves. IPCE is the ratio of number of electrons collected in the external circuit to the number of photons incident on the surface. For DSCs, IPCE can be expressed using the following equation:

$$\text{IPCE}(\lambda) = \text{LHE}(\lambda) \times \text{IQE}, \quad (1)$$

where λ is the wavelength, and IQE is the internal quantum efficiency, an indicator of electron injection and charge collection efficiency. As seen in **Figure 28**, the IPCE curve is close to the LHE curve, indicating very high IQE. The value of IQE at peak absorption wavelength (530 nm) is about 0.9. The high IQE indicates efficient electron injection and collection at the anode of solid-state DSCs enabled by the aligned ZnO nanowires.

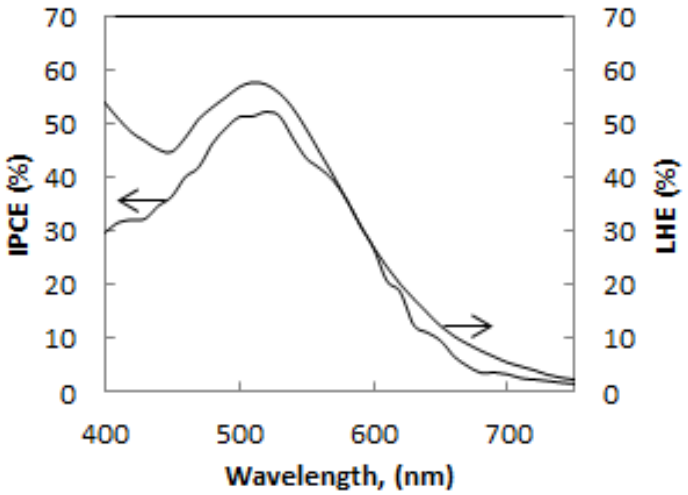

Figure 28. IPCE and light harvesting efficiency (LHE) curves for the solid-state DSC.

Although the efficiency and the fill factor are too low to be considered for practical applications, the solid-state DSC fabricated in this work may be improved through several approaches. First, the high electron collection efficiency at the anode indicates that there is still much space for increasing the dye loading by further increasing the length of the nanowires while maintaining high electron collection efficiency. This could result in efficiencies greater than the TiO_2 nanoparticle-based solid-state DSCs, whose thickness is limited by the difficulty in pore filling by HTM.[17] An ordered nanowire array structure provides vertical channels facilitating filling of the cell with solid HTM, making possible the use of thicker nanowire films. Longer nanowires could be obtained by allowing the nanowires to grow for longer duration, but this is typically accompanied by the lateral growth of nanowires, which leads to fusion of nanowires at the bottom and eliminates the surface area gained by increasing the wire length. Innovative approaches are currently being developed by our group to avoid fusion of nanowires while increasing their length, which may improve the efficiency of solid-state DSCs. Second, compared to TiO_2, ZnO has significant disadvantageous material properties when used as an

anode material for DSCs, which result in low open circuit voltage and small fill factor, leading to low energy conversion efficiency. Therefore, converting the ZnO nanowire to TiO_2 nanotube by a method previously published by our group[59] may improve the performance of the solid-state DSCs. Such effort is currently underway. Third, effective filling of the nanowire arrays with CuSCN remains challenging, and will become more challenging when longer nanowires are used as the anode. In this work, CuSCN is deposited by repeatedly dropping a solution of CuSCN in n-propylsulphide onto the film. This method may form voids between the nanowires which might behave as 'dead-zones' and lead to loss in efficiency. Alternate deposition techniques, such as electrochemical deposition, may improve infiltration of the solid HTM into nanowire arrays and lead to improved cell performance. Fourth, alternative HTM, such as spiro-OMeTAD [2,2',7,7'-tetrakis-(*N*,*N*-di-*p*-methoxyphenylamine)9,9'-spirobifluorene],[18] could lead to higher fill factors, and alternative dyes with a higher molar extinction coefficient than N719 may result in higher photocurrent. These approaches, which can be used either individually or in combination, may improve the performance of the solid-state DSCs, making them viable for practical applications.

5.4 CONCLUSIONS

We have fabricated solid-state DSCs using a vertically aligned ZnO nanowire array as the anode and CuSCN as the solid HTM. The fabricated cell yielded high current densities and promising efficiencies when compared to similar solid-state DSCs. The primary reason for this result is the increased surface area for dye adsorption offered by the long, vertically oriented ZnO nanowire array. The anode made of such an array allows for effective filling of the

sensitized film with the solid HTM and retains high electron collection efficiency at a film thickness as large as 12 μm. This encouraged us to explore the possibility of using a thicker photoanode for solid-state DSCs, with the hope of increasing light harvesting efficiency and consequently, the device efficiency. In the next chapter, we are going to talk about solid-state DSCs using the multilayer nanowire arrays as the photoanode and spiro-OMeTAD as the HTM.

6.0 HIGH-EFFICIENCY SOLID-STATE DYE-SENSITIZED SOLAR CELLS

In the previous chapter we talked about how we have fabricated solid-state DSCs with a single layer nanowire array as the photoanode and achieved performance comparable to similar liquid-state DSCs. We demonstrated very high electron injection and collection efficiency using ZnO nanowire array as the photoanode opening up the possibility of using thicker photoanodes. Despite a lot of effort, synthesizing vertically ordered nanostructures with a sufficiently high internal surface area and incorporating them in solid-state DSCs has proven to be challenging till date.[79, 80] As a result solid-state DSCs based on such photoanodes have suffered from low dye loading and hence in low efficiencies.[97, 98]

Herein, we talk about the fabrication of solid-state DSCs based on multilayer array of nanowire arrays. The procedure for growing these vertically ordered multilayer arrays has been described earlier in Chapter **4.0** [66] Along with providing a high surface area for dye loading, the multilayer arrays also provide vertical channels for electrolyte filling, opening up opportunities for fabricating high efficiency solid-state DSCs. We have been successfully able to fabricate solid-state DSCs using the multilayer nanowire arrays as photoanode and spiro-OMeTAD as the solid hole transport material (HTM). By using an effective HTM filling process, we were able to use a 50 μm thick photoanode, resulting in solid-state DSCs with a power conversion efficiency of 5.65%. Instead of using CuSCN, we have used spiro-OMeTAD (2,20,7,70-tetrakis-(N,N-di-p-methoxyphenylamine)9,90-spirobifluorene) for these experiments.

Compared to the previously used, CuSCN, and other such inorganic p-type semiconductors, organic hole transport materials possess the advantage of having plentiful sources, easy film formation and potentially being low cost. Also, spiro-OMeTAD can be effectively doped by chemical or electrochemical oxidation to achieve the desired conductivity. The high solubility and respectable charge carrier mobility further make Spiro-OMeTAD an attractive option.[15, 99] Solid-state DSCs with Spiro-OMeTAD have achieved efficiencies of over 5%.[100] **Figure 29** shows the chemical structure of Spiro-OMeTAD.[18]

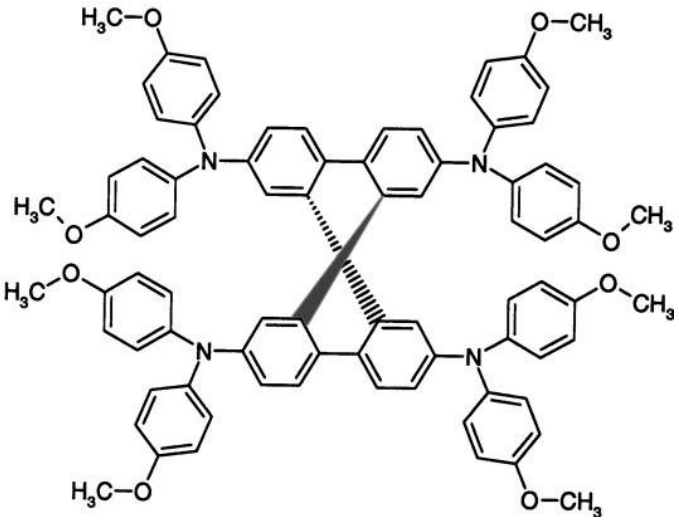

Figure 29. Molecular Structure of spiro-OMeTad

6.1 RESULTS AND DISCUSSIONS

6.1.1 Morphology Characterization

Figure 30 shows an SEM image of a four-layer ZnO nanowire array. This multi leyer nanowire assembly was synthesized in the same manner as discussed in Chapter **4.0** The entire array is about 50 μm thick, and the 4 individual layers are 11, 15, 14 and 10 μm thick, respectively, from bottom to top. The four-layer ZnO nanowire array possesses a roughness factor of about 510. To achieve better DSC photovoltaic performance, the ZnO nanowires were coated with a layer of TiO_2 by the method described earlier in Section **3.2.3**.

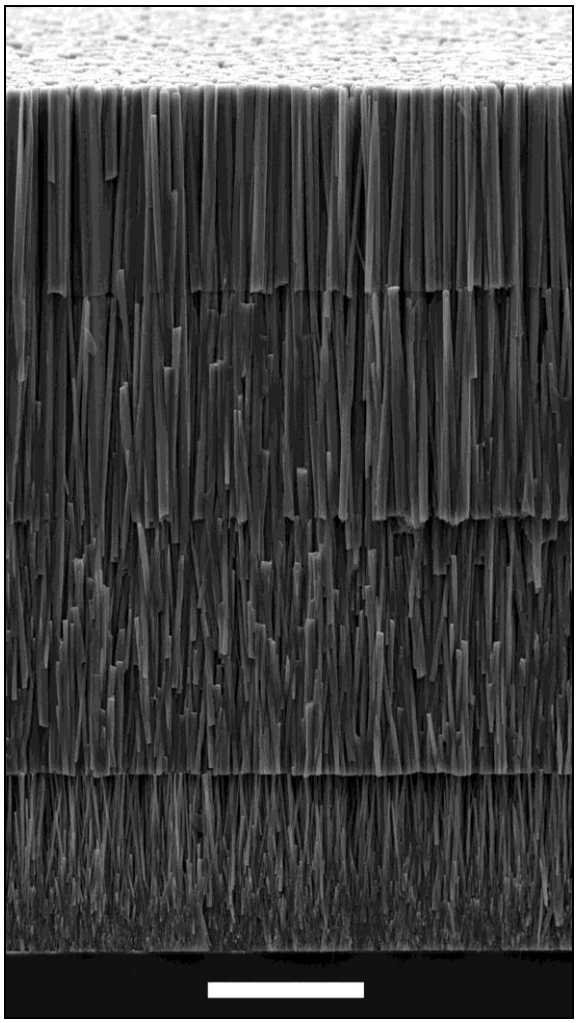

Figure 30. SEM image of a four layer assembly of ZnO nanowire arrays. Scale Bar, 10 μm.

Figure 31 shows a scanning transmission electron microscopy (STEM) elemental mapping image of a TiO_2-coated ZnO nanowire and a line-scan energy dispersive X-Ray Spectrum across the width of the nanowire. The ZnO nanowire is uniformly coated with a 20-30 nm thick layer of TiO_2.

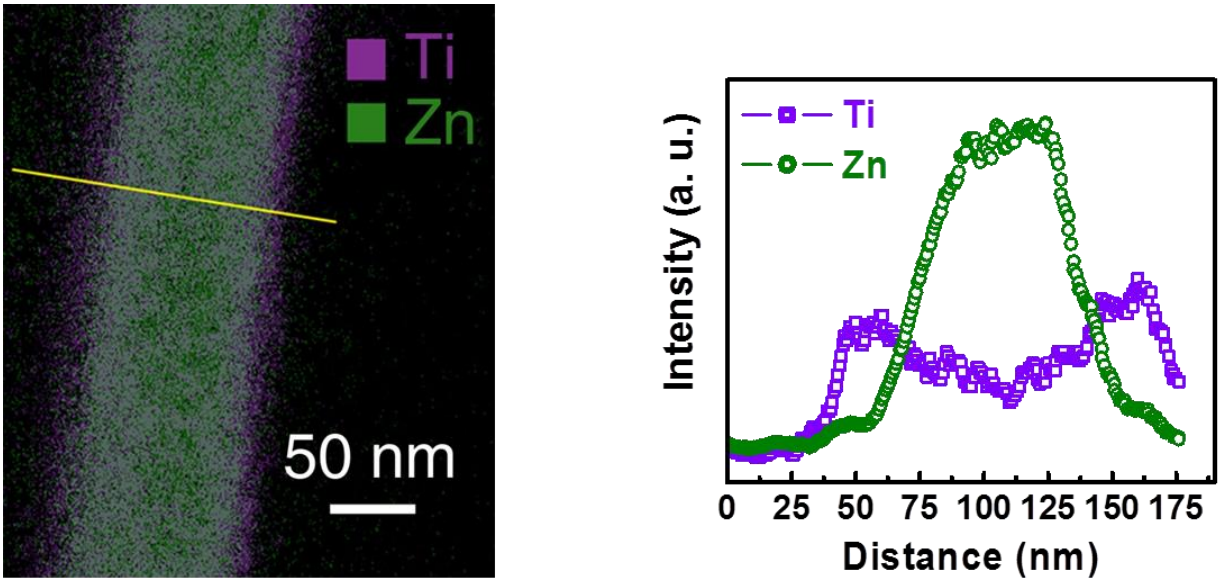

Figure 31. TEM analysis of TiO_2-coated ZnO nanowires. (a) STEM elemental mapping image. (b) Line-scan EDX profile obtained along the dotted line in (a).

Although the four-layer nanowire array provides straight channels for electrolyte filling, the effective filling of solid HTM in such high aspect ratio nanostructures is still challenging. First, we tried a literature reported process for filling the nanostructure with the solid HTM.[101-103] The method involves using a single application of 200 mg/ml of spiro-OMeTAD solution. This was followed by spinning off the excess solution and drying the solvent off. The excess solution on the top of the film acts a reservoir during the filling process. As the solvent evaporates, the concentration of spiro-OMeTAD in the reservoir increases and more spiro-

OMeTAD diffuses into the film. **Figure 32** shows a representative SEM image of the nanowire array filled with spiro-OMeTAD by this single-stage process. It was observed that spiro-OMeTAD has infiltrated down to the bottom of the nanowire array, almost 50 μm below the top surface. However, a large number of voids were observed, especially in the bottom three layers, indicating that this HTM filling process is ineffective for high aspect ratio nanostructures.

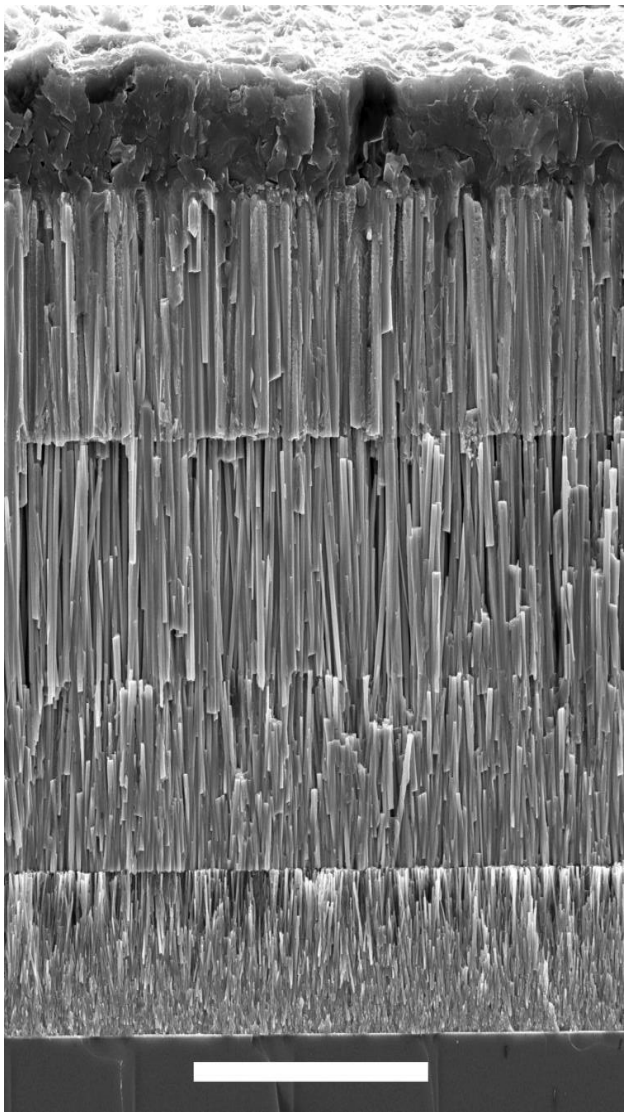

Figure 32. SEM image of a four layer TiO_2-coated ZnO nanowire array filled with spiro-OMeTAD by the single-step process. Scale bar, 20 μm.

We believe the main reason for the inefficient filling is the increase in the viscosity of the HTM solution associated with the evaporation of the solvent. This increase in viscosity leads to a lower rate of diffusion rate, inhibiting effective infiltration. As a consequence, the solution on the top of the nanowires forms a solid overlayer during the subsequent drying before enough HTM diffuses into the nanowire film. The formation of this overlayer makes it extremely difficult for the HTM to effectively fill the entire nanowire film even with multiple applications of the HTM solution. The SEM image in **Figure 32** is a representative result of such multiple applications, resulting in an approximately 7 μm thick overlayer.

To overcome the limitations of this process and to ensure effective filling of HTM, we have developed a multi-step HTM filling procedure. Instead of applying an excess volume of the HTM solution in one step, we apply the solution in multiple steps. The concentration of the solution used is the same as before i.e. 200 mg/ml. In each step, we apply only a small volume, about one-half of the total space occupied by the nanowire array. By applying the solution in a volume smaller than the pore volume of the array in each step, the overlayer formation is avoided to a large extent. **Figure 33** shows a representative SEM image of a four-layer TiO_2-coated ZnO nanowire array with spiro-OMeTAD by the multi-step process. It is evident that the filling of spiro-OMeTAD is significantly improved and the thickness of the overlayer is only about 1 μm. AS discussed earlier in Chapter **6.0** this overlayer is essential to avoid short-circuiting while depositing the gold back contact. After filling the multi layer nanowires with spiro-OMeTAD, DSCs were fabricated and characterized in the same way as described in Section **5.2.3**.

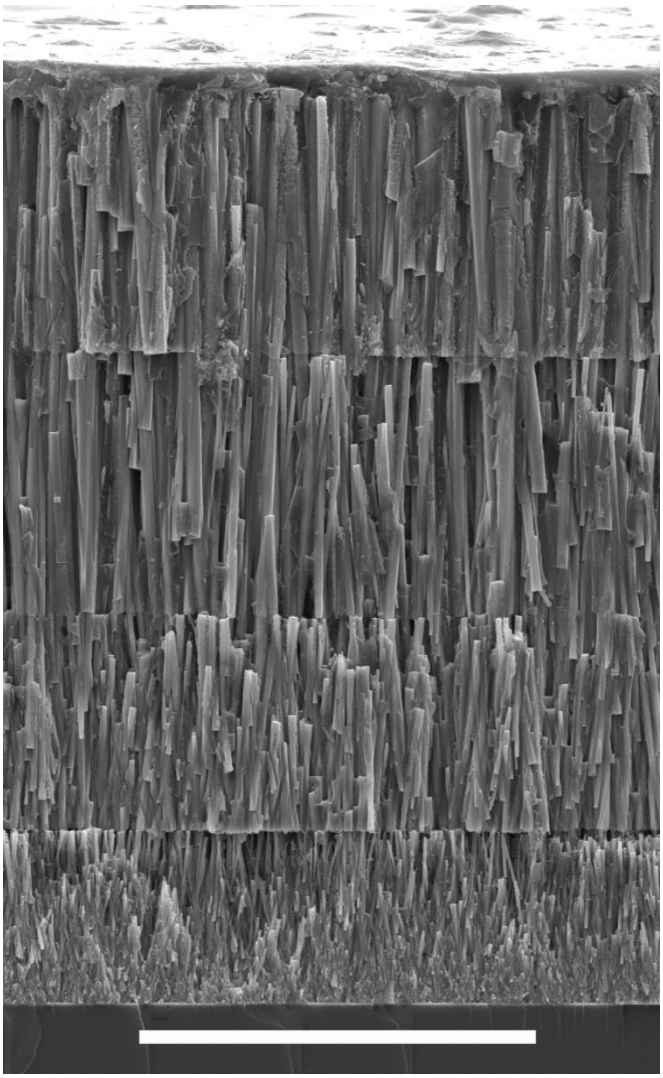

Figure 33. SEM image of a four layer TiO_2-coated ZnO nanowire array filled with spiro-OMeTAD by the multistep process. Scale bar, 20 μm.

6.1.2 Photovoltaic Performance

To illustrate the effectiveness of our multi-step process for filling HTM, we have fabricated two groups of solid-state DSCs. The first group of solid-state DSCs is filled with spiro-OMeTAD by the single step process and the second group of cells is filled with spiro-OMeTAD by our multistep method. The short circuit current density (J_{SC}), open-circuit voltage (V_{OC}), fill factor (*ff*), and power conversion efficiency (η) of the two groups of cells are tabulated in **Table 6** and **Table 7**. **Figure 34** shows the *J-V* characteristics of two representative cells. The plot of incident photon-to-current conversion efficiency (*IPCE*) versus wavelength is shown in the inset. J_{SC} of both groups of cells are about 12 mA/cm^2 which is greater than the value reported for the nanoparticle based solid-state DSCs[104-106] and also significantly higher than the J_{SC} for our solid-state DSC using a single layer of ZnO nanowire array.[107] The main reason for this is that the use of a thicker photoanode leads to significantly higher dye loading resulting in better light absorption and hence higher photocurrents.

Table 6. Photovoltaic performance date for solid-state DSCs using single-step HTM filling process

Cell no.	J_{SC} (mA/cm^2)	V_{OC} (V)	*ff*	η (%)
1	11.9	0.714	0.488	4.15
2	12.0	0.730	0.517	4.52
3	11.9	0.673	0.498	3.99
4	11.7	0.691	0.514	4.16
5	11.3	0.695	0.521	4.09
6	11.6	0.673	0.522	4.07
7	12.1	0.718	0.511	4.42
8	11.5	0.719	0.520	4.30
Average	**11.75**	**0.702**	**0.511**	**4.21**

Table 7. Photovoltaic performance data for solid-state DSCs using multi-step HTM filling process

Cell no.	J_{SC} (mA/cm^2)	V_{OC} (V)	*ff*	η (%)
9	12.2	0.788	0.568	5.46
10	12.2	0.792	0.589	5.68
11	12.4	0.798	0.594	5.86
12	12.3	0.790	0.591	5.74
13	12.0	0.786	0.608	5.73
14	12.5	0.786	0.571	5.61
15	11.9	0.778	0.591	5.48
Average	**12.2**	**0.788**	**0.587**	**5.65**

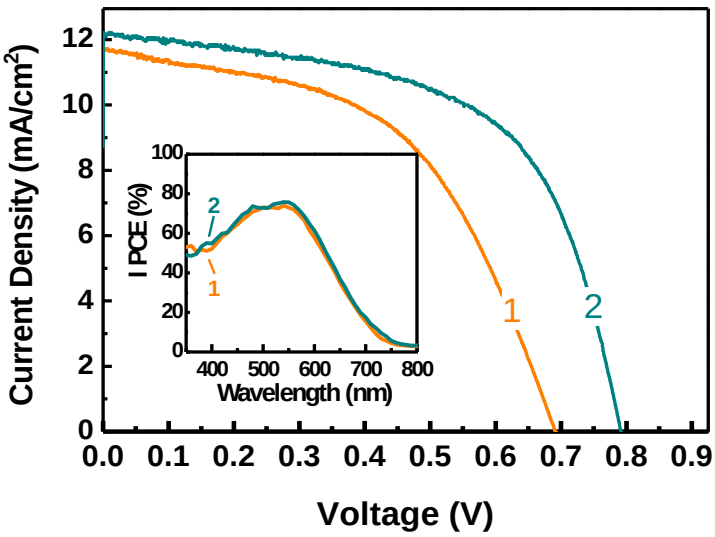

Figure 34. J-V Characteristics of two representative solid-state DSCs fabricated by filling the four-layer TiO_2-coated ZnO nanowire arrays single-step (curve 1) and multistep (curve 2) processes. Inset, IPCE versus wavelength plot.

Comparison of the device characteristics for the two groups of solid-state DSCs reveals that the multi-step filling process results in significantly improved device performance. Compared to the single-step method, J_{SC}, V_{OC}, and *ff* have increased on average from 11.75 to 12.2 mA/cm^2, 0.702 to 0.788 V, and 0.511 to 0.587, respectively. These improvements lead to significant improvement in the overall power conversion efficiency from 4.21% to 5.65%.

6.1.3 Electrochemical Impedance Spectroscopy

To better understand the improved performance of solid-state DSCs fabricated using multi-step process, we have performed electrochemical impedance spectroscopy (EIS) on both

groups of solar cells. **Figure 35** shows EIS spectra of two representative solid-state DSCs (under illumination of AM 1.5G simulated sunlight) for the two groups of solar cells. In the frequency range of 0.1-1 x 10^4 s^{-1}, the Nyquist plots for both solar cells are in the form of a large semicircle. The semicircle in this frequency range on the Nyquist plots is associated with the charge transfer across the photoanode/electrolyte interface and the size of the semicircle represents the recombination resistance between electrons in the photoanode and the holes in the HTM.[108-111] The semicircle representing the cell made by multistep filling process is larger than that of the single-step filling process as can be seen from the Nyquist plots. This represents and increased recombination resistance in the case of the DSC fabricated using the multi-step process. The increased recombination resistance leads to a longer electron lifetime, which is manifested by the left-shift of the characteristic frequency in the Bode phase plots. In addition, the reduced overlayer thickness on top of the array, as a result of multistep HTM filling process, should decrease the series resistance of the cell. Both the reduced series resistance and the longer electron lifetime contribute to the improvements in the device performance for the solid-state DSC.

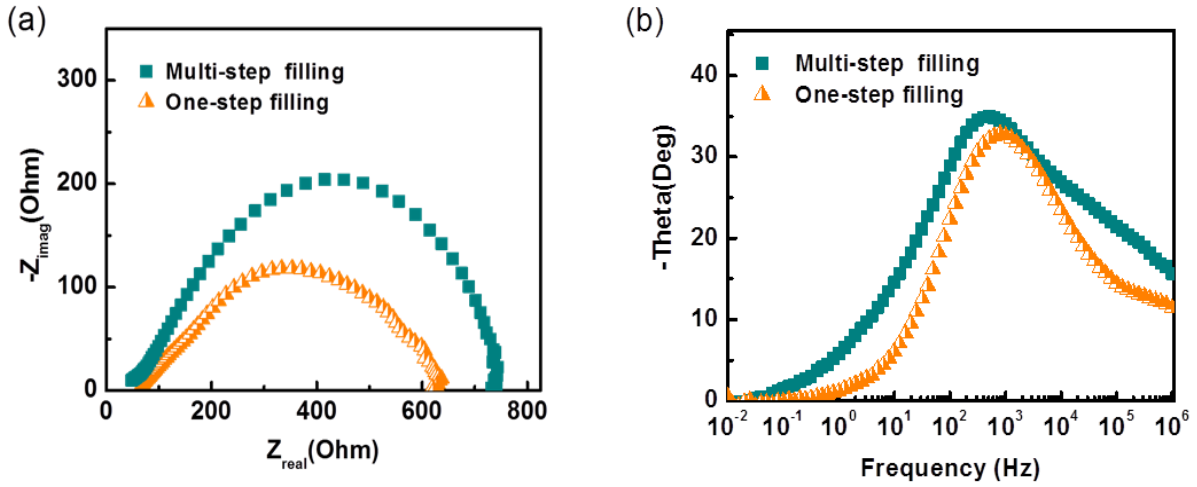

Figure 35. EIS spectra under illumination of AM 1.5G simulated sunlight of two representative solid-state DSCs. (a) Nyquist plots. (b) Bode phase angle versus frequency plots.

6.2 CONCLUSIONS

The development of the multilayer nanowire arrays and the multistep filling process represent significant advancements in the development of solid-state DSCs. It opens further opportunities for improvement of solid-state DSCs by simultaneous use of a range of strategies, such as using dyes with a high extinction coefficient,[106] using alternate HTMs and dopants[105, 112-114] and by cosensitization or using energy relay dyes.[115-117] Another area of improvement could be further increasing the thickness of the photoanode which would result in better light harvesting efficiency. It should be noted that though the probability of electron-hole recombination increases with the nanowire length, no significant increase was observed when the thickness of the nanowire arrays was increased from 10 to 50 μm.

7.0 VERTICALLY ORDERED TIN BASED NANOTUBE ARRAYS AS HIGH CAPACITY ANODE MATERIAL FOR LITHIUM-ION BATTERIES

7.1 INTRODUCTION

We had earlier discussed the unique advantages of vertically ordered nanostructures for Lithium-Ion Batteries (LIBs) in Section **1.2**. We have fabricated and evaluated the performance of LIBs using our SnO_2 nanotube arrays as an anode material. The nanotube arrays, grown on a Ti foil were directly used as an anode material in LIB and they delivered a reversible capacity of 610 mAh/g at a cycling rate of 200 mA/g. A large irreversible capacity loss was observed after the first discharge cycle for our cell using SnO_2 nanotube array as the anode. This irreversible capacity loss is a characteristic drawback for SnO_2-based devices. The reason for this is the irreversible reduction of SnO_2 to Sn resulting in the formation of irreversible Li_2O accompanied by electrolyte decomposition during the first discharge cycle.

This Li_2O matrix has an advantage in that it provides a facile environment for subsequent alloying and dealloying reactions whilst prevent agglomeration of Sn particles. However, it may also lead to excessive blocking of the Sn sites, thereby limiting the rechargeable capacity for the battery. One alternative to overcoming this is to use composite Sn/SnO_2 anodes which would help in limiting the Li_2O formation and hence in reducing the irreversible capacity loss. With the intention of reducing the irreversible capacity loss, we have fabricated hybrid nanotube arrays

(containing a mixture of Sn, SnO and SnO_2) by thermal reduction of the aforementioned nanotube arrays. The hybrid nanotube arrays exhibited a significantly lower irreversible capacity loss after the first discharge and also delivered higher capacities and improved cycling capabilities. The hybrid nanotube arrays delivered a capacity of 710 mAh/g after 80 cycles with a low capacity fade.

7.2 EXPERIMENTAL METHODS

7.2.1 Synthesis of arrays of ZnO nanowire, SnO_2 nanotube, and hybrid nanotubes arrays

ZnO nanowires and SnO_2 nanotube arrays were prepared by the same method described by us earlier in Chapter **2.0** and Chapter **3.0** respectively. The main difference was the substrate used for this part of the work. Instead of a conducting glass substrate, a Ti substrate was used for growing the nanostructures for LIBs. For synthesizing hybrid nanotube arrays, the SnO_2 nanotube array was subjected to thermal reduction in a H_2 atmosphere. Reduction was carried out by placing the SnO_2 nanotube array in a furnace maintained under a 30 kPa H_2 pressure at 400°C for 1 hour.

7.2.2 Fabrication and Characterization of Lithium-ion Batteries

The electrochemical measurements were carried out by fabricating 2032 coin cell LIBs in a half cell configuration using Li foil as counter electrode and 1 M $LiPF_6$ in 1:1 v/v mixture of ethylene carbonate (EC) and dimethyl carbonate (DMC) as the electrolyte. The nanotube arrays

grown on Ti substrate were directly used as anode. The typical active material loading was 1-2 mg. A polypropylene film was used as the separator. The coin cells were assembled in a glove box with an inert atmosphere. The cells were galvanostatically cycled in a fixed voltage window of 0.02 - 1.20 V versus Li/Li^+ at a constant current density of 200 mA/g.

7.3 RESULTS AND DISCUSSIONS

We have grown ordered SnO_2 nanotube arrays by using ZnO nanowires as a sacrificial template using the method described earlier.[118] The process starts with growing vertically aligned ZnO nanowires directly on Ti substrate by a hydrothermal method. This is followed by conversion of ZnO nanowire arrays to SnO_2 nanotubes via SnO_2 deposition and simultaneous ZnO dissolution by placing the ZnO nanowire array in an aqueous solution of $(NH_4)_2SnF_6$ and H_3BO_3. The detailed explanation for the method used for synthesizing these ordered SnO_2 nanotube arrays has been described in Section **3.2.2**.

7.3.1 Performance of SnO_2 Nanotube Arrays as Anode Material

The primary motive behind this part of the work was to analyze the performance of these ordered SnO_2 nanotube array as an anode in LIB. The synthesized nanotube array fabricated on Ti is used directly as the anode without addition of any additives or binders. In order to understand the electrochemical processes taking place within the cell we studied the differential capacity versus voltage plots, shown in **Figure 36a**. These plots were obtained by performing galvanostatic cycling in a voltage window of 0.02 – 1.20 V. The cycling rate was fixed at 200

mA/g. The first discharge curve started from the open-circuit voltage of the cell which was around 2.70 V. The corresponding first discharge capacity was very high, that is 1650 mAh/g, which is higher than the theoretical value. The higher than expected capacity can be attributed to surface-electrolyte interphase (SEI) film formation due to electrolyte decomposition. Three distinct peaks were observed during the first discharge cycle. The peak located at 1.0 V corresponds to the irreversible reduction of SnO_2 to Sn resulting in the formation of Li_2O as denoted by equation 7.1. The subsequent peaks observed at 0.5 V and 0.25 V could be attributed to the alloying reaction of Li and Sn with different Li content. This alloying reaction is denoted by the forward reaction equation 7.2.

$$SnO_2 + 4Li + 4e^- \rightarrow Sn + Li_2O \tag{7.1}$$

$$xLi^+ + xe^- + Sn \leftrightarrow Li_xSn \tag{7.2}$$

A broad peak observed at around 0.6 V during the first charge cycle could be attributed to the Li dealloying reaction denoted by the backward reaction in equation 7.2. The peak corresponding to equation 1 at 1.0 V disappeared after the first few cycles. These observations are consistent with other reports on SnO_2-based devices.[29, 34, 42] **Figure 36b** shows the typical charge-discharge capacities and the corresponding columbic efficiency for the first 20 cycles for the LIB fabricated with SnO_2 nanotube arrays as the anode material. After a very high first discharge capacity, the observed capacity during the first charge was 694.2 mAh/g, resulting in a columbic efficiency of 42.1%. This large irreversible loss after the first discharge can be attributed to electrolyte decomposition and the irreversible reaction denoted by equation 7.1. The SnO_2 nanotube array delivered a capacity of ≈ 600 mAh/g after 20 cycles.

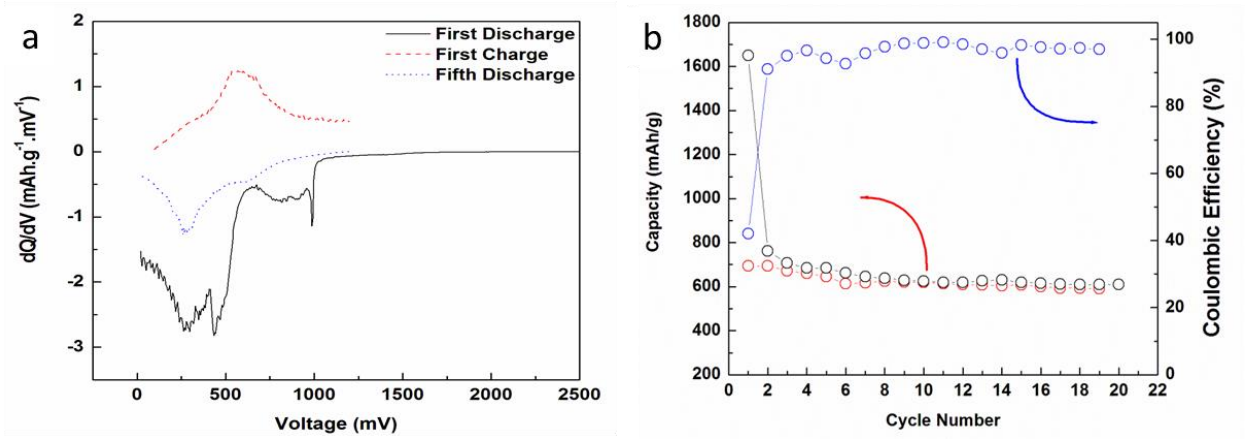

Figure 36. Electrochemical performance of SnO_2 nanotube array electrode. (a) Differential capacity versus voltage plots. (b) Cycling performance and coulombic efficiency at 200 mA/g cycling rate.

7.3.2 Performance of Hybrid Nanotube Arrays as Anode Material

With the intention of reducing the irreversible capacity loss and attain higher recyclable capacities, we have synthesized hybrid nanotubes consisting of a mixture of Sn, SnO and SnO_2 phases. Hybrid nanotube arrays were formed by thermal reduction. The SnO_2 nanotubes were exposed to a H_2 environment and heated at a temperature of 400°C for 1 h in a furnace. A stream containing 20% H_2 was passed through the furnace at a flow rate of 500 sccm to maintain the reducing environment. The result of the thermal reduction was the formation of hybrid nanotubes consisting of Sn, SnO and SnO_2 domains. The nanotube morphology was retained following this partial thermochemical reduction as can be seen in the SEM image in **Figure 37a**. The hybrid nanotubes formed after the thermal reduction were slightly thinner than the SnO_2 nanotubes. Peaks corresponding to Sn, SnO and SnO_2 were observed in the XRD pattern shown in **Figure 37b**, confirming the hybrid nature of our nanotubes. The SnO_2 peaks were sharper as compared to the XRD pattern for pure SnO_2 nanotubes indicating that the reduction process was accompanied by simultaneous particle growth for SnO_2. The nanotube morphology could also be

clearly seen in the TEM image in the inset of **Figure 37c**. **Figure 37c** and **Figure 37d** show the HRTEM image of the hybrid nanotube taken at the edge of the wall and the center of the wall, respectively. The walls of the tube are polycrystalline in nature and consist of a mixture of Sn, SnO and SnO_2 crystals. The lattice spacing measurements shown in the HRTEM image can be ascribed to (110) plane of SnO_2, (200) plane of Sn and (110) plane of SnO, respectively. For the thermal reduction, a range of temperatures from 200°C to 700°C were investigated. At lower temperatures, negligible or no reduction of SnO_2 was observed whereas at higher temperatures, SnO_2 reduced completely to Sn, resulting in subsequent melting and agglomeration of Sn. Under our conditions, we were able to obtain a hybrid mixture, thereby successfully reducing the oxide content, while at the same time the nanotube morphology was retained.

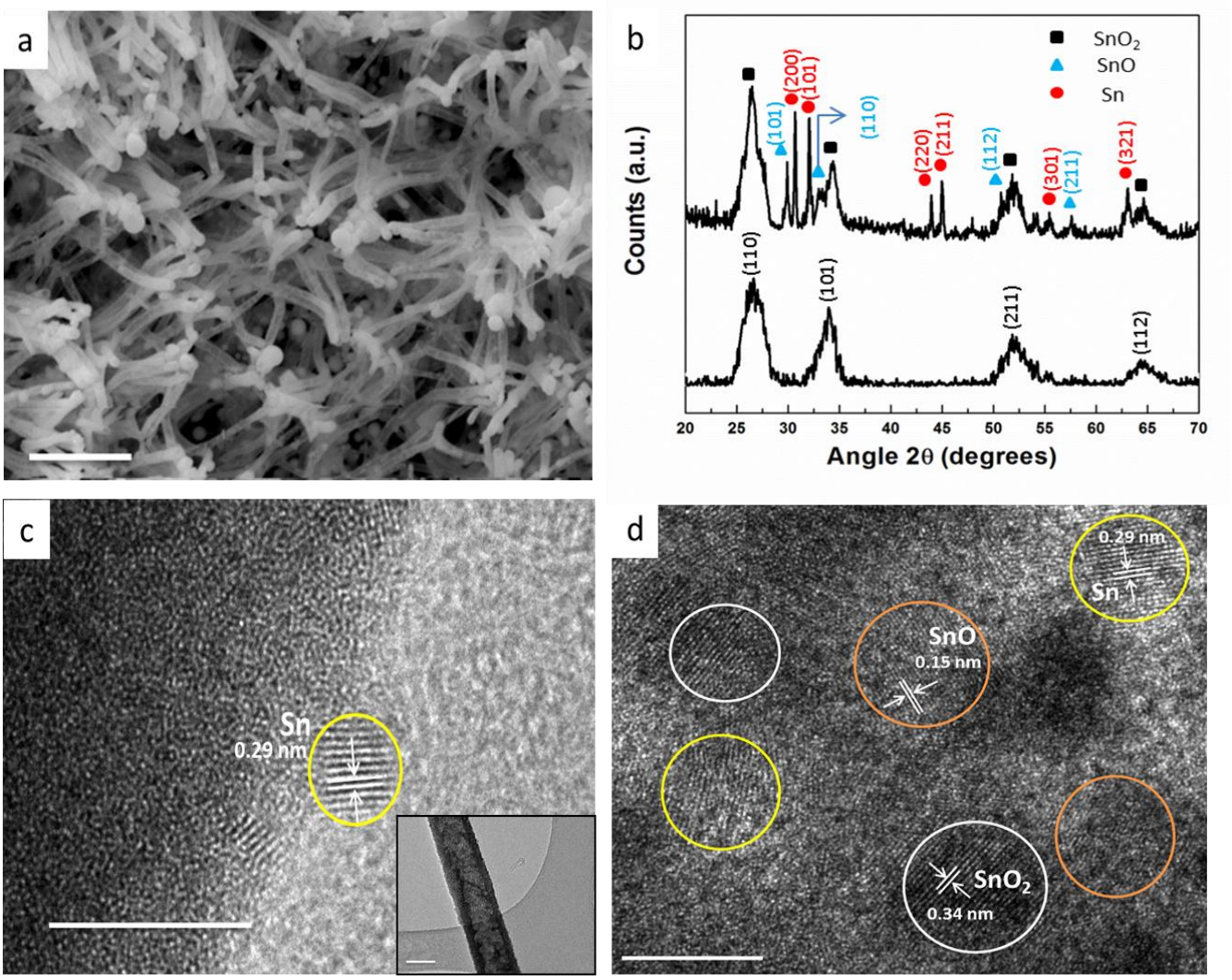

Figure 37. Hybrid nanotube arrays. (a) Top-view SEM image of hybrid nanotube arrays after thermal reduction. Scale bar, 2 μm. (b) XRD pattern for hybrid nanotube array. (c) HRTEM image at the edge of the wall of hybrid nanotube showing Sn crystal. Scale bar, 10nm. (d) HRTEM image at the wall of the nanotube showing polycrystalline nature of the hybrid nanotube. Scale bar, 5nm.

Figure 38b shows the charge-discharge curves and the coulombic efficiencies for LIBs fabricated with the hybrid nanotube array as the anode. The cycling rate was again fixed at 200 mA/g. As compared to the SnO_2 nanotube array, a lower first discharge capacity is observed, 1210 mAh/g versus 1650 mAh/g. The first charge capacity was 778 mAh/g and the corresponding coulombic efficiency calculated is 64.25% for the first cycle. This increase in capacity retention is a significant improvement over bare-SnO_2 nanotube arrays and is also higher than previous reports for Sn-based systems.[42, 119] The hybrid nanotubes also exhibited better stability and higher charge retention delivering a capacity of 710 mAh/g after 80 cycles.

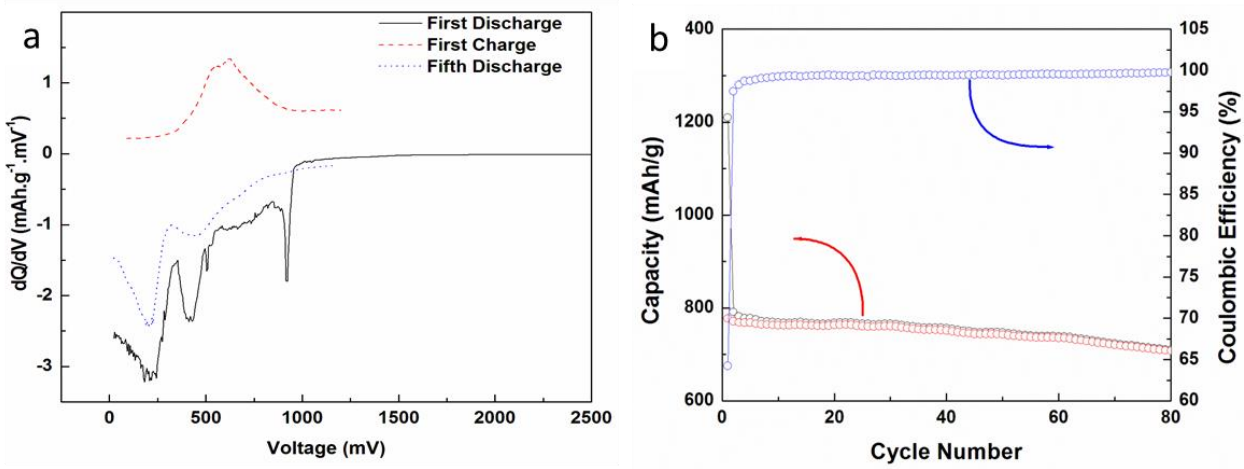

Figure 38. Electrochemical performance of hybrid nanotube array electrode. (a) Differential capacity versus voltage plots. (b) Cycling performance and coulombic efficiency at 200 mA/g cycling rate.

To better understand the improved performance of our hybrid nanotube arrays, we studied the differential capacity versus voltage plots shown in **Figure 38a**. As seen in the differential capacity plots for pure SnO_2 nanotubes, in **Figure 36a**, a peak was observed at around 0.95 V during the first discharge which disappeared for the subsequent cycles. This peak corresponds to the irreversible formation of Li_2O. However, we believe a lower SnO_2 content, in

the case of the hybrid nanotubes, led to lower Li_2O formation in the first cycle which can be interpreted from the resultant lower first discharge capacity. Thus, we can conclude that Li_2O formation was suppressed using our hybrid nanotube arrays. Furthermore, the peak corresponding to the alloying reaction of Li and Sn shifted to a slightly lower potential as compared to the pure SnO_2 nanotube array anode (0.23 V *versus* 0.25 V) indicating higher lithium alloying content for the hybrid nanotubes, resulting in higher capacities for subsequent cycles.

Differences were also observed in the differential capacity plots for the pure and hybrid nanotubes during the charge cycle. A single anodic peak is observed at around 0.6 V during the first charge cycle for the pure SnO_2 nanotubes. On the other hand, the differential capacity plot for the hybrid nanotubes during the first charge cycle shows two distinct peaks at 0.5 V and 0.6 V indicating a stage-wise delithiation mechanism. This goes to show the lithium extraction is taking place in a stage-wise manner for hybrid nanotubes as compared to a single stage delithiation in case of SnO_2 nanotubes. This stage-wise delithiation mechanism should result in more complete removal of lithium resulting in higher capacity. The improved performance due to stage-wise delithiation mechanism because of the presence of nanoscale Sn particles has been reported before.[120]

It is believed that an SnO phase is formed due to the ability of metal nanoparticles (Sn) to reduce the Li_2O to form metal oxide (SnO) *via* equation 4.[28, 34] The lithiation mechanism of the hybrid nanotubes can be expressed as:

$$SnO_2 + 2Li^+ + 2e^- \rightarrow SnO + Li_2O \quad (7.3)$$

$$SnO + 2Li^+ + 2e^- \leftrightarrow Sn + Li_2O \quad (7.4)$$

$$xLi^+ + xe^- + Sn \leftrightarrow Li_xSn \quad (7.5)$$

The presence of SnO, after repeated cycling, was confirmed from the ex-situ XRD performed on the hybrid nanotube anode after 20 cycles of charge and discharge shown in **Figure 39**. This reversible formation of SnO should lead to higher capacities for subsequent cycles by preventing agglomeration of Sn nanoparticles. Furthermore, the Sn and SnO phases also have a higher theoretical capacity as well as faster kinetics for Li_xSn formation as compared to SnO_2.[40] In comparison, for SnO_2 anodes, majority of the nanoparticles comprising the pure SnO_2 nanotubes get completely reduced to Sn while some SnO_2 remains unreacted after the first discharge cycle. The reduction of SnO_2 also leads to large amount of Li_2O formation which may block some Sn alloying sites resulting in capacity fade. Hence, the improved capacity retention observed in case of hybrid nanotubes can be attributed to the presence of an Sn and an SnO phase, as well as significant reduction in Li_2O formation.

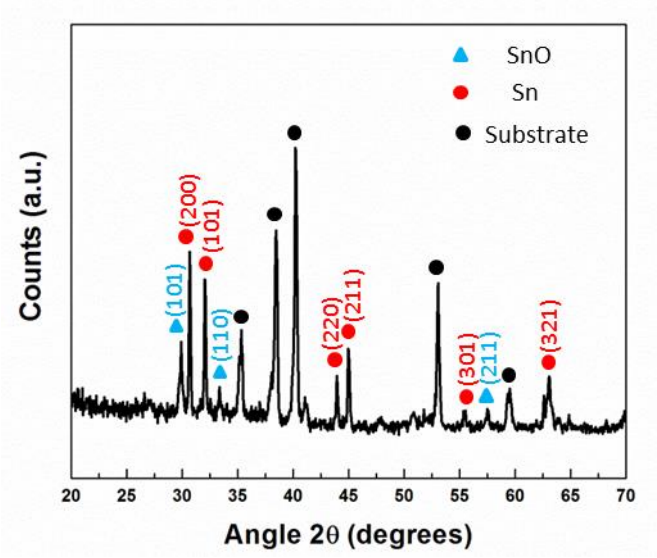

Figure 39. XRD pattern for the hybrid nanotube array after 20 cycles of charge and discharge.

The hybrid nanotube arrays also exhibit a high capacity and better cycling stability when compared to other such hybrid particle-based Sn electrodes.[29] The performance was also

comparable to that reported by Meduri *et al* using hybrid nanowire structures.[34] On the other hand, the performance of our LIBs based on pure SnO_2 nanotube arrays is significantly better than their pure phase SnO_2 nanowires. The improved performance of our nanotube arrays could be attributed to the unique advantages offered by their hierarchical structure. The vertically ordered nanotube structure, grown directly on the current collecting substrate, ensures good electrical contact as well as high electrolyte contact area. The nanotube morphology also provides sufficient space for withstanding the strains caused by expansion due to lithium insertion and extraction. Hence, the nanotube structures can deliver a high capacity and good cycleability. Another major advantage, of using these ordered nanotube arrays, is that they can be grown directly on the current collector by our method and hence do not require the use of any binders or conducting additives. This should help increase the loading of the active material for LIBs resulting in higher capacities.

7.4 CONCLUSIONS

We have developed a process to fabricate ordered SnO_2 nanotube arrays directly on current collecting substrate by using a sacrificial temperature approach. The entire synthesis was carried out in aqueous solution at low temperatures making the process attractive for scale-up. These SnO_2 nanotube arrays delivered a rechargeable capacity of 600 mAh/g after 20 cycles when used anode in LIBs. In addition we have also developed a strategy to fabricate hybrid nanotube arrays with higher Sn content with the intention of reducing the irreversible capacity loss in the first cycle as well as achieve better capacity retention. These hybrid nanotubes exhibit a reversible storage capacity of 710 mAh/g after 80 cycles. The nanotube arrays should be able

to better withstand the strains generated by lithium insertion/extraction, resulting in better cycling stability. The better performance of the hybrid mixture can be attributed to a lower SnO_2 content, which leads to lower irreversible formation of Li_2O, as well as the presence of Sn and SnO phases.

8.0 SUMMARY AND FUTURE OUTLOOK

Vertically ordered (1-D) nanostructures provide a promising alternative to conventional nanoparticle films used as electrode materials for energy conversion and storage devices. These 1-D nanostructures, in forms of nanowires or nanotubes, help maximize the electrode surface area while maintaining good electrical connections to the current collector. We have successfully fabricated and integrated such vertically ordered nanostructures in dye-sensitized solar cells (DSCs) and lithium-ion batteries (LIBs) and demonstrated improvement in device performance. Our work consists of three distinct parts: In the first part, i.e. Chapter **3.0** and Chapter **4.0** we have spoken about the advantages and applications of vertically ordered nanostructures for DSCs. In Chapter **5.0** and Chapter **6.0** we have explored the potential advantages of the synthesized nanostructures for solid-state DSCs which hold promise for higher stability than their liquid-state counterparts. Finally, in Chapter **7.0** we have studied the application of vertically ordered Sn-based nanotube arrays as a potential anode material in LIBs.

8.1.1 Vertically Ordered Nanostructures for DSCs

In Chapter **3.0** we have described the method developed in our lab for fabricating vertically ordered SnO_2 nanotube arrays by a low temperature hydrothermal method. The method involved using ZnO nanowire array as a sacrificial template and all the steps are easily scalable.

We integrated these nanotube arrays in DSCs and studied the electron recombination kinetics. We observed that the electron recombination lifetimes are much higher for SnO_2 nanotube based devices than other photoanodes. These results open up the possibility of further improvement by using redox mediators with faster kinetics, which would otherwise be hampered by fast recombination of electrons.

In Chapter **4.0** we have described a convenient approach to synthesize multilayer assembly of high surface area of nanowire arrays. The main motivation behind this work was to improve the surface area of the vertically ordered nanostructures which is one of the main factors limiting their efficiencies. The internal surface area of our multilayer nanowire assembly is more than five times greater than the single layer array and we were able to achieve power conversion efficiencies of up to 7%.

In the ongoing work in our lab, we are currently trying to convert our multilayer nanowire arrays into SnO_2 nanotubes. This should enable us to take the dual advantage of the high roughness factors offered by the multilayer assembly as well as the excellent electronic properties of SnO_2 nanotubes. Another exciting idea is to fabricate hybrid devices in which nanoparticles are coated along the walls and between the nanotubes. The nanoparticle network would help boost the surface area for dye adsorption and the underlying nanotube framework would ensure efficient electron transport and collection. Our hypothesis is that when these nanoparticle networks are coated on the nanotubes, they will absorb the electron from the dye and pass it onto the nanotube framework. The electrons could then be collected at the current collecting substrate without them having to pass through a tortuous network, resulting in improved device performance.

8.1.2 Vertically Ordered Nanostructures for Solid-State DSCs

A major factor inhibiting the commercialization of DSCs is the volatile nature of the liquid electrolyte used for hole transport. Replacing these liquid electrolytes with solid HTMs represents an ideal solution to overcome the problem of device stability. In Chapter **5.0** and Chapter **6.0** we have successfully being able to incorporate 1-D nanostructures in the device architecture for solid-state DSCs and demonstrated unique advantages over the traditional nanoparticle framework. Using our multilayer nanowire assembly, we were able to achieve a power conversion efficiency of 5.65% which is comparable to the nanoparticle based solid-state DSCs. The photoanode made of such a vertically ordered array allows for effective filling of the photoanode with the solid HTM while retaining high electron collection efficiency. Due to these advantages, vertically ordered nanostructures represent great alternatives for further improvement of solid-state DSCs. Use of alternate dyes and HTMs should lead to improved device performance and higher efficiencies.

8.1.3 Vertically Ordered Nanostructures for LIBs

In Chapter **7.0** we have described the fabrication of hybrid Sn-based nanotube arrays and their application as anode material in LIBs. The hybrid nanotubes exhibited reduced first cycle irreversible loss as well as excellent capacity retention. The primary reason for the reduced irreversible loss in the hybrid nanotubes was higher Sn content and subsequent reduction in Li_2O formation. The good cycling stability could be attributed to the ability of the nanotube structure to better withstand the strains generated by lithium insertion and extraction. The use of such vertically oriented hybrid nanotubes could be extended to other anode materials with a higher

theoretical capacity, such as Si and Ge, opening up possibilities for fabricating LIBs with better stability and higher capacity retention.

APPENDIX A

INCIDENT PHOTON TO CURRENT CONVERSION EFFICIENCY (IPCE)

Incident photon to current conversion efficiency (IPCE) is a measure of the ratio of photons that generate electrons in the external circuit to incident photons of monochromatic light. For our work, IPCE was calculated by chronoamperometric scan using a monochromatic light source. Wavelength of incident light was changed using a monochromator and the corresponding short-circuit current (J_{SC}) was determined. IPCE can then be calculated using the following formula:

$$IPCE = \frac{J_{SC}}{P} \times \frac{1240}{\lambda} \times 100$$

where J_{SC} is the short-circuit current in mA/cm^2, P is the power of the incident light in W/cm^2 and λ is the wavelength of the incident monochromatic light in nm.

BIBLIOGRAPHY

1. Liu, J., et al., *Oriented Nanostructures for Energy Conversion and Storage.* ChemSusChem, 2008. **1**(8-9): p. 676-697.

2. Smalley, R.E., *Future global energy prosperity: The terawatt challenge.* MRS Bulletin, 2005. **30**(6): p. 412-417.

3. Hochbaum, A.I. and P. Yang, *Semiconductor Nanowires for Energy Conversion.* Chemical Reviews, 2009. **110**(1): p. 527-546.

4. P. Norling, F.W.-B., T. M. Masciangioli, *Water and Sustainable Development: Opportunities for the Chemical Sciences,* in *A Workshop Report to the Chemical Sciences Roundtable,* 2004.

5. Arico, A.S., et al., *Nanostructured materials for advanced energy conversion and storage devices.* Nat Mater, 2005. **4**(5): p. 366-377.

6. Maier, J., *Nanoionics: ion transport and electrochemical storage in confined systems.* Nat Mater, 2005. **4**(11): p. 805-815.

7. Gonçalves, L.M., et al., *Dye-sensitized solar cells: A safe bet for the future.* Energy & Environmental Science, 2008. **1**(6): p. 655.

8. Graetzel, M., *Solar Energy Conversion by Dye-Sensitized Photovoltaic Cells.* Inorganic Chemistry, 2005. **44**(20): p. 6841-6851.

9. Hoffmann, W., *PV solar electricity industry: Market growth and perspective.* Solar Energy Materials and Solar Cells, 2006. **90**(18-19): p. 3285-3311.

10. Green, M.A., et al., *Solar cell efficiency tables (version 41).* Progress in Photovoltaics, 2013. **21**(1): p. 1-11.

11. O'Regan, B. and M. Gratzel, *A low-cost, high-efficiency solar cell based on dye-sensitized colloidal TiO_2 films.* Nature, 1991. **353**(6346): p. 737-740.

12. Yella, A., et al., *Porphyrin-Sensitized Solar Cells with Cobalt (II/III)–Based Redox Electrolyte Exceed 12 Percent Efficiency.* Science, 2011. **334**(6056): p. 629-634.

13. Grätzel, M., *Dye-sensitized solar cells.* Journal of Photochemistry and Photobiology C: Photochemistry Reviews, 2003. **4**(2): p. 145-153.

14. Nazeeruddin, M.K., et al., *Conversion of Light to Electricity by cis-XzBis(2,2'-bipyridyl-4,4'-dicarboxylate)ruthenium(11) Charge-Transfer Sensitizers (X = C1-, Br-, I-, CN-, and SCN-) on Nanocrystalline TiO_2 Electrodes.* Journal of American Chemical Society, 1993. **115**: p. 6382-6390.

15. Li, B., et al., *Review of recent progress in solid-state dye-sensitized solar cells.* Solar Energy Materials and Solar Cells, 2006. **90**(5): p. 549-573.

16. O'Regan, B.C. and F. Lenzmann, *Charge Transport and Recombination in a Nanoscale Interpenetrating Network of n-Type and p-Type Semiconductors: Transient Photocurrent and Photovoltage Studies of TiO_2/Dye/CuSCN Photovoltaic Cells.* The Journal of Physical Chemistry B, 2004. **108**(14): p. 4342-4350.

17. O'Regan, B., et al., *A Solid-State Dye-Sensitized Solar Cell Fabricated with Pressure-Treated P25−TiO_2 and CuSCN: Analysis of Pore Filling and IV Characteristics.* Chemistry of Materials, 2002. **14**(12): p. 5023-5029.

18. Schmidt-Mende, L., S.M. Zakeeruddin, and M. Gratzel, *Efficiency improvement in solid-state-dye-sensitized photovoltaics with an amphiphilic Ruthenium-dye.* Applied Physics Letters, 2005. **86**(1): p. 013504.

19. Snaith, H.J. and L. Schmidt-Mende, *Advances in Liquid-Electrolyte and Solid-State Dye-Sensitized Solar Cells.* Advanced Materials, 2007. **19**(20): p. 3187-3200.

20. Ding, I.K., et al., *Pore-Filling of Spiro-OMeTAD in Solid-State Dye Sensitized Solar Cells: Quantification, Mechanism, and Consequences for Device Performance.* Advanced Functional Materials, 2009. **19**(15): p. 2431-2436.

21. Tarascon, J.M. and M. Armand, *Issues and challenges facing rechargeable lithium batteries.* Nature, 2001. **414**(6861): p. 359-367.

22. Armand, M. and J.M. Tarascon, *Building better batteries.* Nature, 2008. **451**(7179): p. 652-657.

23. Park, K.-S., et al., *Long-term, high-rate lithium storage capabilities of TiO_2 nanostructured electrodes using 3D self-supported indium tin oxide conducting nanowire arrays.* Energy & Environmental Science, 2011. **4**(5): p. 1796-1801.

24. Cui, L.-F., et al., *Crystalline-Amorphous Core-Shell Silicon Nanowires for High Capacity and High Current Battery Electrodes.* Nano Letters, 2009. **9**(1): p. 491-495.

25. Li, Y., B. Tan, and Y. Wu, *Mesoporous CO_3O_4 nanowire arrays for lithium ion batteries with high capacity and rate capability.* Nano Letters, 2008. **8**(1): p. 265-270.

26. Chan, C.K., et al., *High-performance lithium battery anodes using silicon nanowires.* Nature Nanotechnology, 2008. **3**(1): p. 31-35.

27. Sharma, Y., et al., *Nanophase $ZnCo_2O_4$ as a high performance anode material for Li-ion batteries.* Advanced Functional Materials, 2007. **17**(15): p. 2855-2861.

28. Poizot, P., et al., *Nano-sized transition-metaloxides as negative-electrode materials for lithium-ion batteries.* Nature, 2000. **407**(6803): p. 496-499.

29. Sivashanmugam, A., et al., *Electrochemical behavior of Sn/SnO2 mixtures for use as anode in lithium rechargeable batteries.* Journal of Power Sources, 2005. **144**(1): p. 197-203.

30. Wang, X.-L., et al., *Sn/SnOx Core-Shell Nanospheres: Synthesis, Anode Performance in Li Ion Batteries, and Superconductivity.* Journal of Physical Chemistry C, 2010. **114**(35): p. 14697-14703.

31. Kim, M.G., S. Sim, and J. Cho, *Novel Core-Shell Sn-Cu Anodes for Lithium Rechargeable Batteries Prepared by a Redox-Transmetalation Reaction.* Advanced Materials, 2010. **22**(45): p. 5154.

32. Lee, S.H., et al., *Fabrication of Carbon-Encapsulated Mono- and Bimetallic (Sn and Sn/Sb Alloy) Nanorods. Potential Lithium-Ion Battery Anode Materials.* Chemistry of Materials, 2009. **21**(11): p. 2306-2314.

33. Idota, Y., et al., *Tin-based amorphous oxide: A high-capacity lithium-ion-storage material.* Science, 1997. **276**(5317): p. 1395-1397.

34. Meduri, P., et al., *Hybrid Tin Oxide Nanowires as Stable and High Capacity Anodes for Li-Ion Batteries.* Nano Letters, 2009. **9**(2): p. 612-616.

35. Li, N.C. and C.R. Martin, *A high-rate, high-capacity, nanostructured Sn-based anode prepared using sol-gel template synthesis.* Journal of the Electrochemical Society, 2001. **148**(2): p. A164-A170.

36. Courtney, I.A. and J.R. Dahn, *Electrochemical and in situ x-ray diffraction studies of the reaction of lithium with tin oxide composites.* Journal of the Electrochemical Society, 1997. **144**(6): p. 2045-2052.

37. Wachtler, M., M. Winter, and J.O. Besenhard, *Anodic materials for rechargeable Li-batteries.* Journal of Power Sources, 2002. **105**(2): p. 151-160.

38. Winter, M. and J.O. Besenhard, *Electrochemical lithiation of tin and tin-based intermetallics and composites.* Electrochimica Acta, 1999. **45**(1-2): p. 31-50.

39. Zhou, W., et al., *Epitaxial Growth of Branched alpha-Fe_2O_3/SnO_2 Nano-Heterostructures with Improved Lithium-Ion Battery Performance.* Advanced Functional Materials, 2011. **21**(13): p. 2439-2445.

40. Lim, A.-H., et al., *Biomineralized Sn-based multiphasic nanostructures for Li-ion battery electrodes.* Nanoscale, 2012. **4**(15): p. 4694-4701.

41. Wang, B., et al., *The dimensionality of Sn anodes in Li-ion batteries.* Materials Today, 2012. **15**(12): p. 544-552.

42. Liu, J., et al., *Direct growth of SnO_2 nanorod array electrodes for lithium-ion batteries.* Journal of Materials Chemistry, 2009. **19**(13): p. 1859-1864.

43. Taberna, P.L., et al., *High rate capabilities Fe_3O_4-based Cu nano-architectured electrodes for lithium-ion battery applications.* Nat Mater, 2006. **5**(7): p. 567-73.

44. Sides, C.R. and C.R. Martin, *Nanostructured electrodes and the low-temperature performance of Li-ion batteries.* Advanced Materials, 2005. **17**(1): p. 125-+.

45. Xu, C., et al., *Preferential Growth of Long ZnO Nanowire Array and Its Application in Dye-Sensitized Solar Cells.* The Journal of Physical Chemistry C, 2010. **114**(1): p. 125-129.

46. Law, M., et al., *Nanowire dye-sensitized solar cells.* Nat Mater, 2005. **4**(6): p. 455-9.

47. Chappel, S., S.-G. Chen, and A. Zaban, *TiO_2-Coated Nanoporous SnO_2 Electrodes for Dye-Sensitized Solar Cells.* Langmuir, 2002. **18**(8): p. 3336-3342.

48. Sayama, K., H. Sugihara, and H. Arakawa, *Photoelectrochemical Properties of a Porous Nb2O5 Electrode Sensitized by a Ruthenium Dye.* Chemistry of Materials, 1998. **10**(12): p. 3825-3832.

49. Ramasamy, E. and J. Lee, *Ordered Mesoporous SnO_2−Based Photoanodes for High-Performance Dye-Sensitized Solar Cells.* The Journal of Physical Chemistry C, 2010. **114**(50): p. 22032-22037.

50. Hendry, E., et al., *Local Field Effects on Electron Transport in Nanostructured TiO_2 Revealed by Terahertz Spectroscopy.* Nano Letters, 2006. **6**(4): p. 755-759.

51. Seager, C.H. and S.M. Myers, *Quantitative comparisons of dissolved hydrogen density and the electrical and optical properties of ZnO.* Journal of Applied Physics, 2003. **94**(5): p. 2888-2894.

52. Martinson, A.B.F., et al., *New Architectures for Dye-Sensitized Solar Cells.* Chemistry – A European Journal, 2008. **14**(15): p. 4458-4467.

53. Green, A.N.M., et al., *Charge Transport versus Recombination in Dye-Sensitized Solar Cells Employing Nanocrystalline TiO_2 and SnO_2 Films.* The Journal of Physical Chemistry B, 2005. **109**(25): p. 12525-12533.

54. Benkö, G., et al., *Photoinduced Electron Injection from Ru(dcbpy)2(NCS)2 to SnO_2 and TiO_2 Nanocrystalline Films.* Journal of the American Chemical Society, 2003. **125**(5): p. 1118-1119.

55. Kay, A. and M. Grätzel, *Dye-Sensitized Core−Shell Nanocrystals: Improved Efficiency of Mesoporous Tin Oxide Electrodes Coated with a Thin Layer of an Insulating Oxide.* Chemistry of Materials, 2002. **14**(7): p. 2930-2935.

56. Tiwana, P., et al., *Electron Mobility and Injection Dynamics in Mesoporous ZnO, SnO_2, and TiO_2 Films Used in Dye-Sensitized Solar Cells.* ACS Nano, 2011. **5**(6): p. 5158-5166.

57. Chappel, S. and A. Zaban, *Nanoporous SnO_2 electrodes for dye-sensitized solar cells: improved cell performance by the synthesis of 18nm SnO_2 colloids.* Solar Energy Materials and Solar Cells, 2002. **71**(2): p. 141-152.

58. Gubbala, S., et al., *Band-Edge Engineered Hybrid Structures for Dye-Sensitized Solar Cells Based on SnO_2 Nanowires.* Advanced Functional Materials, 2008. **18**(16): p. 2411-2418.

59. Xu, C., et al., *Ordered TiO_2 Nanotube Arrays on Transparent Conductive Oxide for Dye-Sensitized Solar Cells.* Chemistry of Materials, 2010. **22**(1): p. 143-148.

60. Lee, J.-H., et al., *Fabrication of Aligned TiO_2 One-Dimensional Nanostructured Arrays Using a One-Step Templating Solution Approach.* The Journal of Physical Chemistry B, 2005. **109**(27): p. 13056-13059.

61. Deki, S., et al., *Liquid-Phase Infiltration (LPI) Process for the Fabrication of Highly Nano-Ordered Materials.* Chemistry of Materials, 2004. **16**(9): p. 1747-1750.

62. Birks, L.S. and H. Friedman, *Particle Size Determination from X-Ray Line Broadening.* Journal of Applied Physics, 1946. **17**(8): p. 687-692.

63. Ishikawa, K., K. Yoshikawa, and N. Okada, *Size effect on the ferroelectric phase transition in $PbTiO_3$ ultrafine particles.* Physical Review B, 1988. **37**(10): p. 5852-5855.

64. Wang, Y.-L., et al., *Hydrothermal preparation and photoelectrochemical performance of size-controlled SnO_2 nanorod arrays.* CrystEngComm, 2010. **12**(12): p. 4024.

65. Qian, J., et al., *TiO_2-Coated Multilayered SnO_2 Hollow Microspheres for Dye-Sensitized Solar Cells.* Advanced Materials, 2009. **21**(36): p. 3663-3667.

66. Xu, C., et al., *Multilayer Assembly of Nanowire Arrays for Dye-Sensitized Solar Cells.* Journal of the American Chemical Society, 2011. **133**(21): p. 8122-8125.

67. Bisquert, J., et al., *Determination of Rate Constants for Charge Transfer and the Distribution of Semiconductor and Electrolyte Electronic Energy Levels in Dye-Sensitized Solar Cells by Open-Circuit Photovoltage Decay Method.* Journal of the American Chemical Society, 2004. **126**(41): p. 13550-13559.

68. Zaban, A., M. Greenshtein, and J. Bisquert, *Determination of the Electron Lifetime in Nanocrystalline Dye Solar Cells by Open-Circuit Voltage Decay Measurements.* ChemPhysChem, 2003. **4**(8): p. 859-864.

69. Bandaranayake, K.M.P., et al., *Dye-sensitized solar cells made from nanocrystalline TiO_2 films coated with outer layers of different oxide materials.* Coordination Chemistry Reviews, 2004. **248**(13–14): p. 1277-1281.

70. Lee, S., et al., *Two-Step Sol−Gel Method-Based TiO_2 Nanoparticles with Uniform Morphology and Size for Efficient Photo-Energy Conversion Devices.* Chemistry of Materials, 2010. **22**(6): p. 1958-1965.

71. Wang, Q., J.-E. Moser, and M. Grätzel, *Electrochemical Impedance Spectroscopic Analysis of Dye-Sensitized Solar Cells.* The Journal of Physical Chemistry B, 2005. **109**(31): p. 14945-14953.

72. Choi, H., et al., *An Efficient Dye-Sensitized Solar Cell with an Organic Sensitizer Encapsulated in a Cyclodextrin Cavity.* Angewandte Chemie International Edition, 2009. **48**(32): p. 5938-5941.

73. Adachi, M., et al., *Determination of Parameters of Electron Transport in Dye-Sensitized Solar Cells Using Electrochemical Impedance Spectroscopy.* The Journal of Physical Chemistry B, 2006. **110**(28): p. 13872-13880.

74. Song, J., et al., *Enhancement of Photogenerated Electron Transport in Dye-Sensitized Solar Cells with Introduction of a Reduced Graphene Oxide–TiO_2 Junction.* Chemistry – A European Journal, 2011. **17**(39): p. 10832-10837.

75. Xi, G. and J. Ye, *Correction to Ultrathin SnO_2 Nanorods: Template- and Surfactant-Free Solution Phase Synthesis, Growth Mechanism, Optical, Gas-Sensing, and Surface Adsorption Properties.* Inorganic Chemistry, 2010. **49**(7): p. 3553-3553.

76. Kim, D.-W., et al., *Highly Conductive Coaxial SnO_2−In_2O_3 Heterostructured Nanowires for Li Ion Battery Electrodes.* Nano Letters, 2007. **7**(10): p. 3041-3045.

77. Park, M.-S., et al., *Preparation and Electrochemical Properties of SnO_2 Nanowires for Application in Lithium-Ion Batteries.* Angewandte Chemie International Edition, 2007. **46**(5): p. 750-753.

78. Mor, G.K., et al., *Use of Highly-Ordered TiO_2 Nanotube Arrays in Dye-Sensitized Solar Cells.* Nano Letters, 2005. **6**(2): p. 215-218.

79. Feng, X., et al., *Vertically Aligned Single Crystal TiO_2 Nanowire Arrays Grown Directly on Transparent Conducting Oxide Coated Glass: Synthesis Details and Applications.* Nano Letters, 2008. **8**(11): p. 3781-3786.

80. Liu, B. and E.S. Aydil, *Growth of Oriented Single-Crystalline Rutile TiO_2 Nanorods on Transparent Conducting Substrates for Dye-Sensitized Solar Cells.* Journal of the American Chemical Society, 2009. **131**(11): p. 3985-3990.

81. Varghese, O.K., M. Paulose, and C.A. Grimes, *Long vertically aligned titania nanotubes on transparent conducting oxide for highly efficient solar cells.* Nat Nano, 2009. **4**(9): p. 592-597.

82. Zhong Lin, W., *ZnO nanowire and nanobelt platform for nanotechnology.* Materials Science and Engineering: R: Reports, 2009. **64**(3-4): p. 33-71.

83. Liu, J., et al., *Iron Oxide-Based Nanotube Arrays Derived from Sacrificial Template-Accelerated Hydrolysis: Large-Area Design and Reversible Lithium Storage.* Chemistry of Materials, 2009. **22**(1): p. 212-217.

84. Zhou, M., et al., *CdSe Nanotube Arrays on ITO via Aligned ZnO Nanorods Templating.* Chemistry of Materials, 2009. **22**(1): p. 64-69.

85. Orera, A. and P.R. Slater, *New Chemical Systems for Solid Oxide Fuel Cells.* Chemistry of Materials, 2009. **22**(3): p. 675-690.

86. Ellis, B.L., K.T. Lee, and L.F. Nazar, *Positive Electrode Materials for Li-Ion and Li-Batteries.* Chemistry of Materials, 2010. **22**(3): p. 691-714.

87. Tennakone, K., et al., *Dye-sensitized solid state photovoltaic cell based on composite zinc oxide/tin (IV) oxide films.* Journal of Physics D: Applied Physics, 1999. **32**(4): p. 374.

88. Kumara, G.R.R.A., et al., *Dye-sensitized solar cell with the hole collector p-CuSCN deposited from a solution in n-propyl sulphide.* Solar Energy Materials and Solar Cells, 2001. **69**(2): p. 195-199.

89. Rost, C., et al., *Semiconductor growth on porous substrates.* Materials Science and Engineering: B, 2000. **69-70**(0): p. 570-573.

90. Perera, V.P.S. and K. Tennakone, *Recombination processes in dye-sensitized solid-state solar cells with CuI as the hole collector.* Solar Energy Materials and Solar Cells, 2003. **79**(2): p. 249-255.

91. Smith, D.L. and V.I. Saunders, *The structure and polytypism of the [beta] modification of copper(I) thiocyanate.* Acta Crystallographica Section B, 1981. **37**(10): p. 1807-1812.

92. Zhong Lin, W., *Zinc oxide nanostructures: growth, properties and applications.* Journal of Physics: Condensed Matter, 2004. **16**(25): p. R829.

93. Schmidt-Mende, L. and J.L. MacManus-Driscoll, *ZnO – nanostructures, defects, and devices.* Materials Today, 2007. **10**(5): p. 40-48.

94. Postels, B., et al., *Dye-sensitized solar cells on the basis of ZnO nanorods.* Journal of the Korean Physical Society, 2008. **53**(1): p. 115-118.

95. O'Regan, B. and D.T. Schwartz, *Efficient Photo-Hole Injection from Adsorbed Cyanine Dyes into Electrodeposited Copper(I) Thiocyanate Thin Films.* Chemistry of Materials, 1995. **7**(7): p. 1349-1354.

96. O'Regan, B., et al., *Electrodeposited nanocomposite n-p heterojunctions for solid-state dye-sensitized photovoltaics.* Advanced Materials, 2000. **12**(17): p. 1263.

97. Wang, M., et al., *Solid-State Dye-Sensitized Solar Cells using Ordered TiO_2 Nanorods on Transparent Conductive Oxide as Photoanodes.* Journal of Physical Chemistry C, 2012. **116**(5): p. 3266-3273.

98. Bendall, J.S., et al., *An efficient DSSC based on ZnO nanowire photo-anodes and a new D-pi-A organic dye.* Energy & Environmental Science, 2011. **4**(8): p. 2903-2908.

99. Jennings, J.R. and L.M. Peter, *A Reappraisal of the Electron Diffusion Length in Solid-State Dye-Sensitized Solar Cells.* The Journal of Physical Chemistry C, 2007. **111**(44): p. 16100-16104.

100. Snaith, H.J., et al., *Efficiency Enhancements in Solid-State Hybrid Solar Cells via Reduced Charge Recombination and Increased Light Capture.* Nano Letters, 2007. **7**(11): p. 3372-3376.

101. Schmidt-Mende, L. and M. Gratzel, *TiO_2 pore-filling and its effect on the efficiency of solid-state dye-sensitized solar cells.* Thin Solid Films, 2006. **500**(1-2): p. 296-301.

102. Snaith, H.J., et al., *Charge collection and pore filling in solid-state dye-sensitized solar cells.* Nanotechnology, 2008. **19**(42).

103. Ding, I.K., et al., *Pore-Filling of Spiro-OMeTAD in Solid-State Dye Sensitized Solar Cells: Quantification, Mechanism, and Consequences for Device Performance.* Advanced Functional Materials, 2009. **19**(15): p. 2431-2436.

104. Snaith, H.J., et al., *Efficiency enhancements in solid-state hybrid solar cells via reduced charge recombination and increased light capture.* Nano Letters, 2007. **7**(11): p. 3372-3376.

105. Burschka, J., et al., *Tris(2-(1H-pyrazol-1-yl)pyridine)cobalt(III) as p-Type Dopant for Organic Semiconductors and Its Application in Highly Efficient Solid-State Dye-Sensitized Solar Cells.* Journal of the American Chemical Society, 2011. **133**(45): p. 18042-18045.

106. Cai, N., et al., *An Organic D-pi-A Dye for Record Efficiency Solid-State Sensitized Heterojunction Solar Cells.* Nano Letters, 2011. **11**(4): p. 1452-1456.

107. Desai, U.V., et al., *Solid-state dye-sensitized solar cells based on ordered ZnO nanowire arrays.* Nanotechnology, 2012. **23**(20).

108. van de Lagemaat, J., N.G. Park, and A.J. Frank, *Influence of electrical potential distribution, charge transport, and recombination on the photopotential and photocurrent conversion efficiency of dye-sensitized nanocrystalline TiO_2 solar cells: A study by electrical impedance and optical modulation techniques.* Journal of Physical Chemistry B, 2000. **104**(9): p. 2044-2052.

109. Wang, Q., J.E. Moser, and M. Gratzel, *Electrochemical impedance spectroscopic analysis of dye-sensitized solar cells.* Journal of Physical Chemistry B, 2005. **109**(31): p. 14945-14953.

110. Wang, M., et al., *Surface Design in Solid-State Dye Sensitized Solar Cells: Effects of Zwitterionic Co-adsorbents on Photovoltaic Performance.* Advanced Functional Materials, 2009. **19**(13): p. 2163-2172.

111. Xin, X., et al., *Low-Cost Copper Zinc Tin Sulfide Counter Electrodes for High-Efficiency Dye-Sensitized Solar Cells.* Angewandte Chemie-International Edition, 2011. **50**(49): p. 11739-11742.

112. Leijtens, T., et al., *Hole Transport Materials with Low Glass Transition Temperatures and High Solubility for Application in Solid-State Dye-Sensitized Solar Cells.* ACS Nano, 2012. **6**(2): p. 1455-1462.

113. Wang, H., et al., *Novel Ester-Functionalized Solid-State Electrolyte for Highly Efficient All-Solid-State Dye-Sensitized Solar Cells.* Advanced Materials, 2012. **24**(1): p. 121-+.

114. Kim, J., et al., *Enhanced Performance of I_2-Free Solid-State Dye-Sensitized Solar Cells with Conductive Polymer up to 6.8%.* Advanced Functional Materials, 2011. **21**(24): p. 4633-4639.

115. Yella, A., et al., *Porphyrin-Sensitized Solar Cells with Cobalt (II/III)-Based Redox Electrolyte Exceed 12 Percent Efficiency.* Science, 2011. **334**(6056): p. 629-634.

116. Yum, J.-H., et al., *Panchromatic Response in Solid-State Dye-Sensitized Solar Cells Containing Phosphorescent Energy Relay Dyes.* Angewandte Chemie-International Edition, 2009. **48**(49): p. 9277-9280.

117. Hardin, B.E., et al., *Increased light harvesting in dye-sensitized solar cells with energy relay dyes.* Nature Photonics, 2009. **3**(7): p. 406-411.

118. Desai, U.V., et al., *Hybrid TiO_2-SnO_2 nanotube arrays for dye-sensitized solar cells.* Journal of Physical Chemistry C, 2013. **117**(7): p. 3232-3239.

119. Kim, H. and J. Cho, *Hard templating synthesis of mesoporous and nanowire SnO2 lithium battery anode materials.* Journal of Materials Chemistry, 2008. **18**(7): p. 771-775.

120. Meduri, P., et al., *Kinetically limited de-lithiation behavior of nanoscale tin-covered tin oxide nanowires.* Energy & Environmental Science, 2011. **4**(5): p. 1695-1699.